

OPTICAL MICROSCOPY AND SPECTROSCOPY
AT LOW TEMPERATURES AND HIGH
MAGNETIC FIELDS

A Dissertation

Presented to the Faculty of the Graduate School

of Cornell University

in Partial Fulfillment of the Requirements for the Degree of

Doctor of Philosophy

by

Colin Andrew Heikes

May 2015

© 2015 Colin Andrew Heikes
ALL RIGHTS RESERVED

OPTICAL MICROSCOPY AND SPECTROSCOPY AT LOW TEMPERATURES
AND HIGH MAGNETIC FIELDS

Colin Andrew Heikes, Ph.D.

Cornell University 2015

This dissertation examines my efforts to develop an optical platform to explore low temperature and high magnetic field materials and device characterization. I have developed a modular scanning confocal microscopy platform using room temperature light generation and analysis which relies on an optical fiber to couple light from ambient conditions into a low temperature and high magnetic field sample environment. I have built two microscopes: one for operation in a dilution refrigerator at temperatures below 100 mK and magnetic fields of <9 T, and one for operation in a liquid He bath cryostat with a $7\text{ T} \times 1\text{ T} \times 1\text{ T}$ vector magnet. Both of these microscopes allow for concurrent sample transport measurements.

I apply these microscopes to the study of the electron nematic phase of $\text{Sr}_3\text{Ru}_2\text{O}_7$ through polarization microscopy and to the study of the magnetoluminescence of bulk single crystal CdTe and single layer MoSe_2 . I report optical polarization measurements of $\text{Sr}_3\text{Ru}_2\text{O}_7$ while tuning through the electron nematic phase transitions reported below 1 K and at 8 T, with sample base temperatures as low as 120 mK. I demonstrate the breaking of valley degeneracy in single layer MoSe_2 with applied magnetic fields through polarization resolved photoluminescence measurements with out-of-plane fields up to 6.7 T. I demonstrate that the emission from MoSe_2 becomes circularly-polarized in magnetic field even with unpolarized excitation, and that the degree of this polarization

can be increased to about 50% by gating the sample. This suggests that electric fields can facilitate the generation of valley-population imbalance in samples where valley degeneracy has been broken by magnetic field. Finally I present preliminary efforts to incorporate two dimensional transition metal dichalcogenides (TMDs) with ferroelectric thin films for ferroelectricly gated semiconductor devices.

BIOGRAPHICAL SKETCH

Colin Heikes was born in Boulder, Colorado and grew up in southern Rhode Island. He left New England for the D.C beltway to obtain his B.S. in Materials Science and Engineering from the University of Maryland, College Park. There he worked with Professor John Cumings as an undergraduate researcher and received his degree in 2008. Colin next moved north to the frozen tundras of Ithaca, New York where he enrolled in a Ph.D. program in Materials Science and Engineering at Cornell University. Colin worked in both the groups of Darrell Schlom and Dan Ralph while at Cornell. He received his M.S. in Materials Science and Engineering in 2013 and completed the degree requirements for his Ph.D in 2015. After graduating with his Ph.D. from Cornell, Colin plans to continue on with further experimental research.

This document is dedicated to my fiance and best friend, Jessica Wayt. I can't express enough how much your help and support has meant to me through this process.

ACKNOWLEDGEMENTS

I would first like to thank my advisor Dan Ralph for the continuous support, both moral and academic, that he has given me over the last 6.5 years. He has been immensely influential in my understanding of how to perform research and how to ask the correct questions in a scientific setting. He put up with many a naive and off topic question, and his patience and knowledge have made me a better scientist. Dan gave me the freedom to pursue topics that interested me, which in turn has given me the confidence and knowledge to move forward as an independent researcher.

I would also like to acknowledge and thank Darrell Schlom, who has also given me a great deal of guidance over the course of my graduate career. Darrell's attitude towards scientific exploration and collaborative research is contagious, and his inquisitive and broad interests have shaped my own scientific interests going forward. His genuine excitement about research and his ability to always ask the right question are both traits that I hope I can emulate.

I am also grateful to Craig Fennie and David Muller for serving on my special committee. I would also like to thank them for interesting and helpful discussions over the course my graduate career.

I must also thank all the members of the Ralph group, both past and present, who have helped make my time at Cornell both intellectually stimulating and joyful. In particular, I must thank Saikat Gosh who was my mentor starting out and who taught me most of the things I know about optics. Together we managed to teach each other about low temperature science. I also want to thank Sufei Shi. Without our late night conversations and without Sufei's indomitable research spirit, this project would have been significantly more difficult. I don't know if I could have done it without having someone else to talk to in lab late

into the night. Josh Parks and Eugenia Tam were also exceedingly helpful in learning about low temperature transport and in troubleshooting while I was learning how dilution refrigerators work. I must also thank Chen Wang, Lin Xue, Yongtao Cui, Kiran Thadani, Wan Li, Taka Moriyama, Alex Melnick, Ted Gudmundsen, Greg Stiehl, Jen Grab, Colin Jermain, Neil Reynolds, Jonathon Gibbons, John Heron, and David MacNeill for helping create a lab atmosphere that was both collaborative and congenial. In particular, I must thank David for all the moral support and direct help with these experiments. His amazing ability to explain QM and EM to me and his hard work on these projects has helped me immensely.

I am also thankful to all the people that I worked with in the Schlom group both at Penn State and at Cornell. I must thank Alex Melville, Carolina Adamo, Charles Brooks, Hanjong Paik and the others who taught me how to use the MBE. Everyone in the group was incredibly supportive and welcoming in my time working with them.

I want to thank the excellent support staff in Clark Hall in CCMR, CNS, and LAASP. In particular I want to thank Nate Ellis for his help with machining and design for these projects. While I never actually completed his course, he helped me immensely. I must also thank Eric Smith whose low temperature knowledge was intrinsic to my work. Eric was always willing and able to help me whenever the dilution refrigerator was looking broken and things were at their bleakest. I don't know how I would have survived without his help.

I finally must thank my friends and family for their support and love. Living in Ithaca would have been so much worse without my great friendships and our extracurricular activities. I need to thank my parents for their support. And last, but most certainly not least, I must thank my wonderful fiance, Jessica Wayt,

without whom this would not have been possible. She has been there for me at every juncture, and here love and support have kept me above water over the course of these last 6.5 years. I could no have done it without her.

TABLE OF CONTENTS

Biographical Sketch	iii
Dedication	iv
Acknowledgements	v
Table of Contents	viii
List of Tables	x
List of Figures	xi
1 Introduction	1
1.1 Optical Measurements at Low Temperature	1
1.2 The Electron Nematic Phase of $\text{Sr}_3\text{Ru}_2\text{O}_7$	3
1.3 Transition Metal Dichalcogenides as a Two Dimensional Material System	8
2 A Modular Design for Concurrent Optical and Transport Measurements	12
2.1 Coupling Light into an Optical Fiber	12
2.2 Low Temperature, High Field Optical Coupling and Analysis	16
2.3 Sample Positioning and Optical Scanning	29
2.4 Sample Thermalization, Transport Measurements and Low Temperature High Magnetic Field Constraints	42
2.5 Conclusions	47
3 Polarization Microscopy of Bilayer Strontium Ruthenate	48
3.1 Polarization microscopy in our microscopes	48
3.2 Characterization and Mounting of the $\text{Sr}_3\text{Ru}_2\text{O}_7$ Sample	52
3.3 Initial Measurements and Polarization Maintaining Fiber	56
3.4 Polarization Maintaining Fiber Based Measurements	61
3.5 Discussion of Results	73
3.6 Conclusions	76
4 Magnetoluminescence Spectroscopy of Semiconductors at Cryogenic Temperatures	77
4.1 Photoluminescence in Our Microscopes	77
4.2 Magnetoluminescence of Bound Excitons in Bulk CdTe	81
4.3 Breaking of Valley Degeneracy by Magnetic Field in Monolayer MoSe_2	83
4.4 S1. Dependence of Luminescence Handedness on Excitation Handedness	95
4.5 S2. Background Subtraction and Fitting	96
4.6 S3. Comparison of Data from Multiple Devices	99
4.7 S4. Further Discussion of the Trion Luminescence and its Gate Voltage Dependence	101

4.8	S5. Calculations of the Exciton Valley Splitting within $\mathbf{k} \cdot \mathbf{p}$ Theory and Tight-binding Models	108
4.9	S6. Experimental Determination of the Sign of the Valley Splitting	111
4.10	S7. Power Dependence of Trion Polarization	113
5	Future Directions	115
5.1	Introduction to Ferroelectrics as Gate Oxides for 2D Materials	115
5.2	Finding a Relevant Ferroelectric	119
5.3	Future Device Plans	123
A	Current state of the dilution refrigerator, and updated SOPs	124
A.1	Electrical lines and switchboxes:	124
A.2	Temperature Measurement	127
A.3	1 K Pot Changes	128
A.4	Mash Circulation Pump	130
A.5	Optical Fiber Feedthroughs and Maintenance	134
	Bibliography	137

LIST OF TABLES

4.1	Valley Splitting for Various Devices	101
-----	--	-----

LIST OF FIGURES

1.1	Crystal Structure of $\text{Sr}_3\text{Ru}_2\text{O}_7$	4
1.2	Nematic Phase Diagram and Resistive Anisotropy	6
1.3	Angle Dependence of the Nematic Phase Diagram	7
1.4	Crystal Structure and Band Structure of TMDs	9
2.1	Fiber Coupling Optics Diagram	14
2.2	Schematic of Low Temperature Microscope Insert and Dewar	18
2.3	Fixed Position Fiber Collimation and Objective Lens Mount	20
2.4	Piezoceramic Tube Lens Holder	23
2.5	Expected Z Contrast for Scanning Confocal Microscope	26
2.6	Spot size Measurement with Knife Edge	28
2.7	Images and Schematic of an AFM Calibration grid	32
2.8	Circuit Diagram and Layout for Piezotube Amplifier	37
2.9	Temperature Dependence of Piezotube Imaging	41
2.10	Optical Microscope Insert with Thermalized and Clamped Sample	43
2.11	Sample Holder and Thermalization Plate	46
3.1	Photo of Polarization Detection Setup	51
3.2	Laue Pattern and Mounted Sample Geometry	54
3.3	Polarization Maintaining Fiber Launch and Panda Fiber Geometry	58
3.4	Polarization Response at 1.3 K	63
3.5	Magnetic Field Dependence of the Polarization Response with Time	65
3.6	Typical Polarization Sweeps at Dilution Temperatures	67
3.7	Lowest Drift Polarization Angle vs. Magnetic Field Sweep	68
3.8	Polarization Angle vs. Magnetic Field with Incoherent Excitation	70
4.1	Photoluminescence Optics	79
4.2	Photoluminescence Spectra of CdTe at 0 T and 6.7 T	82
4.3	Experimental Geometry and Initial Spectroscopy	85
4.4	Polarization-Resolved Luminescence Spectra and Band Diagram	87
4.5	Valley Splitting with Magnetic Field	89
4.6	Gate Dependence of Valley Splitting	93
4.7	Luminescence Handedness Dependence on Excitation	97
4.8	Fiber Background Spectra	97
4.9	Peak Fitting Comparison	98
4.10	Comparison of Sample Valley Splitting	100
4.11	Gate Dependence of D	102
4.12	Band Diagrams for Gate Dependence of Trion Luminescence	103
4.13	Trion Valley Scattering Rate	107
4.14	Power Dependence of Trion Polarization	114
5.1	θ -2 θ Scans of SrTiO_3 Film on (110) NdGaO_3	122

A.1	Diagram of Kelvinox Switchboxes	125
A.2	Diagram of Pumps in Corridor	129
A.3	Diagram of Circulation Pump	131
A.4	Gas Handling System Diagram	133

CHAPTER 1

INTRODUCTION

1.1 Optical Measurements at Low Temperature

Optical techniques are highly useful for characterizing materials systems and studying electronic structure. Aside from imaging an object, light couples to a multitude of materials properties with techniques such as optical reflectivity, absorption, photoluminescence (PL), Raman spectroscopy, second harmonic generation (SHG), and magneto-optic Kerr or Faraday rotation measurements. Optical techniques can be used to probe band structure (absorption or PL), electron-lattice coupling (optical reflectivity and Raman spectroscopy), lattice symmetry (SHG), magnetization (Kerr and Faraday rotation), phonon or other quasiparticle excitations (Raman spectroscopy), as well as other properties. As well as coupling to a multitude of materials properties, light can be focused down to probe sizes limited only by the wavelength of the excitation and diffraction. This gives an ability to measure the spatial nature of materials properties and is particularly useful for studying sample non-uniformity and defects.

Measuring the low temperature properties and the temperature dependence of materials give information about the ground states and underlying physics of properties such as band structure and electronic scattering mechanisms. In particular, cooling suppresses thermal excitations and this suppression can open up the study of quantum properties coming from electron correlations such as superconductivity and charge or spin ordering. Temperature and magnetic field offer two handles to investigate the interactions and properties of these correlated phases. Optical techniques such as Raman microscopy, optical conductiv-

ity, magneto-optic Kerr microscopy, and photoluminescence are all of interest for investigating the nature of these correlated electron phases [1, 2, 3, 4].

Combining optical techniques with low temperature techniques bring forth various issues. Optical techniques with high spatial resolution generally require samples to be positioned in close spatial proximity to lenses, which is not generally consistent with cooling samples to cryogenic temperatures. The samples need to be placed in a vacuum environment to prevent condensation of gases onto the sample surface, so the optics need to be included in the sample vacuum space or the sample vacuum space needs to have optically transparent windows for optical access to the sample. There are many potential ways to cool samples with optical access, with a large array of companies offering design solutions using flow cryostats with windows, bath cryostats with windows, or even pulse coolers with windows. These window based cryostats tend to be incompatible with large magnetic fields, as the superconducting magnet geometries tend to enclose the sample in non-transparent materials. There are a few options available for coupling light into a high field magnet bore, in particular attocube systems has made great strides recently in the design of a free space coupled confocal microscopy platform for spectroscopy applications in diamond NV centers [5]. These window based systems are also not very compatible with cooling below 1 K, as the thermal radiation through the windows can add a large heat load to the samples. These systems are also exceedingly expensive. Another possible route is to use optical fibers to couple light into a sample space with high magnetic fields and low temperatures. This concept has been pursued for measuring PL of semiconductor quantum dots, PL of quantum Hall states, and polar Kerr microscopy [3, 6, 7, 8, 9]. We will present our own design for an optical fiber based confocal microscope that functions at temperatures below 100

mK and magnetic fields up to 9 T, which we use for polarization microscopy of $\text{Sr}_3\text{Ru}_2\text{O}_7$ and magnetoluminescence of monolayer transition metal dichalcogenides (TMDs), in particular MoSe_2 .

1.2 The Electron Nematic Phase of $\text{Sr}_3\text{Ru}_2\text{O}_7$

$\text{Sr}_3\text{Ru}_2\text{O}_7$ is the $n=2$ member of the Ruddlesden-Popper phase layered perovskite structure for strontium ruthenate. These Ruddlesden-Popper phases of strontium ruthenate show a wide variety of ground states. While the $n=1$ member shows unconventional superconductivity and the $n=\infty$ is an itinerant ferromagnet, $\text{Sr}_3\text{Ru}_2\text{O}_7$ is a metamagnet with a phase transition below 1 K and between 7.95 T and 8.15 T [11][12]. This low temperature, high magnetic field phase shows broken rotational symmetry in transport, and is considered to be the analogue of a nematic liquid crystal for an electron fluid [13]. This phase transition is only seen in crystals with very high purity, as measured by residual resistivity (ρ_{res}) [11].

Figure 1.1 illustrates the crystal structure of the $n=2$ bilayer $\text{Sr}_3\text{Ru}_2\text{O}_7$. It has space group Bbcb, which corresponds to a face centered orthorhombic structure, due to rotations of the oxygen octahedral. These rotations do not correspond to any difference between the a and b lattice parameters which makes the a and b axis effectively indistinguishable in a Laue measurement [10]. Figure 1.1 illustrates these rotations in the right portion of the figure. Since the phase transitions only show up in high purity crystals, improvements in single crystal growth technique were needed. These high quality $\text{Sr}_3\text{Ru}_2\text{O}_7$ single crystals are grown by a flux feeding floating zone (FFFZ) technique in an image furnace as

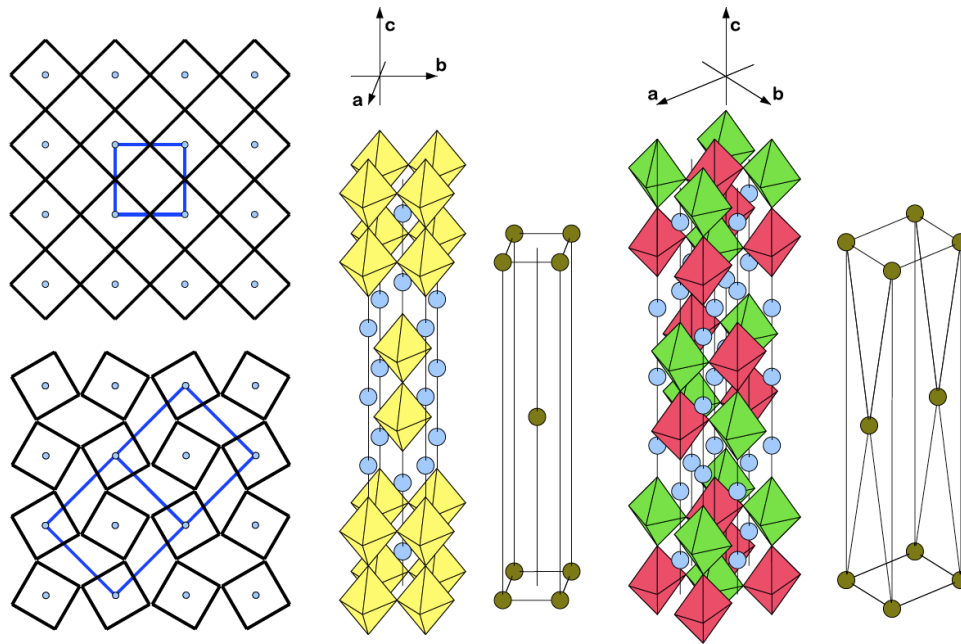


Figure 1.1: Crystal Structure of $\text{Sr}_3\text{Ru}_2\text{O}_7$. Left: In-plane representation of the octahedra before rotation (top), and after (bottom). The basal unit cell is shown in blue. Middle: Undistorted lattice unit cells. Right: Distorted unit cell. Yellow octahedra are not rotated, the green are rotated clockwise in the ab -plane, and the red counter-clockwise. The respective crystallographic axes are represented, the ones for the distorted lattice rotated by 45° around the c -axis. Figure adapted from [10]

described by Perry et al. [14]. The key improvement was the ability to measure the evaporated mass of various species during growth, which allowed for improvement of crystal stoichiometry. This led to growth of crystals with ρ_{res} below $1 \mu\Omega\text{cm}$.

The previously mentioned electron nematic phase has been detected using a variety of thermodynamic, magnetic, and transport techniques, as is shown in figure 1.2 A [11]. The nematic nature of this phase has been probed with magnetoresistance measurements and dilatometry. The broken symmetry was first detected as a resistive anisotropy between the a and b crystal axes when a slight in-plane magnetic field was directed along either crystal axis, shown in figure 1.2 B and C [13]. This in-plane field is generated by canting the applied field away from the sample c-axis by an angle, θ . A full mapping of the resistive anisotropy with field and canting angle is shown in figure 1.2 D and E. Initial neutron diffraction measurements showed no lattice distortions upon entering the nematic phase to one part in 10^5 , but later magnetostriction and thermal expansion measurements showed that there is a lattice distortion upon entry into the phase of one part in 10^7 [15] [13]. These same dilatometry measurements illustrate the shift in nematic phase boundaries with changing θ , as is shown in figure 1.3.

An important point is that there are nominally domains of differing order parameter within this phase which prevent the detection of resistive anisotropy with zero in-plane magnetic field, but still show increased scattering even with no in-plane field [13]. There is no evidence for magnetic domain formation in the samples, but the lattice distortion measured in dilatometry measurements has a magnetic field angle dependence that suggests an orbital driven structural

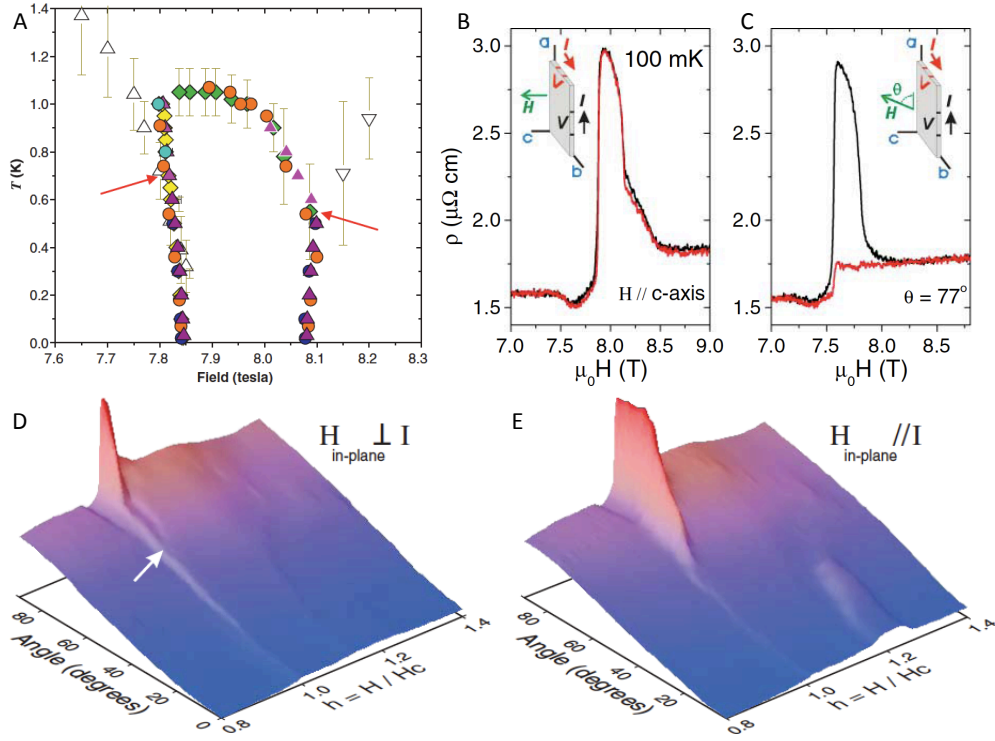


Figure 1.2: Nematic Phase Diagram and Resistive Anisotropy: (A) An empirical phase diagram of $\text{Sr}_3\text{Ru}_2\text{O}_7$ obtained from collating data from dc magnetization (orange circles); the loci of maxima in $d\rho/dH$ (yellow diamonds); loci of peaks in ac susceptibility (purple triangles); loci of maxima in the magnetostriction (blue circles); and the loci of maxima in $d\rho^2/dT^2$ (green diamonds). The red arrows mark the temperatures of critical points deduced from the temperatures above which no peak in χ'' is observable. Figure adapted from figure 3 of [11] (B) The two diagonal components ρ_{aa} and ρ_{bb} of the in-plane magnetoresistivity of $\text{Sr}_3\text{Ru}_2\text{O}_7$ for an applied field parallel to the crystalline c-axis (C) The same resistivity measurement with the crystal tilted such that the field is 13° from c, giving an in-plane component along a. (D), (E) Three-dimensional plots of the magnetoresistivity components ρ_{aa} (D) and ρ_{bb} (E) of a single crystal of $\text{Sr}_3\text{Ru}_2\text{O}_7$ as the external magnetic field is rotated from alignment along the crystalline a axis (0°) to alignment along the crystalline c axis (90°), at a constant temperature of 100 mK. The quantity $H_c(q)$ that normalizes h is the main metamagnetic transition. It varies smoothly from 5.1 T at 0° to 7.87 T at 90° . (B, C, D, E) are adapted from figures 1 and 2 of [13]

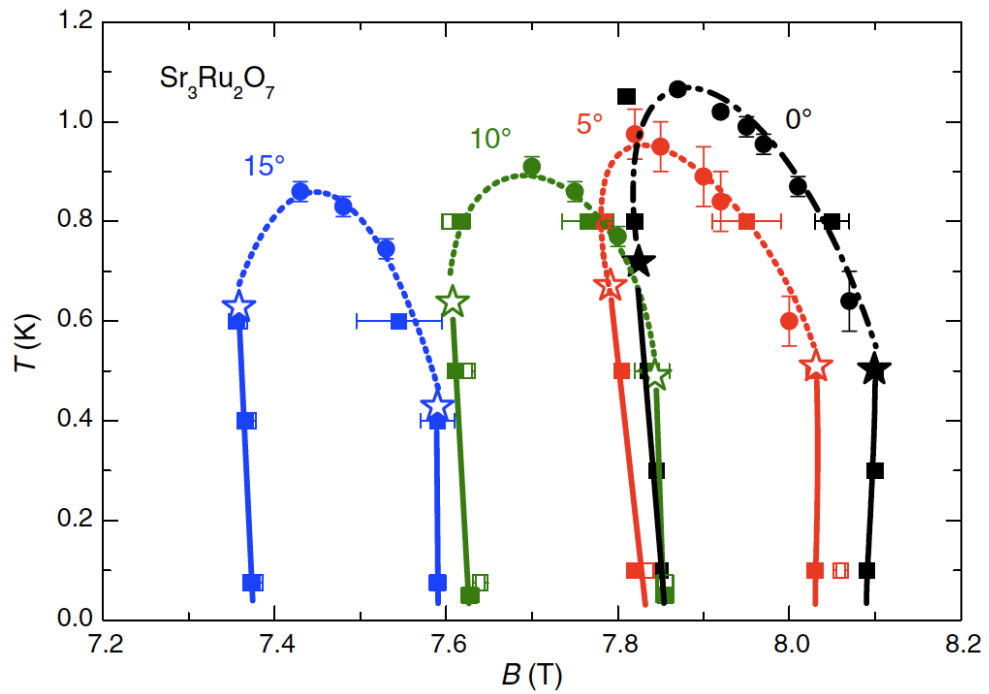


Figure 1.3: Angle Dependence of the Nematic Phase Diagram: Phase diagram of the nematic phase of $\text{Sr}_3\text{Ru}_2\text{O}_7$ at different tilt angles. The squares and circles denote transitions in magnetostriction and thermal expansion, respectively (solid symbols: $\Delta L \parallel B_{\text{in-plane}}$, open symbols: $\Delta L \perp B_{\text{in-plane}}$). Adapted from figure 4 of [15]

distortion. These domains appear to align with applied field, with applied field angles with θ greater than 10^0 showing almost completely aligned domains [15]. The size of these domains and the relationship between domain size and applied field angle is uncertain, with an indirect size estimate of 500 nm for field normal to the sample, coming from de Haas-van Alphen effect measurements of the allowed carrier orbits within the nematic phase dome [16]. Very recently neutron diffraction measurements in field suggest the nematic phase is an ordered spin density wave (SDW) state, with domains and resistivity changes coming from domains of the SDW order parameter [17].

1.3 Transition Metal Dichalcogenides as a Two Dimensional Material System

Monolayer MoSe_2 and other monolayer transition metal dichalcogenides (TMDs) are a materials system with unique potential for controlling their valley degree of freedom [18, 19, 20, 21, 22, 23, 24, 25]. Similar to graphene, the conduction and valence band show extrema (valleys) at the vertices of a hexagonal Brillouin zone; unlike graphene, MoSe_2 exhibits a nonzero optical gap of 1.66 eV [26, 27].

The structure of layered TMDs is similar to that of graphite and each layer has a thickness of 0.6-0.7 nm with strong in-plane covalent bonding and weak out-of-plane van der Waals interactions. Single layers of TMDs are found in two polytypes, depending on the position of the chalcogen (X) with respect to the metal element (M) in the X-M-X structure. The TMD monolayer polytypes can be either trigonal prismatic or octahedral . The structure of these layers is shown

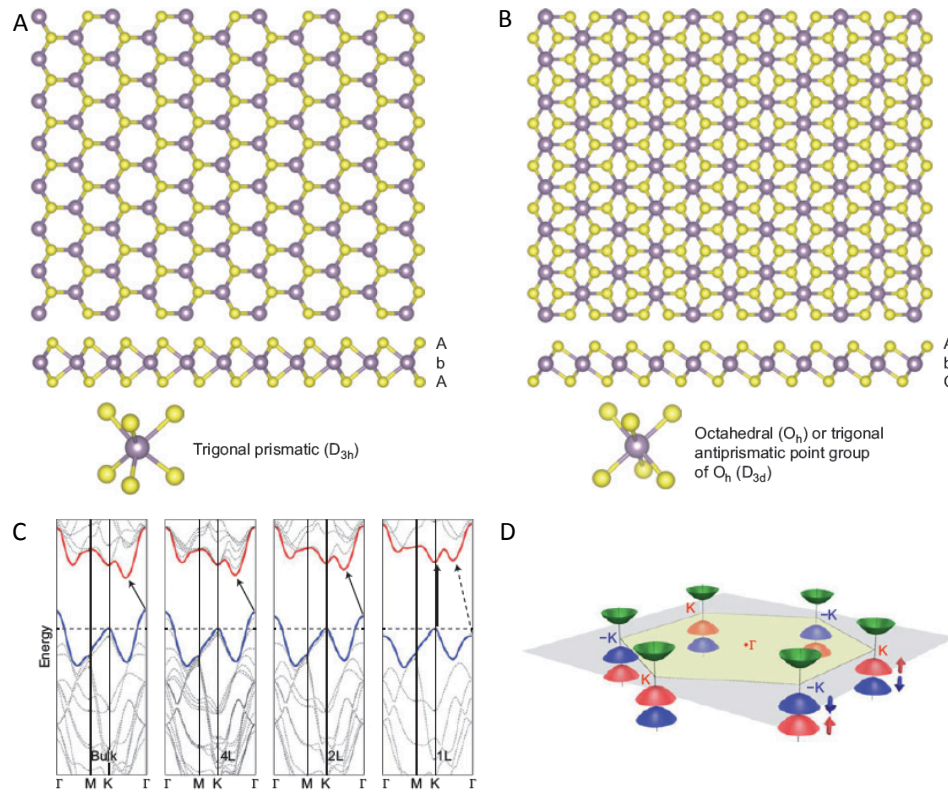


Figure 1.4: Crystal Structure and Band Structure of TMDs: (A) and (B) c-Axis and section view of single-layer TMD with trigonal prismatic (A) and octahedral (B) coordinations. Atom color code: purple, metal; yellow, chalcogen. The labels AbA and AbC represent the stacking sequence where the upper- and lower-case letters represent chalcogen and metal elements, respectively. (C) Energy dispersion (energy versus wavevector k) in bulk, quadrilayer (4L), bilayer (2L) and monolayer (1L) MoS₂ from left to right. The horizontal dashed line represents the energy of a band maximum at the K point. The red and blue lines represent the conduction and valence band edges, respectively. The lowest energy transition (indicated by the solid arrows) is direct (vertical) only in the case of a single layer. Indirect transition in monolayer (dashed arrow in 1L plot) is greater in energy than the direct band edge transition (solid arrow). (D) Band structure of MoS₂ showing six valleys and opposite spin-orbit splitting of the valence band at the K and K (-K) points. The red and blue surfaces represent spin-orbit-split valence band maxima, each of which is associated with a particular electron spin. The green surfaces represent the conduction band minima or the valleys. All figures are adapted from [28] figures 1 and 2

in figure 1.4 A and B [28]. The half-filled d-orbitals of group VIB transition metals (i.e. $M = \text{Cr, Mo, W}$) results in semiconducting behavior with decreasing band gap as the chalcogen atomic number is increased (i.e., $X = \text{S, Se, Te}$). The band alignment and band gap of these materials is dependent on the thickness or number of layers of TMD present. Figure 1.4 C presents DFT calculations of the energy band dispersions for reduced thickness of the TMD MoS_2 . When you transition from 2 layers to 1 layer, the lowest energy transition becomes a direct band transition at the K points of the Brillouin zone. Inversion symmetry is also broken in the monolayer case. The large spin-orbit coupling from the transition metal component combined with this band structure leads to the graphene like hexagonal Brillouin zone shown in figure 1.4D with opposite spin split bands in the K and K valleys[28].

Initial interest in optical measurements of MoS_2 single layers arose when it was demonstrated through PL measurements that monolayer MoS_2 shows enhanced PL compared to bilayer or thicker samples[29]. It was later shown that resonant PL from the different valleys is polarized and the K and K valleys can be independently addressed using circularly polarized excitation [19]. These discoveries have allowed for exploration of optoelectronic properties arising from the valley-dependent chirality of massive Dirac fermions, predicted in the context of inversion symmetry broken graphene [30, 31]. This chirality leads to optical selection rules coupling the exciton valley degree of freedom to photon handedness [19, 20, 21, 22, 23, 24]. Using polarization-resolved spectroscopy researchers have demonstrated valley-selective luminescence with near 100% fidelity [19, 24]. Furthermore, the ability to pump valley-polarized carriers with circularly-polarized light has been demonstrated through the valley Hall effect [25]. The chiral electronic states are also predicted to possess valley-

contrasting orbital magnetic moments coupling valley pseudospin to magnetic field [30, 31, 32, 33, 34, 35, 36], which opens up the possibility for magnetic control over the valley degree of freedom [37, 32].

CHAPTER 2

A MODULAR DESIGN FOR CONCURRENT OPTICAL AND TRANSPORT MEASUREMENTS

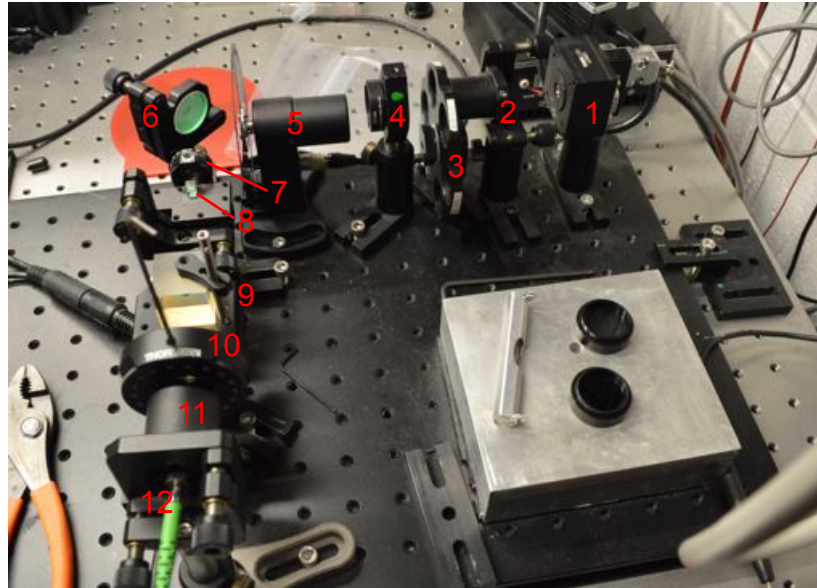
Optical microscopy at low temperatures and high magnetic fields presents a plethora of design challenges. Adding the capabilities for concurrent transport or other electrical measurements complicates things further. In order to mesh the desire for extreme sample conditions with the desire for different types of optical measurements, we rely on coupling light from ambient conditions down into our dewars with a glass optical fiber. We rely on this fiber to both couple light to our sample and to collect the light after it interacts with the sample. This allows us to minimize the number of optical elements that need to be compatible with sub 4 K temperatures and high magnetic fields. We also rely on room temperature light analysis and generation. These standard room temperature spectrometers, photodetectors, lasers, or incoherent light sources give us access to a broad array of measurement techniques within the same optomechanical platform. The combination of transport and electrical measurements with the optical access further expands our capabilities to include photocurrent measurements, electrically gated optical measurements, or other combinations.

2.1 Coupling Light into an Optical Fiber

For our photoluminescence, photocurrent, and polarization microscopy measurements, we use the same basic assembly to couple light from a laser diode into our optical fiber. This assembly is shown in figure 2.1. With some minor modifications, this basic assembly can be used to couple any light source into our fiber. We start with a Thorlabs T-Cube laser diode driver and temperature

controller connected to a Thorlabs thermoelectrically cooled laser diode mount. We mount a single mode laser diode in this mount, and then adjust a lens in the housing of the laser diode mount to collimate the spot. This collimated spot is elliptical in shape, so we use an anamorphic prism pair to shape the beam into a Gaussian beam profile. We choose a prism magnification from the stated ellipticity of the diode specifications. Proper beam collimation and shaping is critical for optimal coupling of the light from free space into the single mode fiber. After shaping the beam, we have a filter mount wheel with a series of neutral density filters and a static filter mount so we can either clean up the spectral properties of the beam or attenuate the beam. We insert an optical chopper in the beam path here to allow us to take advantage of lock-in amplifier based techniques for improvement in signal to noise for our photo-detectors.

At this point (after element 5 in figure 2.1), we have a nominally collimated, Gaussian beam with some unknown polarization; set by the diode heterostructure. The next element is a dielectric mirror mounted on a kinematic mirror mount used reflect the beam and to set the correct path of the beam for optimal fiber coupling geometry. The light next passes through a half wave plate on a rotation mount and a polarizing beam cube aligned normal to the optical path. This beam cube sets the polarization geometry for our light source, while the wave plate rotates the polarization of the beam. By adjusting the angular relationship between the wave plate and the beam cube, we can either optimize the transmission of the beam cube or continuously attenuate the transmitted beam power by changing the weights between the transmitted linear polarization and the orthogonal reflected linear polarization. Now that we have set the polarization of the beam with respect to the geometry of the optical table, we use a non-polarizing beam cube with 10% transmission in one channel and 90%



- | | |
|--------------------------------------|---|
| 1. LDM21 Laser Diode Mount with Lens | 7. $\lambda/2$ wave plate |
| 2. Anamorphic Prism Pair | 8. Polarizing Beam Cube |
| 3. ND Filter Wheel | 9. 90/10 Beam Cube |
| 4. Fixed Filter Mount | 10. $\lambda/2$ wave plate for fiber launch |
| 5. Optical Chopper | 11. Fiber Coupling Lens on Kinematic Mount |
| 6. Dielectric Mirror Mirror Mount | 12. FC/APC Fiber Adapter Mount |

Figure 2.1: Fiber Coupling Optics Diagram. This is a schematic of the optics used to generate and couple our laser diode source into our optical fiber. The label numbers in the photo correspond to the elements labeled in the key.

transmission in the other. We align this cube, called the detection cube, so that 10% of the polarized beam transmits through the cube to the fiber coupling, which will allow us to collect 90% of the signal once the signal exits the fiber after interacting with the sample. We next insert a second half wave plate, which we will call the fiber launch wave plate, which allows us to rotate the launch polarization with respect to the fiber. This will matter if we are launching into a polarization maintaining fiber. Our fiber is attached to a Thorlabs FC/APC fiber adapter, which is mounted on a kinematic mirror mount. We attach a short, threaded lens tube to this fiber mount. This lens focuses the polarized, collimated, Gaussian beam down onto the fiber core, which couples the light into the fiber.

An important point of our setup is that we get stable coupling from free space into our single mode optical fiber, with a minimalistic setup. As is explained in [38], coupling free space light into a single mode fiber is a complicated business where coupling efficiency is dependent not only on the geometry and proper alignment of the optical elements, but also on the proper mode matching between the Gaussian mode of the fiber and the mode of the incident light. Fortunately for us, we are coupling light into a cryogenic environment where high optical powers are the enemy. We don't need to approach the theoretical limits for coupling efficiency, but good coupling does reduce possible artifacts from coupling power drift during a measurement. By choosing an optimal pair of lenses for collimating the laser diode and for focusing down to the fiber core, we can fulfill enough of the coupling requirements that we can instead focus on the temporal stability of the coupling. As explained in [38], we need to focus our beam down to the mode diameter of the single mode fiber. To do this, we pick a laser collimating lens that gives us a beam diameter where we

can find a fiber coupling lens that satisfies $f = D(\pi\omega/4\lambda)$. Here f is the lens focal length, D is the beam diameter at the lens, ω is the fiber mode diameter, and λ is the laser wavelength. We choose a Thorlabs C171TMD-B collimating lens and a Thorlabs C260TMD-B fiber coupling lens from this relationship.

The second part of coupling stability comes from our choice to use only three mobile elements to set the mechanical alignment of the fiber with the collimated beam. We use kinematic mirror mounts (elements 6 and 11 in figure 2.1) for our dielectric mirror and our fiber mount to mechanically align the fiber with the beam path, and then use the threaded lens tube to position the focusing lens in relation to the fiber core. Since there are only two coupled mobile axes in each mount, we don't have to worry about drift in 6 uncoupled axes like we would if we were trying to position the fiber tip in space. With our system, we can achieve coupling efficiencies, as defined as the ratio of power incident on the fiber to the power transmitted through the fiber, of over 0.7. This coupling is stable for time scales on the order of days, and any mechanical drift on this time scale is usually due to small position changes in the kinematic mounts. This can be easily fixed with a few minutes of work. The position of the focusing lens with respect to the fiber can drift on the order months, and this is slightly more involved to re-optimize.

2.2 Low Temperature, High Field Optical Coupling and Analysis

Once we've coupled the light into the fiber, we have to then take the light out of the fiber, interact it with our sample, and then re-couple it back into the fiber.

To simplify this process, we have designed and machined an optical housing that allows us to use standard optical parts designed for room temperature operation at low temperature. Figure 2.2 illustrates the relationship between our bench top light generation and our microscope insert that sits inside the bore of our magnets. We have some very severe spatial limitations in this design, as we are limited by the diameter of the bore of the magnet and by the space above and below the magnet field center in our dewar. The dewar for the Kelvinox dilution refrigerator has the smaller diameter bore and less room below the magnet field center so we use these constraints for our designs. Aside from spatial constraints of fitting our insert into the dewar and magnet, a critical issue is fixing the spatial relationship between optical elements as we change the magnetic field or the temperature. Many of these optical elements have housings or mountings made of steel, so we must fix them firmly to prevent shifting positions with field. Figure 2.2 B shows our design, with spatial axes labeled. This optical housing is modeled after a lens tube, which fixes the optical elements spatially in x and y , while allowing us to adjust the z -spacing between elements with optional spacers. We can also adjust the rotational relationship in the x - y plane between elements. We rely on the machined tolerances between our housing and any optical element holder to keep everything centered on the fiber core, while we rely on a clamping force directed in the z -direction and machined flat surfaces for each element to prevent any tilting out of the x - y plane. We try to keep our parts as rotationally symmetric as possible and make all of our parts out of the same material, either OFHC copper or aluminum, to eliminate large positional shifts during cooling from thermal contraction.

We first mechanically attached our fiber to an off-the-shelf fiber-coupled collimator assembly and then into a sleeve similar to the one shown in figure 2.3A.

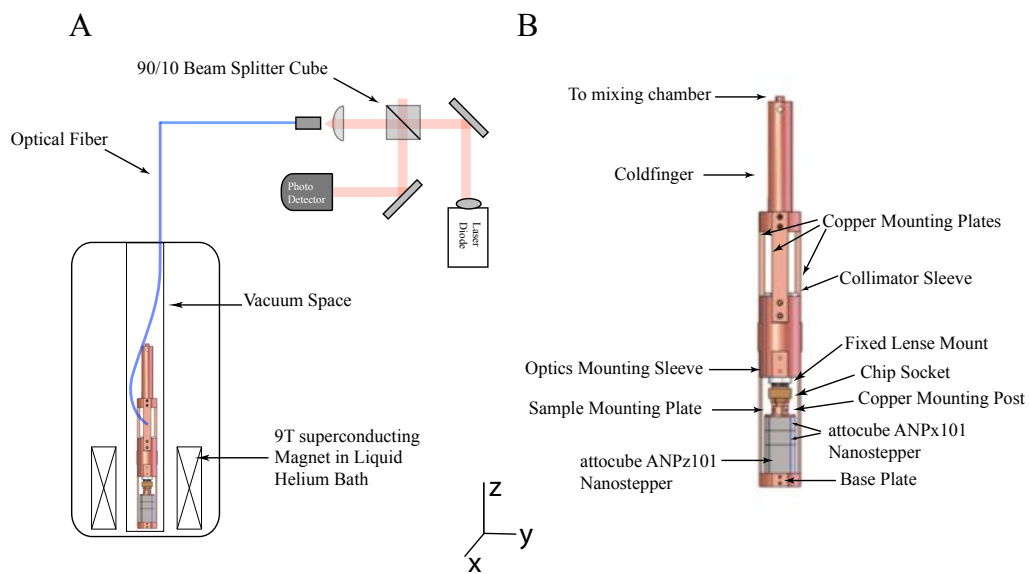


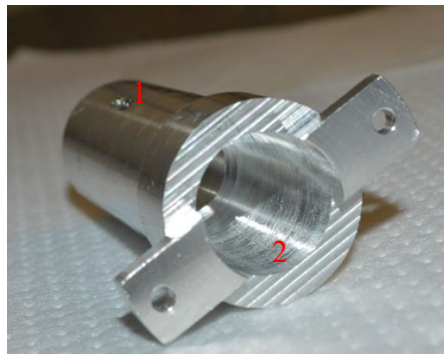
Figure 2.2: Schematic of Low Temperature Microscope Insert and Dewar. (A) Illustrates the coupling of light from room temperature down to our sample at sub 4.2 K temperatures to the bore of our magnet. For the vector magnet, the setup is nearly identical. (B) Assembly drawing of the microscope insert for the dilution refrigerator based setup. The optical axis is along the labeled z -axis and the x and y axes correspond to sample motion for image formation

This sleeve is modeled after Thorlabs own fiber collimator mounts to allow us to choose an off-the-shelf collimator assembly based on the desired operation wavelength and beam diameter. The set screws labeled in figure 2.3 A fix the collimator assembly in our collimator sleeve, and give us rotational freedom. For our work at 780 nm, for example, we use a Thorlabs F260APC-780 fixed focus aspheric fiber collimation package. This collimator has a fiber coupling termination which accurately sets the distance between the fiber tip at the focal point of an aspheric lens for optimal collimation. The collimator fits into our machined sleeve and this sleeve locates the collimator spatially in x-y with respect to our housing, nominally centering our fiber core on the axis of the housing. The collimator is clamped into the sleeve using two sets of three-fold symmetric set screws, giving us some slight freedom in both x-y position and collimation package tilt. This freedom will allow us to optimize coupling back into the fiber later for sample luminescence based experiments.

Once weve coupled the light out of the fiber, we can mount other free space optical elements between this collimator and our focusing lens. In particular, we can manipulate the beam polarization using a retarder of some kind or add in filters. These elements are epoxied or clamped into their own mounting sleeves, and are held in registry with the optical housing from their machined tolerances. These elements will not change the shape of the beam, so it is most important that they are positioned normal to the beam axis to make sure there are no off axis reflections or refractions.

The collimated beam next enters our focusing lens and is focused down to a spot. We have two major designs for mounting this lens: one which allows us to position the lens with respect to a spatially fixed sample using a piezoelec-

A



B



1. Set screw for collimator
2. Cavity for collimator and/or polarization optics
3. Lens mount
4. Threaded end

Figure 2.3: Fixed Position Fiber Collimation and Objective Lens Mount (A) Fiber collimator mounting sleeve, which fixes the fiber collimator into the optics mounting sleeve. The cavity is a slip fit for a Thorlabs 11 mm OD fixed focus aspheric collimation package. (B) A photo of the adapter for mounting an objective lens to our collimator sleeve. The threaded end attaches directly to the face of the collimator sleeve that is out of sight in (A). The lens mount has been faced off to allow the lens to jut out from the assembly

tric tube, and one that fixes the position of the lens with respect to the optical housing with no ability to position it after it is mounted. I will first treat the fixed lens position case, which is shown in Figure 2.3 B. This holder fixes the lens so that the focal point of the lens is either at the z-position of the magnetic field center or at a known location away from that field center in the case of the dilution refrigerator due to spatial constraints. Notice that the lens sticks out from the face of the lens holder. As I will discuss when I describe the sample holder, any extra diameter at the lens position can prevent us from positioning the sample at the lens focal point for high NA, short focal length lenses. The lens holder is threaded at the end to accept any lens with an M9 x 0.5 mounting thread. Switching to a smaller lens size is as easy as making a new holder with the correct threading or making an adapter from M9 x 0.5 to the desired lens mount thread. Larger lenses are problematic due to spatial constraints on the collimator assembly diameter and the need to match lens clear aperture to beam diameter. Our eventual spot size is limited by the filling of the lens.

Our second focusing lens holder design uses a piezoelectric tube to position the focusing lens. As shown in figure 2.4, we epoxy a piezoceramic tube to a mounting sleeve, then we epoxy a modified Thorlabs S05TM06 lens cell adapter to the end of the tube. We machine a mating surface into the non-internal-threaded side of the S05TM06 so it fits flat onto the end of the piezoceramic tube. We then turn down the outer diameter of the threaded side of the S05TM06 and face it off so the lens protrudes. We must remove this material due to constraints from the sample holder that I will describe later. Using a piezoceramic tube as a nanopositioner is a concept well explored by the scanned probe microscopy (SPM) communities. A piezoceramic changes its dimensions or strain state with an applied electric field though the inverse piezoelectric ef-

fect. For the lead zirconia titanate (PZT) materials system that is commonly used in commercial piezoelectric devices, strains on the order of 0.1% of the ceramic static dimension are generally achievable with an applied electric field [39]. For SPM technologies, the piezo-tube needs to be able to position an object with nanometer or sub-nanometer precision in all three special axes. For a tube geometry, we can control the deflection of one end of the tube with respect to the other end of the tube by adding a common electrode to the entire inner surface of the tube and then adding four axially separated electrodes to the outer surface of the tube, as is illustrated in figure 2.4 B. When we ground the inner electrode and then apply a voltage to one of those four electrodes, the piezoceramic material that sees the electric field changes its dimension and the tube deflects in the x and y dimensions, though there is a slight coupling to the z-dimension. Applying a positive bias between an outer electrode quadrant and the inner electrode shrinks the lateral dimension of the tube between the electrodes and a negative bias expands the lateral dimension of that material. If we ground the outer electrodes and apply a bias to the inner electrode, we can strain the tube uniformly and position the end of the tube in the z-dimension. By fixing one end of the tube in space and by applying a controlled DC bias to the 5 electrodes, we can position the free end of the tube arbitrarily in space up to the limits of the piezoceramic material. For maximal tube deflection, we apply equal and opposite voltages to the opposite quadrants while grounding the other two quadrants.

We source our piezoceramic tubes from EBL Products, Inc. This company produces custom shaped piezo-tubes with custom electrode geometries and sources five different PZT compositions for various applications. We choose EBL #2 for our tubes for an optimal low temperature deflection range, calcu-

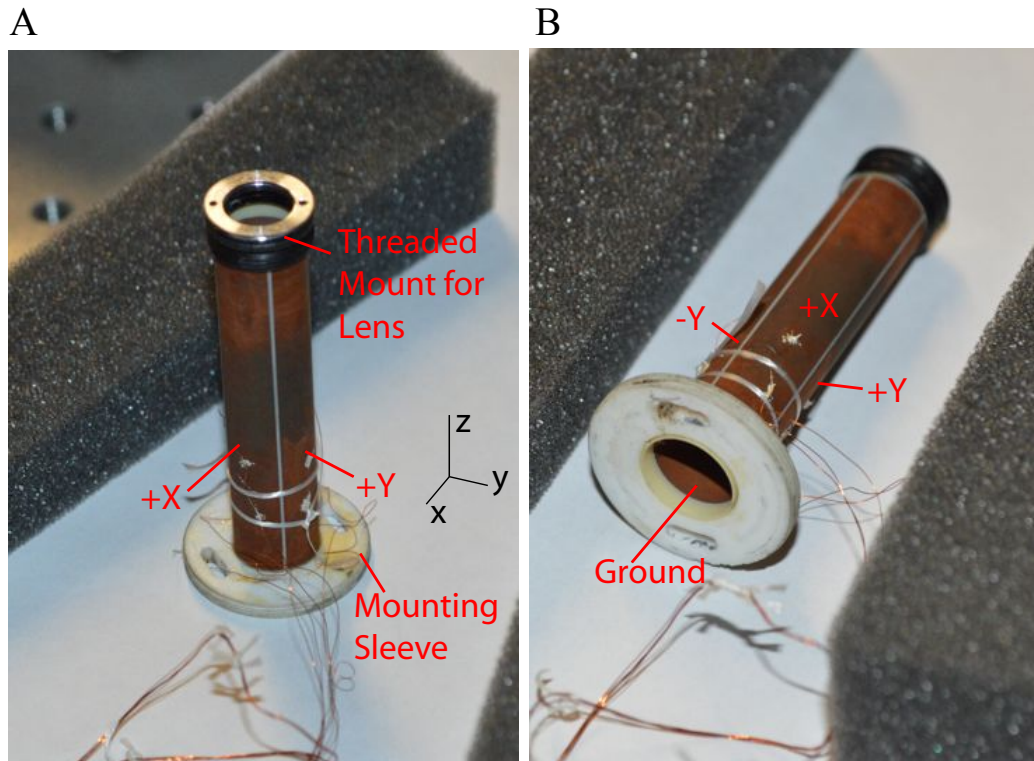


Figure 2.4: Piezoceramic Tube Lens Holder: This piezoceramic tube based lens holder is used to position the focusing objective lens with respect to the sample. (A) shows the threaded termination for mounting an objective lens. (B) shows the electrode geometry. Electrode labels correspond to the direction that the tube end will deflect with a DC bias of the labeled polarity.

lated from the measured piezoelectric coefficients and depoling fields. This depoling field is important, as it gives us a safe limit for how much field we can apply across the tube thickness without altering the piezoresponse of the tube hysteretically. EBL products also provides some basic design formulae for calculating x , y , and z deflections for choosing a tube geometry. When opposite voltages are applied to opposite quadrants, the x or y deflection at a given voltage is given by $\Delta_{x,y} = (0.9d_{31}VL^2)/(d_m t)$ where V is the applied voltage at a quadrant, L is the length of the tube under the electrode, t is the tube thickness, and $d_m = 1/2(OD+ID)$. Here OD and ID refer to the tube outer diameter and inner diameter respectively. From this formula, we can see that optimal x and y positioning ranges come with maximized tube length to diameter aspect ratios and minimal tube thicknesses. In our assembly, we are limited in tube length both by the divergence of the beam from the collimator and by the need to keep the focal point of the optical assembly as close to the magnetic field center as possible. The collimator divergence would severely limit the length of our tube, but we are able to fit the collimator down inside the piezo tube which reduces the distance between the focusing lens and the collimation lens. Considering all of these constraints, including the constraint on tube inner diameter to fit the collimator, we chose piezo tubes with an inner diameter of 0.43, a thickness of 0.014, and a length of 2.2. We have 4 axial sectioned electrodes on the OD and one constant electrode on the ID , with 0.1 of each end of the tube with no electrodes so we can epoxy our mating sleeve and lens holder to the tube without issues of shorting the electrodes. We will show results with this tube geometry, but this choice of ID requires us to remove material from the OD of the collimator assembly. If we were to purchase more tubes, we would increase the inner diameter to 0.46, as this only minimally reduces the scan range. With this geom-

etry, we have an optimal x and y scan range of 50 microns at room temperature and 9 microns at 4.2 K, both for an applied voltage of 250 V which corresponds to the stated depoling field for this material and this piezoceramic thickness. This movement of the tube changes the position of the focus lens which in turn leads to an effective scanning of the position of the focused spot.

These optical assemblies can be thought of as optical fiber detector based point scanned confocal optical systems, as described in Kimura and Wilson's treatment [40]. Here, the excitation comes from the same fiber that is being used as a pinhole for recollection of the light from the sample, which prevents the issues with coherent imaging their treatment of a point source for illumination. The finite size of the fiber core acts as a pinhole and gives efficient coupling of light back into the fiber only when the source of the light comes from the focal plane of the focusing lens. In practice, this gives us two important features. First, we can now use the reflected power coupled back into the fiber to determine if our sample is sitting in the lens focal plane. This gives us a way to bring the sample into the lens focal point without any spatial imaging. Second, this focal plane selectivity gives us the ability to separate reflections from different z-positions in the sample. If we have a sample with a mostly transparent coating, or a sample made of multiple transparent layers we can look at the light reflected from each surface or interface separately. The z-axis selectivity is set by the sensitivity of our detectors and the geometry of the focal spot. From equations 15 and 17 from [40], we can plot the ideal change in detected intensity as a function of distance from the focal plane of the focusing lens for a few choices of focusing lens and laser wavelength, which are shown in figure 2.5. Our ability to distinguish different z-positions at our sample is set by this response and the signal to noise of our detectors.

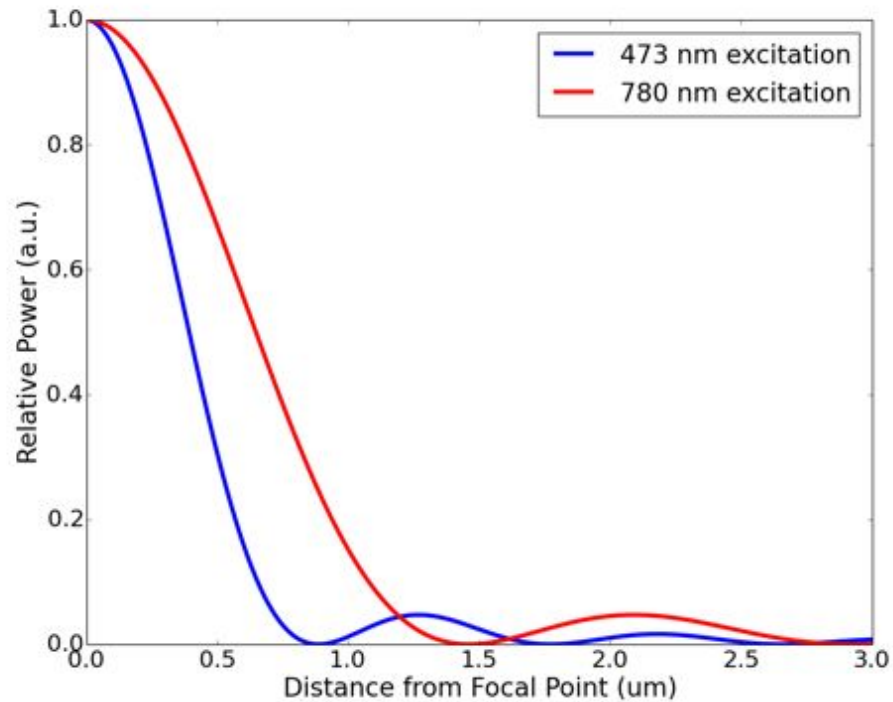


Figure 2.5: Expected Z Contrast for Scanning Confocal Microscope: Here we plot the expected change in collected power vs distance from focal plane for our optical assembly at two different wavelengths. Our ability to detect sample height changes is set by this function, as well as the signal to noise ratio of our detectors. We see here that at 780 nm, a 50 nm step corresponds to about a 1% change in collected power.

In this consideration of our optical setup as a point scanned confocal microscope, our spatial resolution is determined by the waist of the focused beam. In our case our beam waist (w_0) should be set by the relationship $2w_0 = (4\lambda/\pi)(F/D)$ where $2w_0$ is the diameter of the focused spot, λ is the wavelength of the light, F is the focal length of the lens, and D is the diameter of the beam [41]. This only holds for short focal length lenses and beam diameters smaller than the clear aperture of the lens. This effectively means that our spot size is minimized for high numerical aperture (NA) lenses where we fill the clear aperture of the lens completely with the collimated beam. In our case, we've measured our beam spot for two different excitation wavelengths and corresponding lens choices. To do this, we couple our optical fiber into our assembly but mount no sample. We then mount a knife edge, in this case a fresh razor blade, to a three axis micrometer based positioning stage and scan the knife edge through the beam while measuring the beam power. We record the power as a function of knife edge position and get a curve similar to figure 2.6. We take the position of 80% power and 20% power as the beam edges and define that as the spot size. For our laser wavelength of 780 nm and our choice of collimator and lens, we calculate a nominal spot size of 930 nm and measure a spot size of 1.1 micron. This difference comes from our assumptions about the lens and the fact that our lens is designed for optimal thin lens behavior at 830 nm so we have some chromatic aberration that is not considered. Repeating the same measurement with a laser excitation of 473 nm with an equivalent lens, we get a spot size of 510 nm. This illustrates that we have near diffraction limited resolution using this assembly.

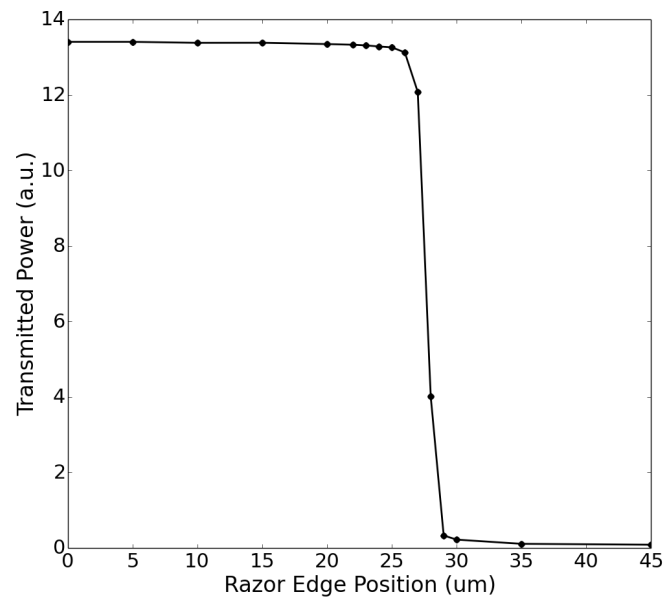


Figure 2.6: Spot size Measurement with Knife Edge: Here we plot the transmitted power of our beam as a razor blade edge is scanned through the waist of focused spot at its minimum diameter. The razor is mounted on a 3 axis micrometer based translation stage and cuts were taken around the focal point to determine the minimum spot size. The position difference between the the 87 % max transmitted power and the 13% max transmitted power gives us the gaussian spot size.

2.3 Sample Positioning and Optical Scanning

A desired advantage of optical techniques is the great spatial resolution that is possible compared to transport or bulk thermodynamic measurements. As we've shown in the previous section, we can get near diffraction limited spot sizes with our optics. Actually achieving spatial resolution for a measurement requires the ability to either position our sample with respect to our fixed optical geometry or to change our optical geometry. We rely on both of these factors as we have both a nanopositioner stack for our sample mount and we can scan the position of the optical spot using our piezotube based focusing lens holder if we so choose. Our sample holder geometry is shown in [figure 2.1 B]. This sample holder is mounted to a three axis nanopositioner assembly. This assembly is composed of an attocube ANPz101 nanostepper and two orthogonally mounted ANPx101 nanosteppers. These steppers give us a 5 mm scan range in each dimension with 50 nm step precision at room temperature and down to a 5 nm step precision below 4.2 K. They can move up to a 100 g load with the total assembly. As you can see from [figure 2.1 B], these nanosteppers are bolted to a copper base plate and this base plate is then attached to the optical mounting sleeve with 3 copper plates. These plates are as thick as they can be to still fit within magnet bore, as the mounting of the attocubes needs to be rigid for them to work.

These attocube nanosteppers function on the principle of stick-slip motion, where the mobile part of the positioner travels along a rod fixed to a piezoceramic stack as voltage pulses are applied to that stack. These voltage pulses are approximately sawtooth-shaped, so during the relatively slow ramp of the pulse the mobile part of the positioner moves with the rod through a frictional

coupling between the rod and mobile plate. The nominally instantaneous decrease in voltage causes the positioning element to slip along the same coupling, and the direction of travel is set by the pulse shape in time. The amplitude of the step is nominally set by only the temperature of the piezoceramic and the amplitude of the voltage pulse, though in practice other factors including the scan history and resistance of the electric connection to the attocubes also play a role.

In order to characterize the utility of these steppers in our setup, we mounted an AFM calibration grid from Anfatec (UGM02) onto our sample holder mounted to our nanopositioners. As is shown in figure 2.7 A, this grid has a center with regularly spaced 1 micron square features surrounded by a set of arrays of 2×100 micron trenches with a 4 micron pitch. These trench arrays are separated from each other by 3.5 micron gaps. SEM images of the center portion of this grid from its manufacturers, shown in figure 2.7 B, show that the side walls of the etched features are effectively sharp compared to our spot size and that the features are slightly rounded. We align the center of the grid to the laser spot by eye with the sample out of focus using the nanosteppers to position the sample stage in x and y . We next bring the grid into the focal plane of the focusing lens using the z -axis nanopositioner by monitoring the back coupled power at the 90% reflected channel of the 90/10 beam cube. As mentioned before, the power is maximized when the sample is positioned at the focal plane of the lens. We then record the reflected power while stepping the x and y -axis steppers generating an array of optical powers as a function of step number. We convert this into an image, and compare this image to the known geometry of the AFM calibration grid to back out the step size for a given applied voltage pulse to the nanostepper. Figure 2.7 C shows one of these images where we

can see the pattern of the calibration grid, as well as certain apparent defects. The contrast of our image comes either from changes in the sample reflectivity or changes in the optical back coupling due to changes in the sample surface height. In the case of this calibration grid designed for AFM, we are resolving the difference between the top surface of the features and the bottom surface of the trenches. The light features are those in focus and the dark features are those out of the focal plane. By taking scans at different sample z-heights, we can test our ability to resolve differences in z-position. We see a swap in contrast, with the light regions becoming dark and the dark regions becoming light with a single step of our z-axis nanopositioner. The AFM calibration grid has features with a 58 nm step height, so this is consistent with the stated step precision of the attocube ANPz101 at room temperature. From figures 2.7 C and D, we see some rounding of nominally square or sharp features. We are effectively seeing an image that convolves our spot size with the feature shape, and our resulting images are consistent with our measured spot sizes. In figure 2. 7 C the $1\ \mu\text{m}$ checkerboard region shows that we are seeing contrast between the individual square features in the array without resolving them fully. Weve demonstrated contrast from different focal planes, but we can also resolve regions of varying reflectivity. For example, we can image the metal leads or metal alignment marks on a sample allowing us to find specific locations on a relatively large sample.

With a scanning point microscope, the motion of the sample holder dictates the spatial relationship between points in an image. Any non-uniformity or hysteresis in nanostepper motion is going to give us effective aberrations or defects in our image generation and can potentially change our sample location from scan to scan. With these attocube steppers, weve experienced two major issues

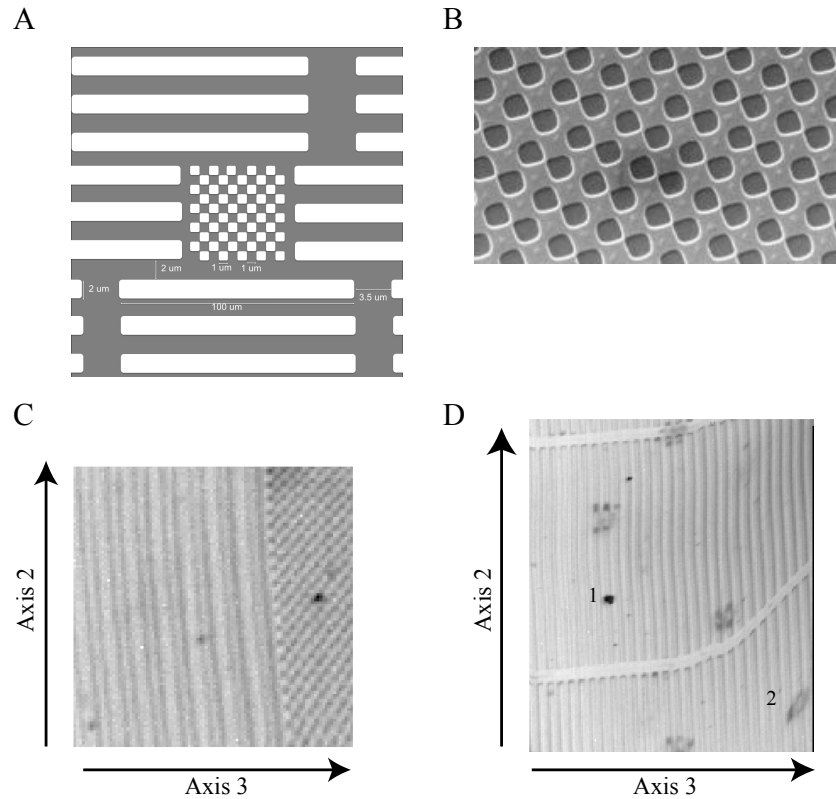


Figure 2.7: Images and Schematic of an AFM Calibration grid : (A) Illustrates a schematic of the layout of the Anfatec UGM02 AFM calibration grid we used for image calibration. (B) A SEM image of the center 1 μm by 1 μm checkerboard region in the center of the calibration grid provided by the manufacturer. The feature edges look sharp on the scale of our spot size. (C) 100 step \times 100 step scanned image of the border between the checkerboard and linear array regions of the calibration grid with a 50 V step size which corresponds to a 400 nm step size at room temperature. (D) 200 \times 200 scan of linear array region of calibration grid showing slipping in axis 2 and multiple defects. Location 1 corresponds to a symmetric defect, while location 2 illustrates a defect that is clearly stretched along with the axis slipping.

with relying on them for sample positioning during image formation. The first issue comes from our scan algorithm. We traverse a two dimensional space by stepping slowly in one direction for one axis (axis 2), then quickly taking the same number of steps back to the original position. We next take a single step in the orthogonal dimension (axis 3) and repeat this procedure while recording an optical power for each position. After weve completed our travel in axis 3, we quickly take the same number of steps in that axis in the opposite direction. In this manner, we nominally map out a space with an optimal scan speed while returning to our initial position. Unfortunately, we see a change in the step size with either scan speed or scan direction. This means that during our scan, our initial axis 2 position is changing for each subsequent scan which gives us an image aberration where feature seem to be drifting on a diagonal, as is shown in figure 2.7 D. This also means that at the end of our scan we will end up in a different initial sample position. Weve attempted to account for this by changing the return step rate (the frequency of pulses from the controller), with no obvious repeatable success. This seems to be an issue with step direction or step hysteresis, so we can account for this by changing the number of steps that we take to return to our initial axis 2 position. To do this we must have some knowledge of what our image should look like, so we can rely either on images taken with a different microscope or on assumptions we make about the shapes and positions of surface defects within our scan range. The defect case is more interesting, as we assume that there should be particulate contamination on our surface and that this particulate contamination should have an array of sizes, including many particulate defects well below our spot size. Defects or particulate contamination below our spot size should look circular in our images. As you can see from the images in figure 2.7 C and D, this seems to be a safe

assumption for scan ranges on the order of 10 microns and above. We take an initial scan and note the defect positions and shapes. Sometimes, as in the case of figure 2.7 D, we see clear evidence of axis slipping in the shape of the defects in the initial image and we can attempt to account for it. Here, we see that in location 1 where we have minimal distortion of the calibration grid features we have a circular defect while in location 2, where we see clear distortions of the calibration grid we see a defect that looks stretched. In general, when there is not a known sample appearance stretched defects indicate axis slipping. If we see no stretched defects, we must take a subsequent image and note the position change of the defects with respect to the step number. In this manner, we can iteratively adjust the number of steps we take in the backwards direction for both axis 2 and 3 to maintain our initial position and step uniformity. While we have this work around, this can be a very inconvenient process and can take large amounts of time. From this procedure we have determined that we generally slip from 1 to 4 steps in 40 steps (50-100 nm in 20 micron), which amounts to large changes in axis 2 position over the course of a 10 micron scan. For axis two, this means a 40-160 step (20-80 micron) change in initial position by the end of a scan. Axis 3 is less sensitive, but after multiple scans this issue becomes apparent. The direction of the slip also seems to always correspond to larger steps in the reverse direction.

We also have a secondary issue that relates to the function of the attocubes themselves. This step direction issue most likely stems from the hysteretic behavior of the frictional coating on the rod (mentioned in conversations with attocube engineers). While the piezoceramic has a uniform displacement during a pulse, the step motion of the positioner depends on the friction between the mobile element and the rod, which in turn is set by this coating. This coating

is designed for optimized step repeatability and step size linearity but it is not perfect and the motion of the slider along the fixed rod can modify the coating. Aside from altering the step size in opposite directions, repeated scanning of the same area can effectively jam the range of the attocube so you cannot leave that region. This shows up as either an inability to move the attocubes beyond this range at all or as the attocube drifting back to its original position when you try to scan a new location with a much larger step disparity between forward and backward travel. If you are in a state where you can move the attocube, but it drifts back to its initial location, then repeated scanning of the new location with a large step number compensation can fix this. This procedure ends up being rather persnickety, but it does work with some effort.

If the attocubes get physically jammed in a region, then things are more serious. The proposed reason that this happens according to the engineers at attocube is that repeated scanning of the same region builds up a physical notch or edge in the coating which prevents motion. The first recourse is to slowly increase the pulse amplitude and number of pulses attempted while trying to take steps out of the jammed region. It is possible that larger pulses will jump you out of the jammed region, and you can then move around to new location. It is also possible to be in a state where no electrical signal applied to the positioners can free them. If this is the case, you must remove the attocube stack from the microscope and manually unjam the stuck position with a force from your hand. This process is incredibly nerve wracking for fear of breaking the positioners, but it is the only way to fix them if they become badly jammed. According to attocube, this behavior is more likely to occur at low temperatures or during temperature cycling, which renders this behavior even more inconvenient and frustrating. Attocube has found that running the positioners through

their entire range of motion at 1 kHz pulse frequency on a regular basis can prevent this. The suggested frequency is on the order of once per week. The idea here is that running the mobile element along the entire range of the rod with a constant pulse rate and amplitude will uniformly smooth the coating and remove the non-uniformities that cause the jams. This seems to work, though it can be exceedingly inconvenient if we need to work on a specific portion of the sample for long times.

The solution to these issues is to use the attocubes as course positioners while relying on our piezoceramic tube based lens holder for imaging once we've found our desired location. In this scanning motif we drive our piezoceramic tube with a large externally applied voltage and record the optical signal as a function of the tube bias. We use a similar scan algorithm where we apply a sawtooth pulse form to one axis of the tube while slowly ramping the bias on the other axis to cover the scanned area uniformly. We generate the large voltages needed to manipulate the piezo tube over its entire range by sourcing a 10 volt signal from a NI-DAQ and then amplifying this signal with a homebuilt amplifier circuit, which is shown in figure 2.8. To drive our piezo tube, we need four channels where we source opposite voltages to opposite quadrants of the tube electrodes. We take in an x signal and a y signal from the DAQ, then route each signal into two independent amplification channels: an inverting channel and a non-inverting channel so we are using the same drive signal for our $\pm x, y$. In this manner, we don't need to worry about issues of timing the signals between our electrodes.

As shown in figure 2.8, our amplification circuit uses two op-amp stages with a low power OP-07 setting the polarity of the input to the high voltage

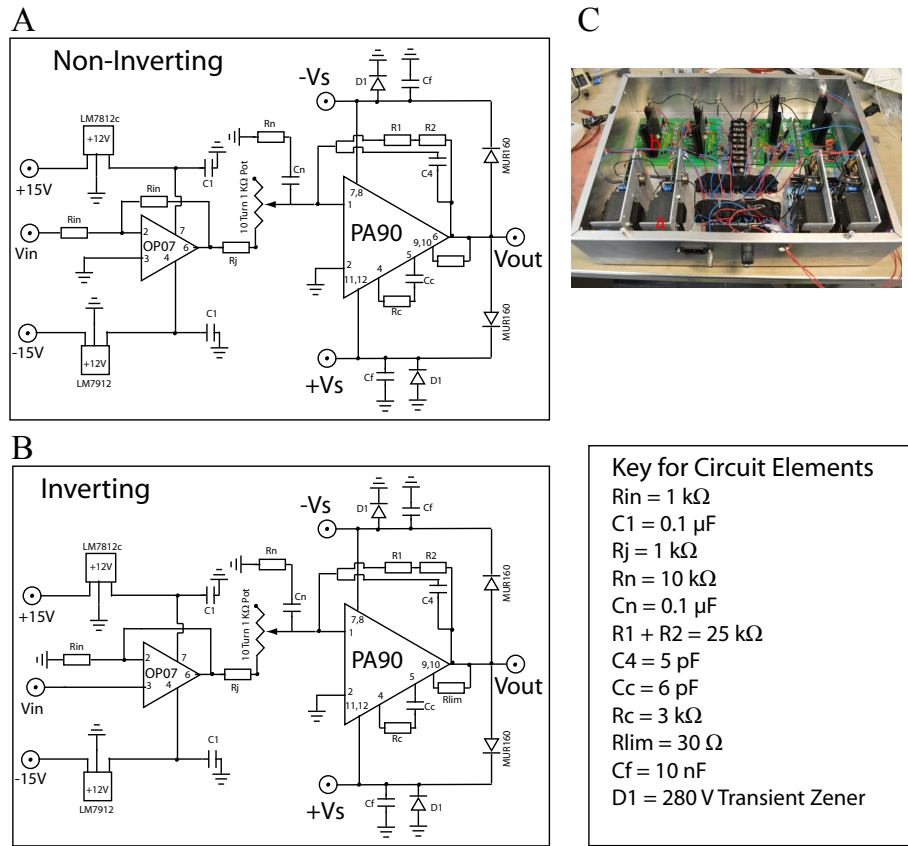


Figure 2.8: Circuit Diagram and Layout for Piezotube Amplifier : The circuit diagrams are labeled with lettered elements, which are described in the key. (A) The circuit diagram for the non-inverting amplifier channels. (B) Circuit diagram for the inverting amplifier channels. (C) Photo of the assembled amplifier box with 4 DC power supplies labeled as (a) and 4 amplifier circuits, labeled as (b). There are 4 amplifier circuits in the box, where a pair of inverting and non-inverting circuits shares a common input signal. Each set of amplifiers has its own pair of power supplies.

Apex PA90 amplifier. This high power amplifier has a rating of 400 V and 200 mA with a slew rate of 300 V/ μ s and is particularly designed with the application of driving piezoelectric transducers in mind. We also use the EK11 evaluation kit boards designed for these amplifiers to make the actual amplifier boxes easier to assemble. The purpose of the OP-07 is not only to set the signal polarity, but also as a protection circuit for the high power amplifier. If we have any sort of power surges or shorts that would blow the PA90s, the OP-07s should blow first and save the high power elements. We also have a protection diode on the output from the high power amplifier so that any voltage that might develop on the output from the amplifier is shunted to ground once again protecting the PA90s. This is critical for driving piezoelectric elements, as accidental strains in the device can lead to large voltages which might destroy the amplifiers. To power our amplifiers we have separate low voltage and high voltage sources. We use two Elenco Precision XP-100 battery eliminators to source ± 15 V for our elements that need low voltages like our OP-07s. For our high voltage channels, we have 4 IHB155-0.12 AC to DC convertors from International Power which allow us to source ± 155 V from the 120 V AC line for our high power amplifiers. We can drive two amplifiers off each pair of IHB155-0.12. One important point of note is that we use a potentiometer to set the gain of the power amplifier so we can balance the individual amplifiers for a given channel to account for any variation between circuits after assembly. We calibrate the gain of the amplifiers so that for a given input channel, the amplified output has the same voltage within the measured noise floor of the amplifier.

As we transduce the electric signal from the DAQ into motion at the end of the piezotube, the electronic performance of our amplifier circuit sets our positioning stability for our optical spot. We need to consider how electronic

noise from our source will add potential noise or uncertainty into our imaging. In our setup with an optical spot size on the order of 1 micron and with a scan range on the order of 40 micron for a given axis, we think about the precision needed in our electronics by considering what kind of voltage variation would give us a spatial uncertainty 1% of the diameter of our spot at the edges of our scans. This choice is an extremely conservative cutoff. In this case, that would correspond to 10 nm in 40 microns, so that even at the end of our scan range we would have a low uncertainty in the piezo tube position. We can assume that linear changes in the voltage will cause a linear change in the position, so we can say that for a 150 V output we need less than 37.5 mV of rms noise and for the 10 V output from our DAQ we need less than 2.5 mV rms. The PA90s have below $1\mu\text{V}$ rms of noise over their entire range while our DAQ has a noise spec of $100\mu\text{V}$ rms. We've looked at the output from our DAQ through the amplifiers and have confirmed that our noise floor is well below 40 mV at max input voltage from the DAQ.

We've mounted the same Anfatec UMG02 calibration grid in our sample holder and imaged it using the piezotube based lens holder. Figure 2.9 A shows an image of the 3.5 micron spacing between two of the arrays of 2×100 micron trenches. We subsequently cooled the calibration grid and optics down in the dilution refrigerator and recorded images of the calibration grid as the piezoelectric coefficients of the tube changed with temperature. Figures 2.9 B and C show the reduction in scan range that we see as the piezoelectric coefficient drops off. Using our maximum amplifier of voltage amplitude of ± 150 V, we go from a one axis scan range of about 40 microns down to a scan range of 6 microns below 4 K, which is expected from the stated temperature behavior. We also see no image distortions when we apply a magnetic field up to 9

T. The apparent rounding off of the patterns in the upper and lower portions of these images is set by the saturation of the high gain amplifiers for that channel. When these images were taken, we had blown up the optimal amplifier for one of the channels that we wanted to use and were forced to replace it with a lower voltage limit version where the non-inverting channel was saturating at ± 100 V. This doesn't alter the demonstration of our scan capabilities for this setup, as the piezo tube still behaves as expected for a properly sourced bias. In principle one might think that the slight geometric coupling between x-z and y-z displacements for this piezo tube or the slight tilt that is induced as the lens moves in space should introduce image distortions. We don't observe this in our images due to the very small effects in our geometry where the change in length for part of the tube is scaling linearly with the tube length while the x and y displacement is scaling with the square of the length. We also are using a very large NA lens, so a slight tilt does not alter the collection geometry very much. If this were an issue in our setup we can nominally also apply a DC bias to the attocube nanopositioners for controlled scanning. Other groups have reported this for their own microscopy setups, though we have not yet attempted this [7]. If we were to attempt this, we would need to be much more careful with our amplifier design, as the attocubes use a different piezoceramic geometry which would be damaged with large negative biases and attocubes data sheets for our positioners do not give us the limits.

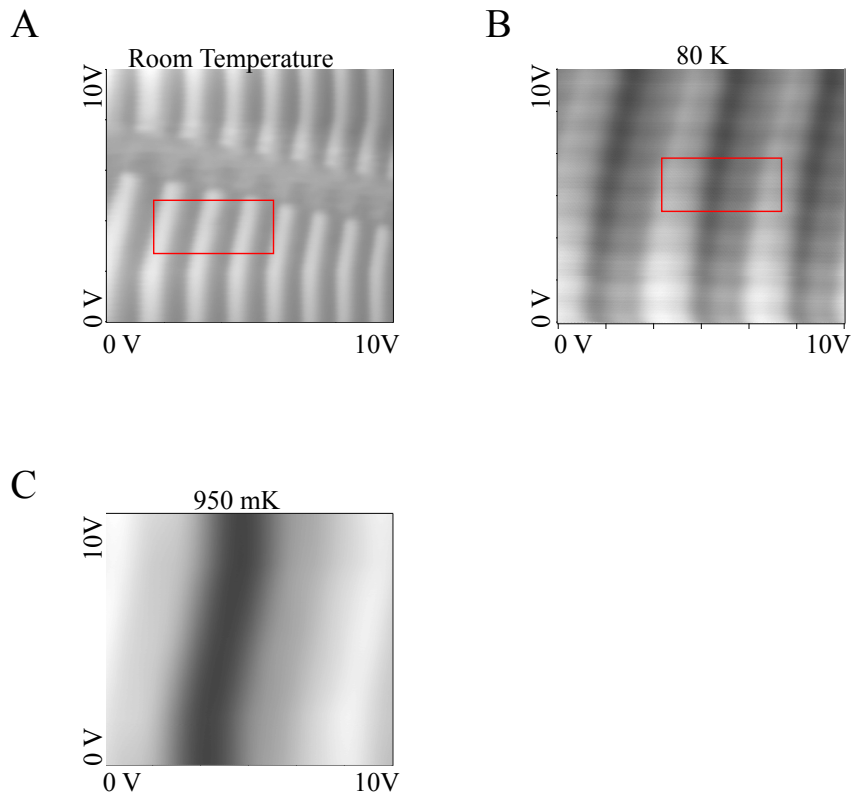


Figure 2.9: Temperature Dependence of Piezotube Imaging: These are images taken of the Anfattec UGM02 AFM calibration grid using our piezotube based objective lens holder in our dilution refrigerator during a single cool down cycle. (A) was taken at room temperature with an evacuated vacuum space. (B) was taken at 80 K while cooling the sample to 4 K using the He bath and exchange gas. (C) was taken at 950 mK while circulating the mash with an evacuated vacuum space. The red box in (A) corresponds to the scan area of (B) and the red box in (B) corresponds to the scan area in (C). The apparent image distortion in each scan is due to the amplifier saturation explained in the text.

2.4 Sample Thermalization, Transport Measurements and Low Temperature High Magnetic Field Constraints

We've explained our how our optics work as well as the sample positioning aspect of our setup, but the utility of this microscopy platform is in its ability to function at temperatures below 4.2 K and magnetic fields up to 9 T. Our optical assembly and our imaging principles are the same for either our dilution refrigerator based setup or for our vector magnet dewar design, but we have different constraints for sample mounting, thermometry, and thermalization for the different microscopes. The principles are the same, but the dilution refrigerator adds significant limitations to our electronics choices and our geometric constraints. We must design a thermal linkage between the sample and the mixing chamber in the dilution refrigerator, while we can rely on helium exchange gas to link the sample to the helium bath for our 4.2 K setup in the vector magnet dewar.

As is shown in figure 2.1 B, we start with a copper cold finger that threads directly into the mixing chamber of the dilution refrigerator. This cold finger extends down towards the field center, where we then use three thick copper plates to attach the optical housing sleeve to the cold finger. The separation between the end of the cold finger and the optical housing sleeve leaves room for the fiber termination so we do not need to bend the fiber too much. Figure 2.10 shows that we have a fourth plate that extends from the cold finger all the way along the optical sleeve and then down to the field center. This is our sample thermalization plate.

Thermalizing a sample sitting on a sample holder to the mixing chamber,

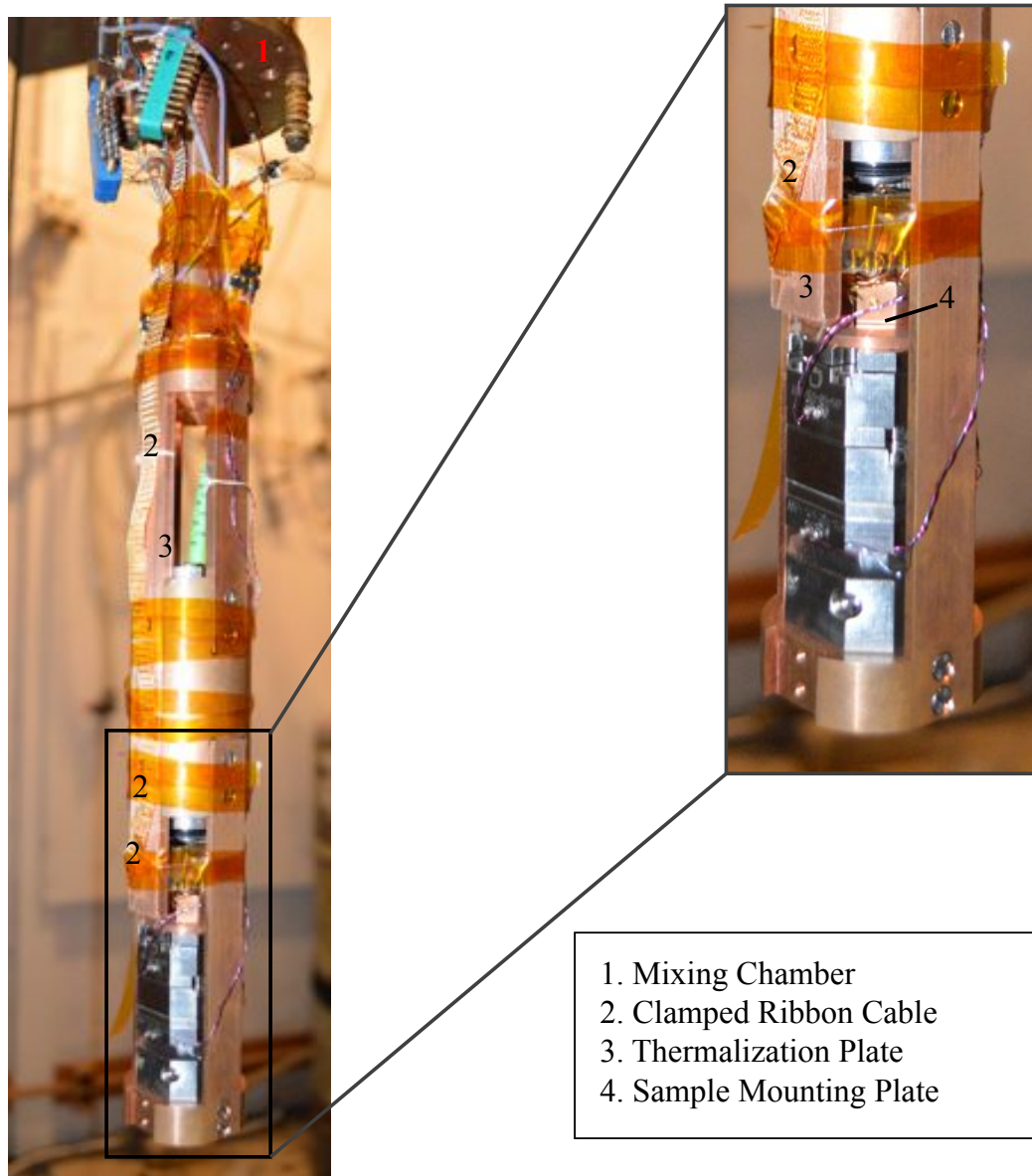


Figure 2.10: Optical Microscope Insert with Thermalized and Clamped Sample: Photograph of a mounted sample after it has been thermalized and all the wires have been tied up and strain relieved for cooling down to 4 K. The Kapton tape and dental floss are used to prevent stray wires from causing thermal shorts between the insert and the vacuum can. The ribbon cable is mechanically fixed to the thermalization plate with dental floss, and with GE varnish to enhance the thermal contact.

while still allowing for our sample to move in three dimensions at the field center is difficult. We cannot rely on the attocubes as a thermal linkage between our sample since the titanium will turn superconducting below 400 mK [42]. We settled on a scheme where we rely on the electrical lines for our sample holder to act as the mobile element of our thermal link. We keep the length of the wires at a minimum, since this is the weakest part of our thermal linkage. As shown in figure 2.10, we thermally clamp a 12 twisted pair cryogenic ribbon cable from CMR direct to the end of the sample thermalization plate so that we only have 0.5 of wire length between our sample holder and our thick copper. We then keep the ribbon cable in close thermal contact with the copper body of the microscope all the way up to the mixing chamber.

Our sample is mounted on a 28 pin ceramic chip carrier which fits inside one of the standard 28 pin plastic chip sockets that are generally used in the group, shown in figures 2.11 A and B. We then modify this chip socket so that we can mount it to our sample positioners. This chip socket/chip carrier mate gives us good thermal and electrical contact between the pins of the socket and the chip holder down to mK temperatures. Our sample holder assembly is shown in figure 2.11. We drill a hole in the center of the base of the socket and use a 0.25 flat head 2-56 brass screw to attach the sample holder to a copper post. This copper post then fits into a groove on the sample mounting plate, which is bolted directly to the attocube positioning stack. We can attach the copper post to the sample mounting plate either through the threaded hole on the copper post or with set screws in the mounting plate. Twenty-four pins of our socket are wired up to the cryogenic twisted pair ribbon cable, with the four remaining pins connected to un-braided 38 gauge copper wire for an extra thermal linkage to the sample thermalization plate. This geometry lets us remove the sample

holder from the microscope without having to remove the entire attocube stack or remove the optical assembly. When the z-axis attocube is fully retracted, the combined chip socket, copper post, sample ribbon cable, and thermalization plate can be removed together.

This use of the wires to thermalize the sample is not ideal for thermal contact, and we cannot assume that our mixing chamber will be at the same temperature as the sample. We need to measure the sample temperature independently, so we mount a 5.6 k Ω calibrated ruthenium oxide resistor to the ceramic chip holder to use as a local temperature sensor. This mounting geometry is shown in figure 2.11 C, where we have attached the resistor to the outer edge of the chip holder using GE varnish. We use a small piece of lens cleaning tissue to electrically isolate the resistor from the chip holder, but the GE varnish saturates the tissue increasing the thermal contact between resistor and the chip. We connect the resistor to 4 pins of the chip holder and use our AVS-47 b resistance bridge to monitor the resistance change with temperature. For our current wiring setup and mash composition we achieve a mixing chamber base temperature of 74 mK. While the mixing chamber is at 74 mK, we measure a sample temperature of 110 mK. These mixing chamber and sample temperatures are measured without adding the microwave shield to the cold plate of the dilution refrigerator. This microwave shield should fit around our microscope, but we have not cooled down with it on to test the true minimum temperature for our sample. As we sweep magnetic field, we see eddy current heating at both the mixing chamber and the sample temperature sensor. We also see some magnetoresistance of our sample temperature sensor. This is on the order of 5% of the total resistance at 9 T, but at base temperature that corresponds to an error of only a few miliKelvin. This magnetoresistance is linear and we can account for

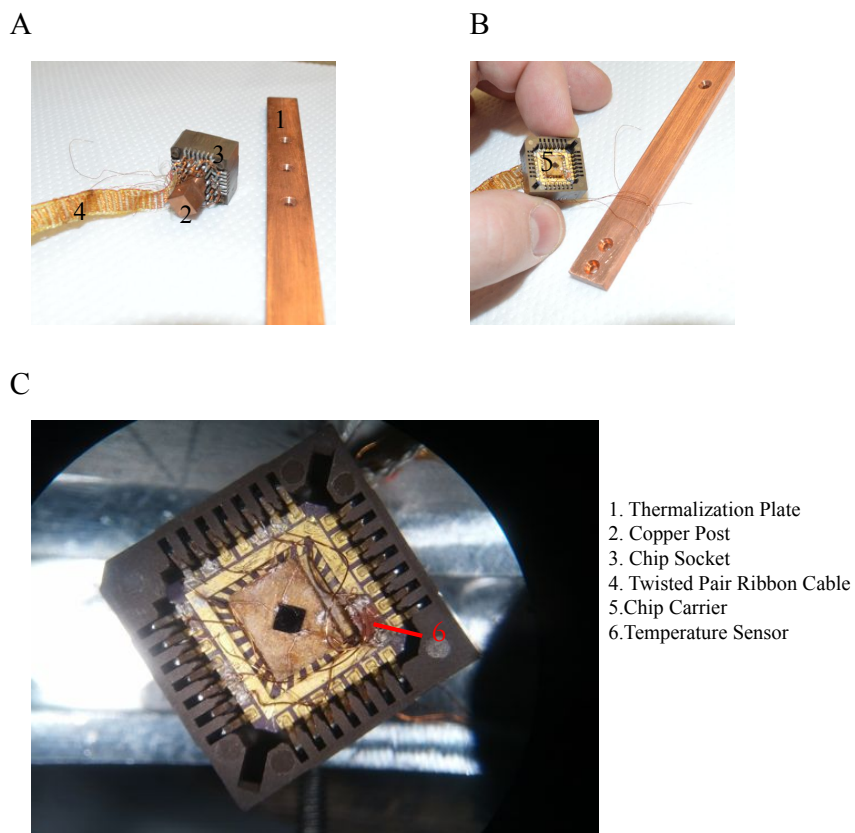


Figure 2.11: Sample Holder and Thermalization Plate. (A) Image of chip socket showing copper mounting post and cryogenic twisted pair ribbon cable used for thermalizing and electrically connecting to sample. The cable is clamped to the thermalization plate for thermalization to the mixing chamber. (B) Image of chip socket showing chip carrier position. (C) Image taken through stereomicroscope of mounted sample on chip carrier. Our mounted temperature sensor is shown, which allows us to measure the sample temperature independent of the mixing chamber.

it by comparing to the mixing chamber temperature sensor, which is in a field canceled region of the dewar. One of our concerns was sample heating from our optical excitation, which is limited by our recollection efficiency of the light back into the optical fiber and the sensitivity of our detectors. We are able to supply optical powers up to of $1 \mu\text{W}$ to the sample with no measurable sample heating at the sample temperature sensor, but above $1 \mu\text{W}$ we start to see sample temperature increases when we unblank our laser. We generally keep our excitation power below 10 nW to avoid any issues. We see no issues of optical path changes or changes in recoupled power as we ramp the magnetic field to 9 T.

2.5 Conclusions

We have designed and built a modular scanning confocal microscope that functions with sample temperatures down to 110 mK and up to magnetic fields of 9 T. We also have a complementary microscopy using the same mechanics and optics that functions at 4.2 K inside a 7 T \times 1 T \times 1 T vector magnet. These setups use room temperature light generation and optical elements with standard mounting geometries so the optics can be quickly switched to optimize for various measurements schemes. We have not discussed the ways we can analyze the light that comes back out of the fridge, as we will discuss this related this to two different systems in later chapters. In particular we will discuss the use of these optics for polarization microscopy of $\text{Sr}_3\text{Ru}_2\text{O}_7$ in chapter three and we will discuss polarization resolved magnetoluminescence of CdTe and MoSe₂ in chapter four.

CHAPTER 3

POLARIZATION MICROSCOPY OF BILAYER STRONTIUM RUTHENATE

We have described our optical microscope in terms of how we couple light into our microscope and back out to our optical table, but we have a full range of options on how to analyze the properties of that light. We've built a detection setup that allows us to analyze the polarization of the light after it has interacted with our sample and been coupled back into our optical fiber. Changes in the polarization of light after interacting with a sample can be used to study magnetic properties of the sample through the Kerr or Faraday effects [41]. Birefringent samples will also alter the polarization of light, which will show contrast between areas of a sample with different symmetries [41]. As discussed in the introduction, $\text{Sr}_3\text{Ru}_2\text{O}_7$ shows an electron nematic phase transition at low temperature and high magnetic field and this electron nematic phase could result in a measurable linear polarization rotation of a reflected beam. Our dilution refrigerator microscopy platform allows us to access the relevant magnetic fields and temperatures to study this electron nematic phase.

3.1 Polarization microscopy in our microscopes

Polarized light microscopy in our case refers to interacting polarized light with our sample, then collecting the reflected light from our sample and analyzing the polarization state of that light after it exits our optical fiber. We need to first generate and couple polarized light into our optical fiber. As is explained in Chapter 2, section 1, our diode laser source generates a polarized beam due to the nature of the diode heterostructure. Our polarizing beam cube in our optical coupling path cleans up the polarization of the laser to a polarization extinction

ratio (ER) of 1000:1 (30 dB) for the transmitted polarization. The ER is defined in Penninckx et al. as the ratio of the optical power in the desired polarization state to the power in the orthogonal polarization state[43]. The launch wave plate, shown in figure 2.1, allows us to rotate the linear polarization to couple an arbitrary linear polarization into our fiber. The inclusion of a $\frac{\lambda}{4}$ wave plate at the same place allows us to couple arbitrary circular or elliptical polarizations into the fiber. We find that for an isotropic single mode fiber, the coupling efficiency is generally independent of polarization state.

We detect the polarization state of the reflected light using the setup shown in [Figure 3.1]. We take the 90% reflected channel from the 90/10 beam cube and reflect it into the blacked out box containing our amplified photodetectors. Here, we use a second polarizing beam cube to split the polarized light into orthogonal components. We then measure the power in the two paths using paired amplified photodetectors. We use two Thorlabs PDF10A detectors which have an amplification of 1×10^9 kV/A and a responsivity at 780 nm of 0.528 A/W. We mount these detectors on micrometer stages and optimize the detector area position to maximize the response in each channel for an unpolarized excitation sent through the polarizing cube. The high sensitivity of these detectors makes it incredibly important to minimize the background light, so we house our detectors in a blacked out box with a small aperture optical access. We also carefully measure the detector dark counts, and typically achieve dark voltages (measured as the detector signal with the beam blanked) of 5-10 mV with an rms noise of 3 mV. We add a quarter wave plate and half wave plate before the polarizing beam cube so we can fully map out the polarization state of the light leaving the optical fiber. Initial room temperature bench top tests illustrated that we could couple arbitrary polarizations into a single mode fiber and dis-

tinguish these polarizations with our detection scheme, though changes in the fiber strain state also alter the polarization of the light leaving the fiber.

In the case of $\text{Sr}_3\text{Ru}_2\text{O}_7$, there are multiple possible optical responses as we traverse the magnetic field and temperature phase space. Previous optical reflectivity measurements have been made on $\text{Sr}_3\text{Ru}_2\text{O}_7$ from 450 K to 12 K with no applied magnetic field and show that the in-plane optical conductivity is Drude-like down to 12 K with a temperature independent plasma edge at $\omega_{\text{pD}} = 12000 \text{ cm}^{-1}$ (833 nm) [44]. No optical measurements on $\text{Sr}_3\text{Ru}_2\text{O}_7$ in its nematic phase have been reported elsewhere. Since the reflectivity in this Drude picture comes from the conductivity of the sample, we might expect that an anisotropic resistivity will lead to differential reflectivities for the orthogonal E_x and E_y components of the electric field of the optical excitation. This would in turn lead to a linear polarization rotation, which we can detect in our setup. We can estimate a response of a few μRad of polarization rotation if we assume that the resistivity anisotropy ratio comes directly from a difference in scattering times. This picture is potentially very naive, as it does not treat the underlying microscopic origin of the change in resistivity, which could actually be due to scattering from the predicted domain walls. It also does not consider any magnetic effects.

Aside from reflectivity changes, we might expect that the magnetization of $\text{Sr}_3\text{Ru}_2\text{O}_7$ would also lead to magneto-optical effects. In particular, the metamagnetic response explained in [12] suggests that there should be a polarization change due to the Polar Kerr effect [41]. The relevant materials parameter for this system is the wavelength dependant Kerr angle describing the magnitude of polarization rotation for a given magnetization change. The Kerr angle for $\text{Sr}_3\text{Ru}_2\text{O}_7$ is unknown, though Kerr rotations for the $n=1$ and $n=\infty$

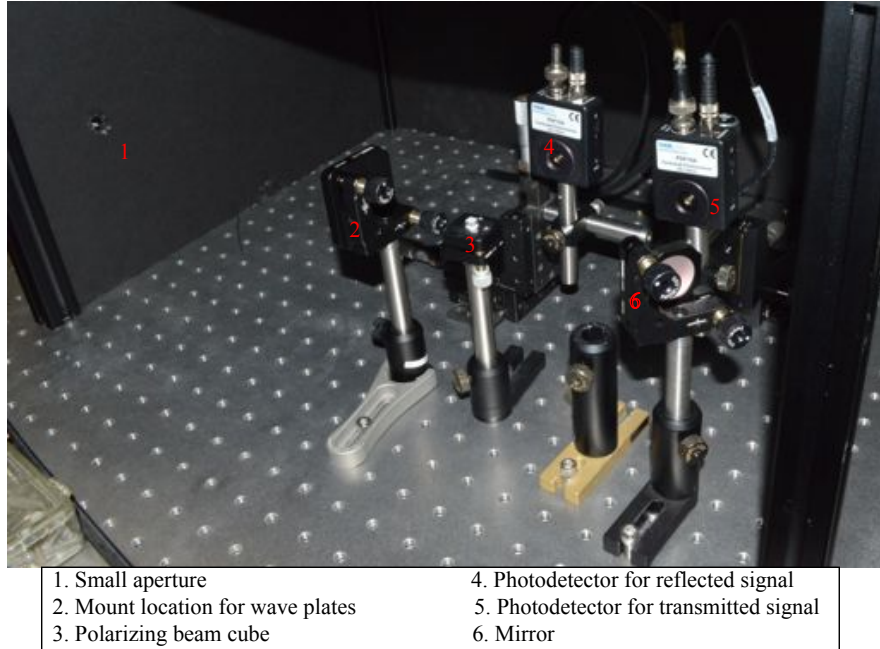


Figure 3.1: Photo of Polarization Detection Setup. A photo taken of our polarization detection setup. Location (1) has a 3 inch by 0.25 inch lens tube mounted through the wall of the dark box. The high aspect ratio gives us rejection of light that is not collimated along our beam path. Location (2) is a stand-in for where we mount our $\lambda/2$ and $\lambda/4$ detection wave plates. We use a mirror (6) so that both photodetectors are facing in the same direction to eliminate differences in background signal from room light or reflections from the room walls. During operation there is a 4th wall closing out the dark box as well as a curtain over the box to reduce light leakage. Both detector are mounted to 3-axis micrometer stages for positioning.

Ruddlesden-Popper sister compounds Sr_2RuO_4 and SrRuO_3 have been reported using Sagnac interferometry [45][1]. Klein et al. may be more relevant as it reports a large Kerr angle of 0.89° for a fully magnetized 300 nm thin film SrRuO_3 at an excitation wavelength of $\lambda = 830$ nm. This large magneto-optical coupling is attributed to the spin orbit coupling of the Ru d-orbitals and these Ru d-orbitals also lead to the magnetization of the $\text{Sr}_3\text{Ru}_2\text{O}_7$, so its possible that we can expect a similar magnetization dependent Kerr rotation in our system[45]. This magnetization dependent polarization rotation would lead to a potential background for any linear birefringence measurement, though it also serves as a potential secondary means for detecting the nematic phase transition, as the magnetization shows kinks upon entering the nematic phase as well [11]. There is no expected magnetic domain formation in the nematic phase, as explained in [13], so a spatial variation in a polarization response should be due to any differential reflectivity change and could serve as a potential means to tease the magnetic response out from a resistivity based response. Further theoretical treatment of any optical response is needed that considers both the microscopic picture of the electron nematic ordering and the underlying magnetic signatures.

3.2 Characterization and Mounting of the $\text{Sr}_3\text{Ru}_2\text{O}_7$ Sample

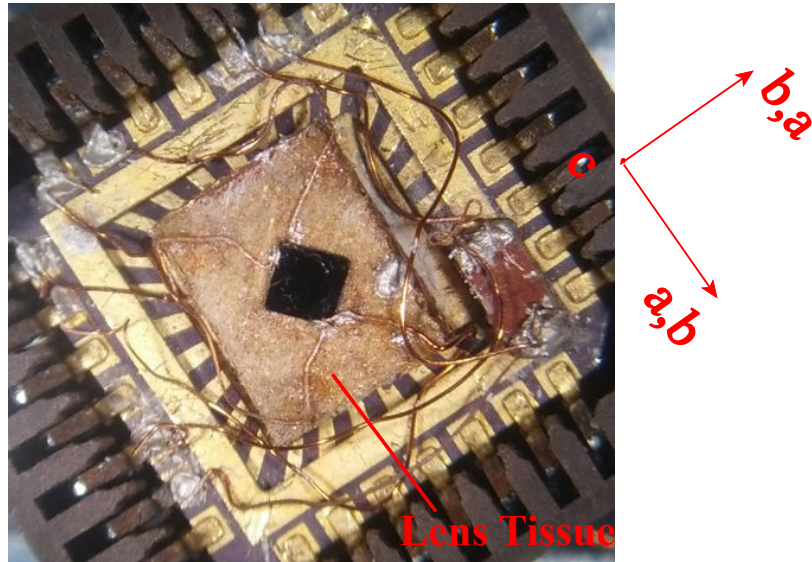
We received a single piece of image furnace grown, single crystal $\text{Sr}_3\text{Ru}_2\text{O}_7$ from Andrew Mackenzie's group at St. Andrews which they measured to be below the required ρ_0 value to see the electron nematic phase. This crystal is grown with the methods described in [14]. The initial single crystal had a cuboid shape with dimensions approximately 1 mm x 1 mm x 300 μm . We need to know the

relationship between the sample shape and the underlying crystal symmetry. The sample is cleaved from a larger crystal, and the cleave face gives us the out-of-plane 'c' axis of the crystal. The in-plane axes have no obvious relationship with the shape of the crystal so we performed Laue diffraction using the CCMR Laue setup in Snee Hall. Due to the symmetry of the crystal structure, we can't tell the difference between the 'a' and 'b' crystal axes with this Laue detector. We can determine that 'a' or 'b' is aligned along the diagonals of the single crystal within the positioning accuracy of the sample stage.

We want to concurrently make sample resistance and optical polarization measurements, so we need to mount our sample to our chip holder without shorting to the chip carrier while still making good thermal contact between the sample and the chip carrier. As explained in [ref for nematic angle dependence], there is a dependence of the magnitude of the resistive anisotropy on the angle of the magnetic field with respect to the crystal axes and there needs to be a slight in-plane field component to see the resistive anisotropy at all. There is also evidence from single crystal dilatometry measurements that the in-plane field component changes the underlying nematic domain structure, which saturates with a field canted 10° away from the c-axis into a nominally single domain system[15]. We cannot rotate our field direction in our dilution refrigerator magnet, but we can tilt our sample. However, as we tilt our sample we also lose collection efficiency for coupling the reflected light back into our optical fiber. We settled on a 5° sample tilt which should show a strong resistivity anisotropy, should still be multi-domain, and will still allow us to collect enough light [15].

Figure 3.2 B illustrates our mounting geometry. To controllably tilt our sample, we machined a small copper plate with a 5° tilt between faces. This plate

A



B

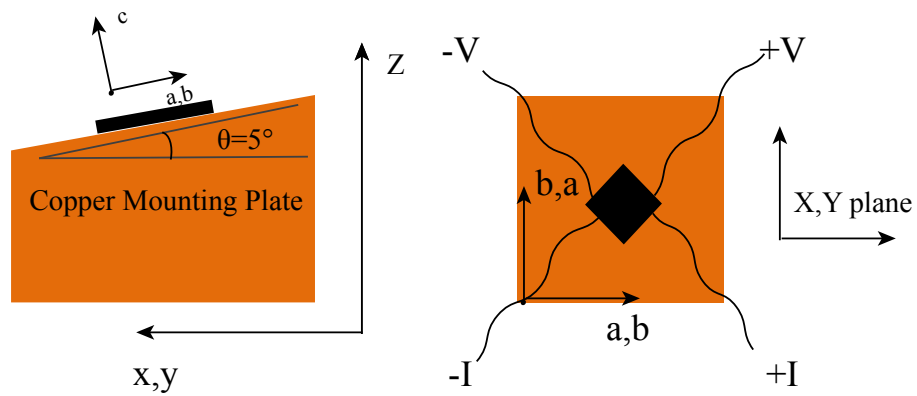


Figure 3.2: Laue Pattern and Mounted Sample Geometry. (A) Photo of mounted sample taken through a stereomicroscope. 40 gauge wires are epoxied to the sample and the sample is electrically isolated from the copper block with lens tissue show. (B) Diagram of copper plate geometry showing relationship between crystal axis and microscope axes. The magnetic field is applied along the microscope Z direction.

is attached to the chip carrier using silver paint, and we then mount our single crystal to the copper plate using GE varnish and lens tissue in the same manner that we described for the sample thermometer. The lens tissue electrically isolates the sample from the copper plate while the GE varnish maintains a thermal contact. Using the Laue measurements, we align the sample so that the tilt generates an in-plane magnetic field aligned with the 'a' or 'b' crystal axis, as is shown in figure 3.2 b. After we have the sample mounted to the copper plate and the chip carrier, we cleave the top surface off the sample to expose a clean surface. From Borzi et al., we see that the maximum resistance change on entering the nematic phase is for the in-plane magnetic field aligned along the current flow direction [13]. To fasten leads to the sample, we use the same method that the Mackenzie group uses to make their sample contact for their transport measurements, as explained by Andreas Rost. We position 4 stripped 40 gauge copper wires in a 4 point measurement geometry so that they make a press electrical contact with the sample and we tack them in place using GE varnish. For our crystal we position our leads at the corners of the sample, as shown in figure 3.2 A and B so that the current is flowing in the same direction as the in-plane component of the magnetic field. Once the GE varnish has hardened, we use H20E silver epoxy from Epotek to mechanically attach the copper leads to the sample and to enhance the electrical contact between sample and the leads. We cure the epoxy for 3 hours at 80⁰ C, which is the minimum cure temperature for this chemistry. We want to keep the cure temperature low to reduce any thermal stresses during cooling. After curing, we have a contact resistance between 15 and 50 ohms for each lead. We measure a room temperature sample resistance in this geometry of 17 m Ω which corresponds to an estimated resistivity of 300 $\mu\Omega \cdot \text{cm}$ and we see this resistance decrease linearly as the sam-

ple temperature is reduced to 80K, which is consistent with previously reported values for samples grown by this method[14].

3.3 Initial Measurements and Polarization Maintaining Fiber

We first cooled down our $\text{Sr}_3\text{Ru}_2\text{O}_7$ single crystal in our microscope using a non-polarization maintaining (PM), single mode optical fiber and a slightly different optical housing geometry where the optical fiber ran through the field center and had a 180° bend inside the IVC. We also used a fiber coupled 95/5 beam cube from Oz Optics instead of the free space coupled 90/10 beam cube described in section (A). This demonstrated two major issues to us, as the measured polarization of reflected signal from the sample was highly time dependent, with full $\pi/2$ linear rotations on the time scale of one to two minutes. We also observed fluctuations in ellipticity on the same time scale. We attempted to account for these rapid polarization fluctuations by sweeping our field through 0.1 T steps and resetting the initial polarization state of the detection wave plates before each sweep. As we swept magnetic field we saw changes in the polarization state of the reflected light, but none of these observations were distinguishable from the time dependent fluctuations at fixed field. The main issue here is that single mode, non-PM acts as a birefringent medium when there are small strains, defects, and temperature gradients in the fiber [46]. These small strains accumulate over a 10 m length of fiber and cause the state of polarization (SOP) at the exit of the fiber to be different from the SOP on launch. This birefringence is time dependent through mechanical perturbations of the fiber position and through temperature fluctuations, and while we can limit this by mechanically clamping the fiber we cannot eliminate the time dependent signal completely.

On top of these zero magnetic field effects, there is also a Faraday effect in the glass of the fiber and low temperature lenses that causes a time reversal broken polarization modification where the linear rotations of the polarization is given by $\theta = \nu Bd$ where θ is the rotation angle, ν is the Verdet coefficient of the medium (in this case the glass), B is the field component in the propagation direction, and d is the distance the light travels through the medium [41]. This is a linear effect that we were planning to subtract off, but it still presents a significant background signal. A typical Verdet constant for optical glass at a wavelength of 780 nm is on the order of $5-10 \frac{\text{Rad}}{\text{Tm}}$ [47].

The solution to issues of polarization stability in our system and to Faraday rotation from our fiber is to use PM single mode fiber. We use PM780-HP fiber from Thorlabs which is a Panda style fiber and has a fiber cross section shown in figure 3.3A. The two Panda stress rods are composed of B_2O_3 doped silica while the core is GeO_2 doped silica. While the fiber is cooled after synthesis, the difference in thermal expansion coefficients between the doped glasses induces large stress into the final fiber. The geometry of these rods exerts an anisotropic stress on the core of the fiber to create two orthogonal propagation modes with different indexes of refraction. This anisotropic index of refraction leads to a controlled fiber birefringence with a fast and slow axis as shown in figure 3.3A[48]. Light coupled with a linear polarization along either mode will stay polarized in the fiber independent of external stresses and fields. For light coupled into the fiber with its polarization perfectly aligned along either the fast or slow axis, the ER of the fiber describes the SOP at the exit of the fiber, where the ER gives the coupling or cross-talk between the two modes and thus limits measurement [49]. For light that is coupled with a misalignment between the polarization of the light and either axis of the fiber, the fiber acts as a very high

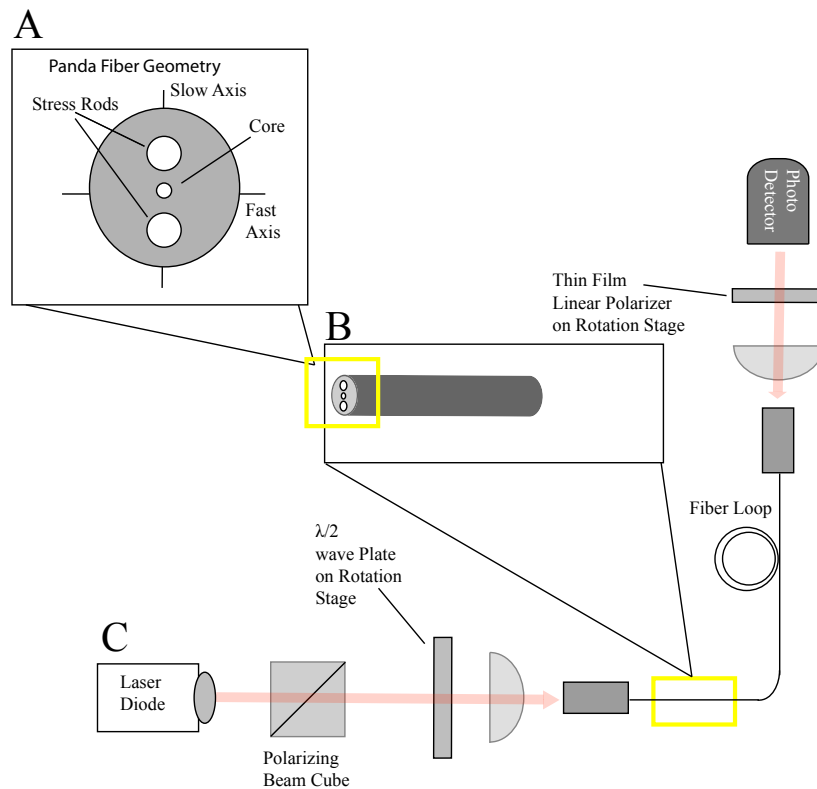


Figure 3.3: Polarization Maintaining Fiber Launch and Panda Fiber Geometry. (A) Diagram of the geometry of a Panda type PM fiber. (B) Expanded view of PM fiber in our coupling arrangement. The geometry of the stress rods is fixed. (C) Here we illustrate our setup for optimizing our coupling of polarized light into our PM fiber. The $\lambda/2$ wave plate and the thin film polarizer are on rotation stages allowing us to align them rotationally to the fiber axis.

order wave plate with a final SOP set by the phase difference between the two fiber axes and the path length.

The alignment dependence of the SOP at the exit of the fiber means we need some way to optimize the alignment of our launch polarization with respect to the fiber axes, which are fixed in our coupling geometry. While we have a maximum ER for a perfect alignment of launch polarization and fiber, we also have an effective ER given by the ratio of power measured in the intended launch axis to the power measured in the cross-talk axis. As shown in figure 3.3C, we couple the exit of the fiber to a fiber mounted collimator and set up a thin film polarizer on a rotation stage. We position a photodetector to measure the transmitted power, and start by aligning the polarizer by eye to the fiber key on the fiber termination, which denotes the slow axis of the fiber. We do a first order alignment by aligning the launch wave plate to maximize the transmitted power at the detector, and then iteratively adjust the launch wave plate and polarizer to maximize the transmitted power. Due to coherence effects in the fiber, this only gets us to an alignment on the order of a few degrees. We can turn the laser diode drive power below the lasing threshold which will give us an effectively incoherent source, but this still only gets us to about a degree of accuracy which can reduce our effective ER by a factor of 10 [50]. In order to get better alignment, we can use coherence to our benefit.

In this optical arrangement, we can model the transmitted power (P) as

$$P \propto (\sin\theta_i \sin\theta_0)^2 + (\cos\theta_i \cos\theta_0)^2 + \frac{1}{2} \sin 2\theta_i \sin 2\theta_0 \cos \Delta\phi \quad (3.1)$$

where θ_i is the angle between the launch polarization and the principle launch axis, θ_0 is the angle between the principle fiber axis and the detection polarizer, and $\Delta\phi$ describes the birefringence of the fiber [50]. For a PM fiber, $\Delta\phi = 2\pi f L \Delta n c$

where f is the frequency of the light, L is the length of fiber, c is the free space speed of light, and Δn is the difference in index of refraction for the orthogonal axes of the fiber. From this, we can see that if we set our detection polarizer at a 45° angle from the principle fiber axis, we will be maximally sensitive to changes in P with changes in $\Delta\phi$. We also see that changes in P from $\Delta\phi$ will be minimized when the launch polarization is aligned to the principle fiber axis. If we can tune $\Delta\phi$, which we can do by either changing Δn or by changing the frequency of the excitation, we can optimize the launch waveplate by adjusting it to minimize for the change in P . Other groups have made this work by modulating the laser frequency by either modulating the drive current for their laser diode or by modulating the laser cavity for a cavity locked laser diode system [50]. We can also tune Δn easily by changing the temperature of the fiber, as the thermal expansion difference changes the fiber core stress state [49]. We find that for a fiber loop shown in figure 3.3C of approximately 2 meters we can easily generate three to four full cycles in power using just the heat from our hands with the optical table as a heat sink. If we have a shorter length of fiber we can use a heat gun to get the same effect. With this method we can achieve alignments of better than 0.3° where we are limited by the precision of our rotation stage. With an alignment of better than 0.5° we are limited by the intrinsic ER of the fiber due to defects and axis cross-talk [50]]. This alignment method has the added benefit of allowing us to determine the ER of the fiber. We define a term E so $E \equiv \frac{(\langle P_{\max} \rangle - \langle P_{\min} \rangle)}{(\langle P_{\max} \rangle + \langle P_{\min} \rangle)}$ where $\langle P_{\max} \rangle$ is the maximum measured power and $\langle P_{\min} \rangle$ is the minimum measured power both averaged over the observed cycles. The ER of our fiber is given by $ER = (\frac{1}{2}E)^2$, as explained in Caponia et al. [49].

3.4 Polarization Maintaining Fiber Based Measurements

After switching to PM fiber, we cooled down our sample with the same mounting geometry and on-sample thermometry. We align the fiber key, denoting the fiber slow axis, at a 45^0 angle from the sample tilt axis to maximize the polarization rotation if the potential birefringence of the sample reflects the broken symmetry from transport measurements. We used a standard transport setup with two Stanford SR830 lock-in amplifiers where we sourced an oscillating 1 V signal from one lock in, then used a $100\text{ k}\Omega$ source resistor to set the current flow in our measurement lines at $10\text{ }\mu\text{A}$. The measurement lines for the fridge are $130\text{ }\Omega$ and the contact resistance for our epoxy joints is on the order of 10 to $50\text{ }\Omega$ so these series resistances should be negligible, but we also measured the voltage drop across the source resistor with the second SR830 to confirm our current. We then measured the voltage drop across the sample using the A-B input channel for the lock-in and recorded the in-phase and out-of-phase components using the analog outputs from the lock-in and our DAQ. We initially cooled down to 1.3 K (which is above the expected transition temperature for the nematic phase at this sample quality and mounting angle [15]) with the mash condensed to strongly thermally link the mixing chamber to the 1 K pot of the dilution refrigerator. Unfortunately as we cool below 10 K (measured at our 1 K pot), our sample resistance decreases below the measurement limit for our lock-in. The Stanford Sr830 has a common mode rejection ratio (CMRR) of 100 dB or 1 in 10^5 , which means that with our $130\text{ }\Omega$ measurement lines we can measure signals as low as $1.3\text{ m}\Omega$ in our four point geometry. Reducing the line resistance is infeasible for thermalization reasons. Our only way to fix this is to find a better system with a higher common mode rejection or to increase our sig-

nal by changing the sample shape. We also tried to use our AVS-47b resistance bridge to measure the sample resistance, but ran into similar issues where the signal was saturated at 1.3 K. We may have seen some magnetoresistance at 9 T with the resistance bridge, but it was well within the noise in the measurement. We need to cut or shape the sample, but we were reluctant to try that without an optical signal as we only had access to the one crystal.

At 1.3 K we recorded the transport signal and polarization signal during field sweeps from 0 T to 8.9 T, as well as the constant field time dependence of the polarization. We start each field sweep by aligning our detection wave plates to maximize the transmitted signal of our polarizing beam cube in the detection path. We define a parameter called polarization angle as $\theta = \tan^{-1}(\sqrt{\frac{P_a}{P_b}})$ where P_a and P_b are the powers measured by the detectors in the transmitted and reflected channels respectively. Figure 3.4 illustrates a typical signal for a field sweep from 0 T to 8.9 T with a sweep rate of $0.1 \frac{T}{\text{min}}$. We define a second parameter, the change in polarization angle, for easy comparison of different sweeps as $\Delta\theta$, which is θ subtracted from θ_i (the initial value of θ at the beginning of a field sweep or time course). We see large polarization changes over the course of a roughly 1.5 hour sweep, including a switching of the apparent fiber axis with the maximum power. When we look at the time dependence of the polarization at constant field, figure 3.5 illustrates that we still have significant instabilities in our polarization signal with time. These instabilities seem to have some unexplained field dependence, and in particular there seems to be an optimal field range where we have a minimum of polarization fluctuations in time between 3 T and 6 T. The fluctuations are also reduced above 6 T with respect to the zero field polarization signal. These fluctuations look very similar to the time dependent fluctuations that we have with fiber phase shifts when

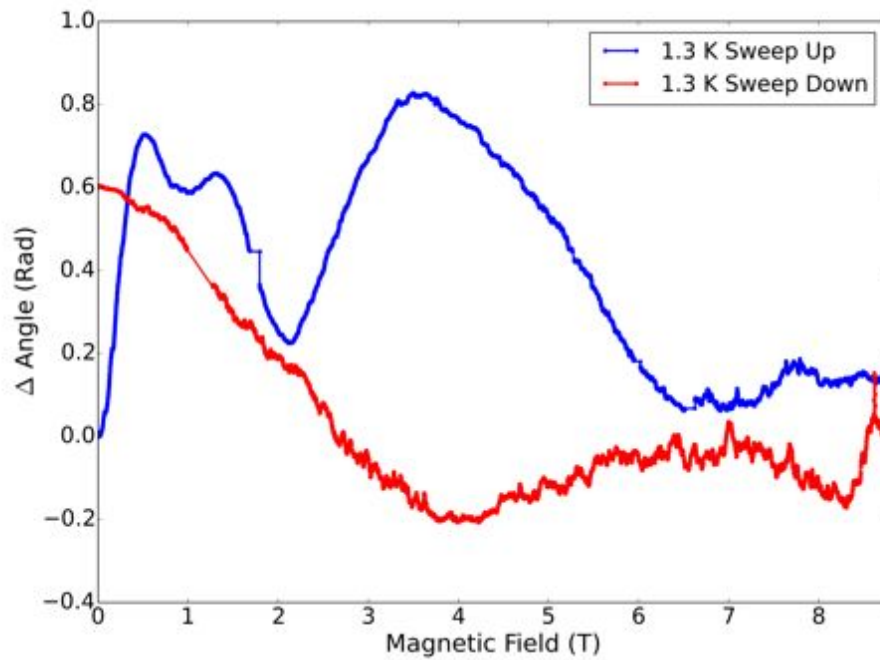


Figure 3.4: Polarization Response at 1.3 K. Here we plot the change in polarization angle (as defined in the text) with sweeping magnetic field at 1.3 K. We swept continuously at 0.1 T/min while monitoring the weights continuously in our two detectors. This illustrates the large degree of instability in our fiber system.

we are heating our fiber, which suggests that we have some issue with ER or coupling losses in our fiber that are not explained completely by the previous description of our fiber system. As discussed in section 3.1, we are looking for a sudden change in the polarization with field to attribute to the nematic phase transition so we look for abrupt changes in the polarization state as we sweep field on top of the slowly drifting background.

We cooled down to a stable sample base temperature of 250 mK to 170 mK (dependent on heat applied to still) using the dilution refrigerator and repeated field sweeps between 7 T and 8.9 T to look for a nematic signature in the polarization response. From our time dependent measurements we do often see a stable polarization signal for tens of minutes at a time, which allows us to perform one to two tesla field sweeps depending on our sweep rate. We keep our sweep rate below $0.1 \frac{T}{\text{min}}$ to prevent eddy current heating at our sample. Despite our slow sweep rate and small sweep ranges, we see a range of behaviors as we sweep the field while monitoring the polarization signal with little consistency from sweep to sweep. Typical scans are shown in figure 3.6, where we see a smooth changing polarization background with small time scale or field step variations along the entire length of the sweep. We see nothing to indicate a definitive signature from a nematic phase transition for any of our sweeps, but we do have one sweep where we had a minimum in background polarization drift which did show two polarization jumps at magnetic field values that match the measured phase transition points for a 5° sample tilt as measured by dilatometry [15]. This data set is shown in figure 3.7. These features are suggestive but in no way conclusive. We could not replicate the relatively low polarization drift rate of this scan to confirm this. If we average over multiple sweeps to look for trends consistent across multiple sweeps, we cannot identify

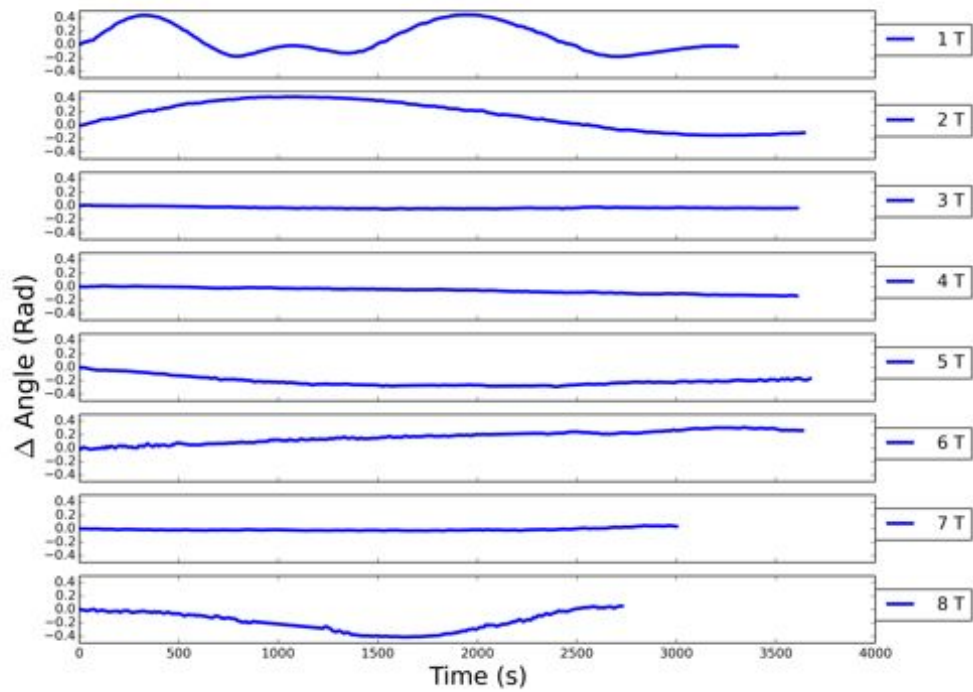


Figure 3.5: Magnetic Field Dependence of the Polarization Response with Time. Magnetic Field Dependence of the Polarization Response with Time Here we plot the constant field, time dependent polarization angle change with applied magnetic fields from 1 T to 8 T in steps of 1 T. Note that the system seems most stable above 3 T, though significant shifts occur again above 7 T.

any relevant features.

While making these measurements we also noticed that the sum of P_a and P_b was not constant during scans, suggesting that we potentially had either a change in sample reflectivity with field or a change in microscope coupling with field or time. Our previous measurements of the microscope performance in field showed no indication of issues of coupling with field or time. To examine this further, we removed the polarizing cube from the detection setup and measured the power at our detector with no polarization sensitivity while also monitoring the laser power. We see that our laser power is constant to better than 5 parts in 10^4 over the entire lengths of our scans which confirms that our measured power fluctuations are coming from our fiber or our sample. We see a 5% fluctuation amplitude over the course of a full sweep from 0 T to 8.9 T with no obvious repeated features in field. We also see no notable and repeatable distinction between light launched on the fast or slow axis of the fiber.

We determined that the limiting factor in these measurements was the ER of the PM fiber. While we have specification limited ER at the end of our first fiber, as measured by our fiber polarization alignment technique referenced in section (C), each coupling joint in our fiber system has a non-zero misalignment and each of these misalignments reduces our ER. As explained in Penninckx et al., each of these misalignments contributes to an effective reduction in measured ratio of the power in the orthogonal fiber modes [43]. Using our fiber based beam cube to separate out the reflected signal from the sample, we have 7 different connections between the initial launched fiber and the final free space detection. Each of these connections is made by a mechanical coupler specifically designed for PM fiber connections where there is a keyway in the connector that

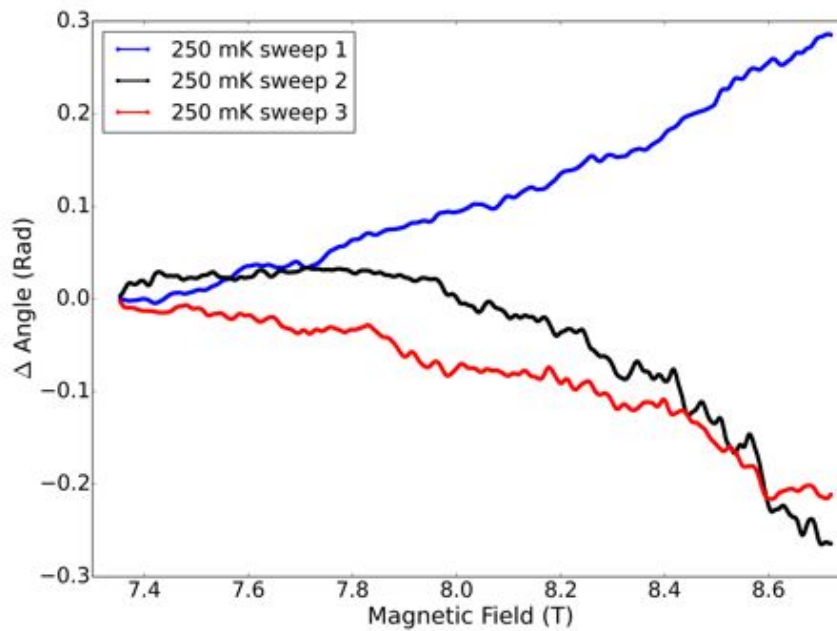


Figure 3.6: Typical Polarization Sweeps at Dilution Temperatures. Here we plot the polarization angle change for three different magnetic field sweeps take on the same day. Each of these sweeps was taken at 0.05 T/min and each of these sweeps started at 7.5 T and ended at 8.9 T, measured at the magnet power supply. The field data has been scaled to account for the distance between the sample and the dewar field center. The magnitude of polarization drift and oscillation in these three sweeps is typical independent of sweep direction.

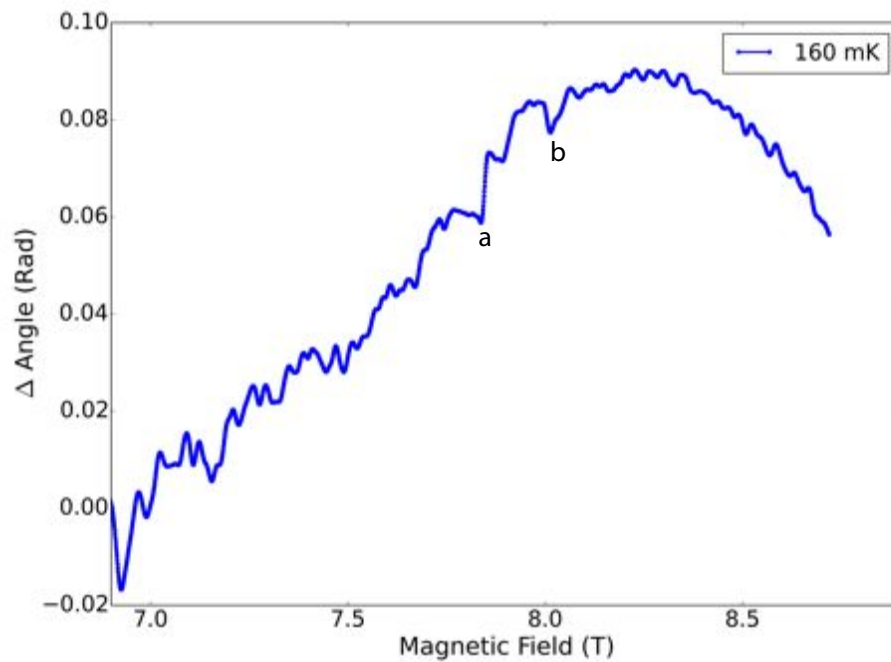


Figure 3.7: Lowest Drift Polarization Angle vs. Magnetic Field Sweep. Here we plot the polarization angle change vs. applied magnetic field at 160 mK with a sweep rate of 0.05 T/min. The field values have been scaled to reflect the difference between the sample position and the dewar field center. We see large and sudden jumps in polarization angle on top of the long time scale drift at 7.85 T (a) and 8.01 T (b), though there are other large short time scale fluctuations at other field values as well.

mates to the fiber polarization axis key to hold the fibers in rotational registry. When we measure the ER of our system after each junction, we see large reductions after each joint. While we start with a launch ER of ≈ 17 dB (limited by the noise in our detector) and by the time our light enters our polarization analysis setup we measure an ER below 5 dB. Further complicating this system is that each time we remake a joint, the ER loss changes depending on the alignment of the fiber axes within the connector keyways. This potentially explains the large time dependent polarization shifts in our measurements and possibly explains the field dependence of the time dependence. Once we have such a poor ER, our entire fiber system is just acting as a giant uncontrolled time dependent, high-order wave plate. We reduce the number of necessary fiber junctions by switching to the free space 90/10 beam cube describe in section 3.1 which brings us down to 2 fiber joints between the launch and detection. These two fiber joints are still enough to reduce our ER from 17 dB to 8 dB at our detectors, though this is complicated by the fact that we seem to be seeing a larger reduction in ER after the light reflects from sample. We still have an ER of 14 dB at our sample, and all the remaining reduction happens on the path from the sample to the detector. Based on Mirri et al. it seem unlikely that there is some differential reflectivity for the orthogonal polarization modes from the fiber at this small angle of sample tilt, but we seem to be losing ER somewhere[44]. There is the possibility that we have a directional dependence in the fiber joints due to the location of possible fiber defects, though it is hard to quantify how much of a difference we could see from that [51]. It is possible, in principle, for us to use a single fiber with no junctions between the launch and sample. For future work, this should be changed to eliminate fiber joints as a source of polarization cross talk.

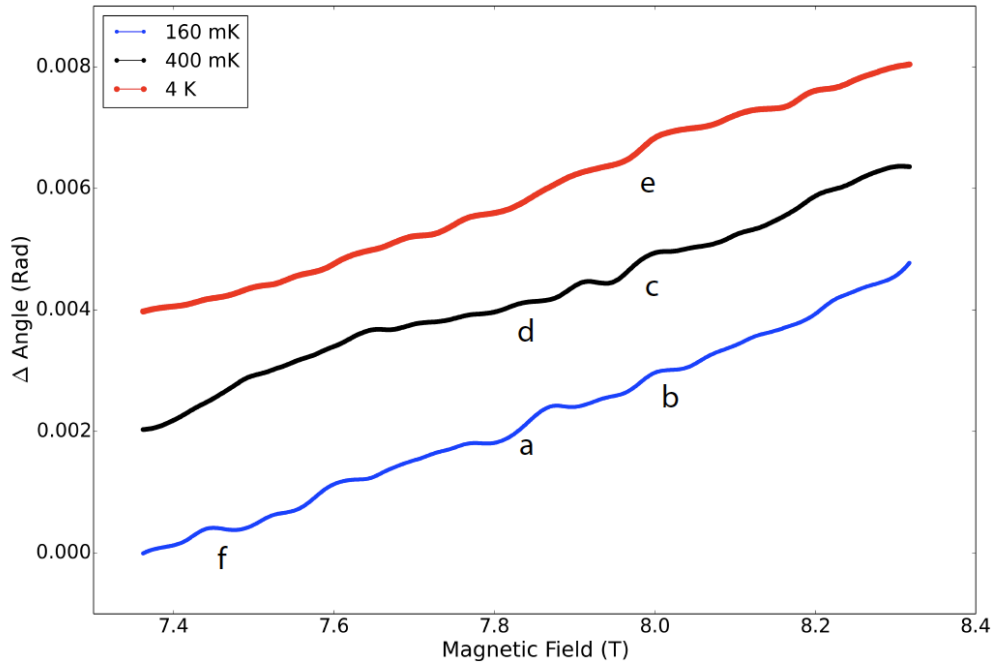


Figure 3.8: Polarization Angle vs. Magnetic Field with Incoherent Excitation. Here we plot the polarization angle change vs. applied magnetic field at 160 mK, 400 mK, and 4 K. For each temperature, we have averaged our signal over 6 distinct sweeps taken on the same day: 3 sweeps increasing field and 3 sweeps decreasing field. Each of these sweeps was taken with a 0.05 T/min sweep rate. We attribute the constant linear signal to Faraday rotation from our focusing optics. (a) and (d) point out features at 7.85 T. (b), (c), and (e) point out features at 8.01 T. (f) points out a feature at 7.45 (T)

While we could repeat our measurements using coherent light and our improved ER, we instead chose to switch to incoherent light as a source. The polarization oscillations we measure are due to a coherent interference effect as the optical power in the two birefringent modes recombines at the exit to the fiber to create a new polarization state. The changing indices of refraction in the fiber cause a changing phase difference between the two modes and alter that state independent of sample effects. If we instead switch to light with a coherence length significantly shorter than our fiber path we can eliminate the coherent recombination effects. We are less sensitive to polarization rotations with incoherent light, but it simplifies the analysis. In this case we are measuring the amount of power in each fiber axis and looking for a change in weight from one axis to the other with changing field. As mentioned in section 3.3 where we discuss the polarization alignment, we can switch to incoherent light by driving our laser diode with a sub-lasing threshold drive current. We still align our launch polarization to our fiber axes using coherent light, but we then turn down the drive power. We measure our light source with a fiber coupled optical spectrometer and determine that we have a coherence length on the order $100 \mu\text{m}$ which is significantly shorter than our effective 10 meter fiber path. We remove our $\frac{\lambda}{4}$ detection wave plate and rotate our $\frac{\lambda}{2}$ detection wave plate so we have equal powers in our reflected and transmitted detection paths.

We repeat field sweeps and constant field time-dependent measurements between 7.5 T and 8.5 T using our incoherent excitation. Figure 3.8 shows $\Delta\theta$ at three different temperatures where we have averaged 6 different sweeps (3 sweeps from 7.5 T to 8.5 T and 3 sweeps from 8.5 T to 7.5 T). The data at 400 mK and 4 K are manually offset from the 160 mK data by 0.002 mRad and 0.004 mRad respectively for clarity. We clearly see a polarization change that is linear

with applied field at all temperatures, which suggests we are seeing the background from the Faraday effect in our optics. We see a rotation of $4 \frac{\text{mRad}}{T}$, which is consistent with the Verdet coefficients given in [47] if we assume that our focusing lens sitting near the field center is the main culprit of Faraday rotation in our signal. We see a small increase of Verdet coefficient with decreasing temperature, which is consistent with the expected behavior of glass at low temperatures if there is a very small paramagnetic term as defined in equation 4 of Borrelli [52]. The constant field time dependence of our system shows no polarization drift over 40 minutes and a consistent noise floor of 0.8 mRad. From figure 3.8 we also see that there are some non-linear magnetic field features that persist after averaging over all of our scans at a given temperature. Similar to our sweep shown in figure 3.7, at 160 mK we see a bump at 7.85 T ((a) in figure 3.8) and 8.01 T ((b) in figure 3.8) but we also see similar features at other less suggestive field values and we don't see a comparable bump at 7.8 T ((d) in figure 3.8) for our 400 mK sweeps which we would expect if we were seeing a signal from the nematic phase transition. We also note that the feature at 8.01 T in the 400 mK ((d) in figure 3.8) and 160 mK ((b) in figure 3.8) sweeps also shows up in the 4 K sweep (((e) in figure 3.8), which should be well out of range of the nematic phase. It should also be mentioned that the magnitude of these features is well within the range of polarization fluctuations that we see with time at constant field. While it would be surprising to see time dependent features after averaging over multiple sweeps, it is a possibility we have not completely ruled out.

3.5 Discussion of Results

At this point, we have no conclusive evidence that we are seeing an optical signature in either polarization or reflectivity of the nematic phase transition. Our sample geometry prevented us from resolving the resistance changes expected for the nematic phase, so we have no control to tell us exactly where the phase transformation is occurring in field and temperature for our sample either. We have seen suggestive polarization changes while sweeping field using both a coherent excitation and an incoherent excitation, though the magnitude of response is significantly reduced for the incoherent excitation. If these polarization changes are from a phase transition or a magnetization jump, it is plausible that the coherent measurement would show a much larger signal that is also less repeatable. The same principle that leads to large fluctuations in signal when we are launching into the fiber for small misalignments of wave plate and fiber could serve to amplify a small sample birefringence after it travels through the fiber. This amplification would also be time dependent and likely to shift with applied field, even reversing in sign. While this could explain why we see no signal after averaging over multiple sweeps, its also possible that the position of the polarization jumps is entirely coincidental. We also see many other polarization fluctuations at non-suggestive fields when using coherent excitation.

In the incoherent excitation case, it is more definite that we have some changing polarization with field. We measure a clear linear rotation, which we attribute to a Faraday rotation from the focusing lens, as well as non-linear polarization fluctuations that repeat at the same field values for a given temperature. The fluctuations in the 400 mK and 160 mK data around 7.85 T, 8.01 T and 7.45 T ((f) in figure 3.8) could be attributable to the metamagnetic transitions

seen in de Haas - van Alphen, thermodynamic, magnetostriction, and magnetic susceptibility measurements [16][11][53], though the origin of the polarization change is not clear. If we are seeing a magnetic response from the sample, we would have expected our polarization angle to be sensitive to the sample magnetization which should give a monotonically changing polarization angle with applied field through Kerr rotation, with possible slope changes upon crossing the relevant field points. Here, we have an oscillation or asymmetric peak in polarization angle as we pass through the metamagnetic crossover and the two metamagnetic phase transitions. It is much more difficult to explain the field features at 4 K, as the thermodynamic signatures go away above 1 K [53] and it seems that while the magnetization is non-linear, it still monotonically increases with field [12]. The existence of the polarization fluctuations at 4 K and the lack of a consistent feature shape make it difficult to attribute the non-linearities in the lower temperature sweeps to the previously reported metamagnetic signatures, though we have most certainly not ruled them out.

Going forward there are two experimental changes that could serve to settle this issue. The most obvious change is to alter the sample geometry to enhance the resistance of the sample. With concurrent transport we would have a control to confirm the nematic transition phase diagram during our optical measurements. We tried switching to a novel transport measurement setup designed for low temperature measurements of low resistance samples. Our Keithley delta mode system, which has a CMRR of 200 dB, should allow us to make 1% error measurements down to $1 \mu\Omega$ with a 100Ω line resistance [54]. During cool down with the Keithley we had a sample holder lead break, which prevented us from testing this out. Given the stated specs for the Keithley system and a possible sample geometry change, we were optimistic that future measurements will

capture the magnetoresistance without issue.

We also should immediately switch to a fiber arrangement with no mechanical fiber junctions, which will give us a maximum fiber ER and eliminate much of the uncertainty and fluctuations when using coherent excitation. Once we eliminate the fiber junction limitations, we open up the possibility to use the coherent interference effects to enhance our signal. If we use a grating locked diode we could generate a time dependent laser wavelength, allowing us to use the same principles that allow us to accurately couple light into the fiber to analyze the recoupling of light back into the fiber after interacting with the sample. Detecting the change in fiber mode coupling would give us a measure of the light rotation after sample interaction. This measurement could be complicated by magnetic field effects in the fiber, and those would need to be accurately measured. There are other optical techniques that might offer insight into the nematic phase, such as interferometric detection of the Kerr rotation through Sagnac interferometry. Sagnac interferometry is sensitive to only the time reversal broken part of a polarization change, so this would not show a signal if there were a birefringence due to differential scattering times in the nematic phase [55]. Alexander Fried et al. have recently reported a fiber based scanning Sagnac microscope that functions at 820 nm, though they do not give results in a magnetic field or at cryogenic temperatures [8]. In that paper, they also suggest a means to adapt the detection scheme using a Faraday rotator instead of a $\frac{\lambda}{4}$ wave plate to detect a linear birefringence instead of a Kerr rotation. It is unclear if these Sagnac interferometer based techniques would work with the necessary large applied magnetic fields. In principle we could apply these techniques in our system, though the infrastructure needed would require significant purchases.

3.6 Conclusions

We have built a polarization sensitive detection scheme for our cryogenic, high magnetic field confocal microscopy platform. We used this detection scheme to investigate the electron nematic phase of $\text{Sr}_3\text{Ru}_2\text{O}_7$, and saw inconclusive results. Weve characterized the magnetic field performance of our system using both coherent optical excitation and incoherent optical excitation, demonstrating that the optical fiber ER is the limiting factor for resolving polarization shifts from sample interaction in our system from systematic effects. We see no definite optical signature of the electron nematic phase, though we do see fluctuations in our polarization signal with incoherent excitation at field values that are suggestive of the metamagnetic magnetic phase transitions and crossovers reported in this material through other magnetic and thermodynamic measurement techniques. We also see polarization fluctuations at other magnetic field values and temperatures where no such transitions or crossovers are reported. Further work should incorporate upgrades of the fiber optic system to enhance fiber ER and should incorporate transport measurements using an altered sample shape.

CHAPTER 4
**MAGNETOLUMINESCENCE SPECTROSCOPY OF SEMICONDUCTORS
AT CRYOGENIC TEMPERATURES**

Magnetoluminescence (ML), the measurement of photoluminescence (PL) of samples in a magnetic field, is a technique broadly used to investigate the physics of defects, excitons, and low dimensionality in semiconductor materials [56]. Application of magnetic fields breaks time reversal symmetry and spin degeneracy, and causes shifts in the band structure, which can be measured through PL spectroscopy. Splitting of the bands with applied field gives a measure of the effective magnetic moment associated with the carriers from the measured bands. Large enough magnetic fields can also quantize the band structure through Landau quantization if the scattering time is long enough for multiple carrier cyclotron orbits. This Landau quantization leads to new transitions between energy states that can be probed optically through PL spectroscopy. ML has been used to investigate the fractional quantum hall effect in semiconductor quantum well structures, exciton effects in self assembled quantum dots structures, excitonic transitions in colloidal semiconducting quantum dots, and PL from defect or impurity states in bulk semiconductors[57, 58, 59] [60][3].

4.1 Photoluminescence in Our Microscopes

For PL spectroscopy in our optical system, we need a few basic elements starting with a narrow line width excitation source. We then need to couple our source into the bore of our magnet to interact it with our sample and we need collect the light emitted from our sample and couple it into a spectral analysis system for determination of the PL spectrum. Figure 4.1 illustrates our light

generation and coupling optics, as well as our spectrometer and imaging setup. Similar to our polarization sensitive microscopy, we use a laser diode to generate a coherent excitation but we add a laser cleanup filter from Semrock after our beam shaping. Optical selection rules for PL are dependent on light polarization, so we polarize our beam with a polarizing beam cube and couple our polarized light into our fiber in the same manner as for our polarization. We use a $\lambda/2$ wave plate to choose which fiber axis to couple into and we optimize this coupling as described in section 3.3. The emitted light from our sample is collected using the same low temperature optics that couple the excitation to the sample in a focused spot. To enable polarization-resolved spectroscopy, a zero-order quartz $\lambda/4$ plate is placed between the aspheric collimation and objective lenses, oriented at 45° to the fiber axes; this couples σ_+ and σ_- emission into orthogonal polarization modes of the fiber. In our system, we are in a Faraday geometry where the polarization of the light is directed in the sample plane, while the magnetic field is oriented normal to the sample.

The light comes back out to room temperature through the optical fiber, and then we separate it out using the same 90/10 beam splitting cube geometry that we describe in section 3.1. This light is then routed through a thin film polarizer on a rotation stage, which allows us to select the light from either fiber axis for analysis. The light passes to a series of mirrors, one of which is on a flip stage (element 7 in figure 4.1), to choose between two analysis paths. In the first path, we couple the light into a multimode fiber which is then coupled into an APD with an optional band pass filter. When the band pass filter is in line, we reject the excitation light that may be recoupled into the fiber from sample reflection and can image the PL intensity from our sample. If we remove the band pass filter, we can image our sample using the same scanning techniques described



- | | | |
|-------------------------------------|-----------------------------|-----------------------------|
| 1. Laser Diode | 5. 90/10 Beam Splitter Cube | 9. Multimode Fiber Coupling |
| 2. Laser Cleanup Filter | 6. Fiber Launch | 10. Grating Spectrometer |
| 3. Polarizing Beam Cube | 7. Flip Mirror | 11. CCD Camera |
| 4. $\lambda/2$ Wave Plate on Launch | 8. Thin Film Polarizer | |

Figure 4.1: Photoluminescence Optics. Labeled photo illustrating the optics used to couple a PL excitaiton signal into our cryostat and the optics used to analyze the emitted PL from our sample.

in section 2.3 and determine the location of our excitation spot with respect to sample features like gating electrodes, alignment marks, or other features. In our second detection path, we couple our light into a thermoelectrically cooled CCD spectrometer for spectral analysis.

It is critical to determine accurately the relationship between the excitation polarization and the magnetic field direction. For linearly polarized excitation, this is trivial but for circularly polarized excitation, this becomes more difficult. We define σ_{\pm} polarization as the circular polarization which carries $\pm\hbar$ angular momentum per photon along the field direction for $B > 0$. Equivalently, σ_{+} (σ_{-}) polarized light can be defined as the light with electric field vector rotating counter-clockwise (clockwise) in time around the positive B axis.

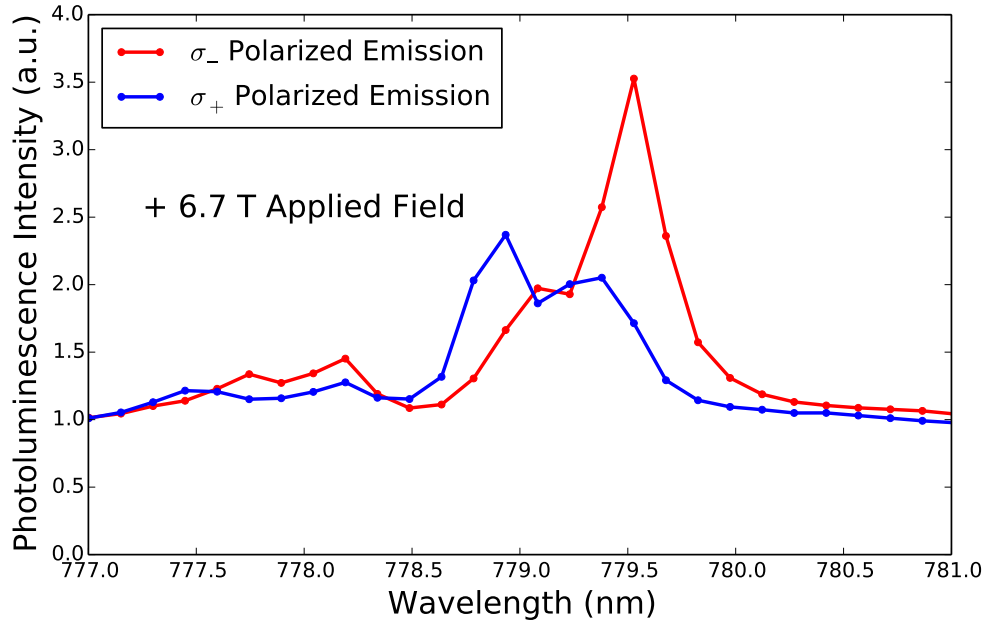
We determined the rotational settings of the detection polarizer corresponding to different circular polarizations of emission. To do this, we launched circularly-polarized laser light into the cryostat objective lens from the sample space, and found the settings of the detection polarizer which maximized the resulting signal. The circularly-polarized light was generated by sending linearly polarized light through a $\lambda/4$ plate with the light polarized at 45° to the wave plate axes. Given knowledge of the wave plate axes and their orientation relative to the light polarization, the handedness of circularly-polarized light produced in this fashion can be determined. We also checked the assignment of the wave plate fast and slow axes by shining circularly-polarized light of a known handedness through the wave plate and analyzing the resulting linear polarization. For this test, the circularly-polarized light was generated using two N-BK7 prisms in a Fresnel rhomb geometry, so that the resulting handedness could be determined from the Fresnel equations. We determined the field

direction using a calibrated Hall probe. The considerations above determine the rotational settings of the detection polarizer corresponding to detection of σ_+ and σ_- emission.

4.2 Magnetoluminescence of Bound Excitons in Bulk CdTe

As a test of our photoluminescence microscope in magnetic field, we measure the ML for a (110) cut, undoped, p -type CdTe substrate (from MTI Corporation). For p -type CdTe, the acceptor-bound exciton luminescence shows a four-fold splitting under magnetic field applied in the Faraday geometry. The optical selection rules lead to circular polarization of these peaks, so that two are σ_+ polarized and two are σ_- polarized. Our measurement of the ML of CdTe at 4.2 K is shown in figure 4.2 With the detection polarization determined as discussed above, we find peak splitting and selection rules for CdTe in agreement with those found by Refs. [57, 58, 59]. In particular, given that the lowest energy acceptor-bound exciton luminescence peak for CdTe is σ_- polarized (for $B > 0$). This illustrates that our determination of the light polarization and magnetic field geometry is accurate, and it also indicates that we do not have systematic errors from our optical elements. Due to the nature of our lens, we could have chromatic aberration that effectively makes our objective lens focal length and optical system recoupling efficiency dependent on the wavelength of the light. Shifts of our elements with magnetic field could appear to be shifts in the PL spectrum. Our CdTe let us rule out systematic spectral shifts with applied field.

A



B

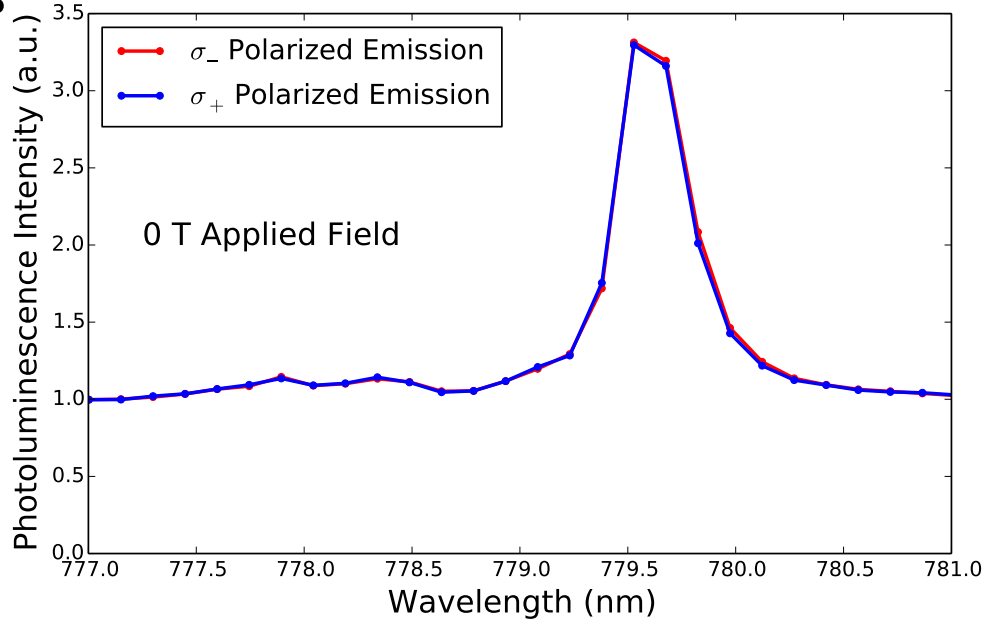


Figure 4.2: Photoluminescence Spectra of CdTe. Polarized PL spectra taken at 4.2 K with a 380 nW excitation source at 1.89 eV (656 nm). (A) PL spectra showing four-fold splitting (each circularly polarized signal is two-fold split) of the maximal intensity PL peak at 6.7 T (B) PL spectra showing no peak splitting with no applied magnetic field. The peak shape in both A and B is limited by the resolution of the CCD camera based spectrometer used to collect spectra.

4.3 Breaking of Valley Degeneracy by Magnetic Field in Monolayer MoSe₂

The following sections 4.3-4.10 are adapted from "Breaking of Valley Degeneracy by Magnetic Field in Monolayer MoSe₂" published in Physical Review Letters 114, 037401 Published 22 January 2015 with authors: David MacNeill, Colin Heikes, Kin Fai Mak, Zachary Anderson, Andor Kormnyos, Viktor Zlyomi, Jiwoong Park, and Daniel C. Ralph

Monolayer MoSe₂ and other monolayer transition metal dichalcogenides (TMDs) are a materials system with unique potential for controlling their valley degree of freedom [18, 19, 20, 21, 22, 23, 24, 25]. Similar to graphene, the conduction and valence band show extrema (valleys) at the vertices of a hexagonal Brillouin zone; unlike graphene, MoSe₂ exhibits a nonzero optical gap of 1.66 eV [26, 27]. This has allowed exploration of optoelectronic properties arising from the valley-dependent chirality of massive Dirac fermions, predicted in the context of inversion symmetry broken graphene [30, 31]. This chirality leads to optical selection rules coupling the exciton valley degree of freedom to photon handedness [19, 20, 21, 22, 23, 24]. Using polarization-resolved spectroscopy researchers have demonstrated valley-selective luminescence with near 100% fidelity [19, 24]. Furthermore, the ability to pump valley-polarized carriers with circularly-polarized light has been demonstrated through the valley Hall effect [25]. The chiral electronic states are also predicted to possess valley-contrasting orbital magnetic moments coupling valley pseudospin to magnetic field [30, 31, 32, 33, 34, 35, 36], which opens up the possibility for magnetic control over the valley degree of freedom [37, 32].

Here, we demonstrate the use of magnetic fields to break valley degeneracy in a monolayer TMD. Specifically, we report polarization-resolved luminescence spectra for back-gated MoSe₂ devices at 4.2 K and in magnetic fields up to 6.7 T. We study the luminescence peak energies as a function of magnetic field, finding a linear splitting of $-0.22 \frac{\text{meV}}{\text{T}}$ between peaks corresponding to light emission with different senses of circular polarization, σ_+ and σ_- . We interpret this as a Zeeman splitting due to valley-dependent magnetic moments. We also investigate the magnetic field dependence of luminescence handedness, finding that the emission becomes circularly-polarized in magnetic field even with unpolarized excitation, and that the degree of this polarization can be increased to about 50% by gating the sample. This suggests that electric fields can facilitate the generation of valley-population imbalance in samples where valley degeneracy has been broken by magnetic field. Our results demonstrate a recently-proposed [37] strategy for generating valley populations, and could lead to new approaches for controlling the valley degree of freedom in monolayer TMDs.

Our device geometry and measurement apparatus are shown in Fig. 4.3a and 4.3b. All measurements were taken using a scanning confocal microscope integrated with a 7 T superconducting magnet dewar, with light coupled in and out of the system via a polarization-maintaining optical fiber (similar designs were reported in Refs. [7, 6]). The light is focused into a roughly 1 μm diameter spot using a pair of aspheric lenses, and the sample is scanned using piezo-driven nanopositioners (from attocube). The sample, positioners, and optical components are placed in a vacuum cryostat which is then evacuated and lowered into a helium bath containing a superconducting magnet; helium exchange gas is added to ensure thermalization of the sample at 4.2 K. For the data in the main text, the excitation power was between 10-60 μW .

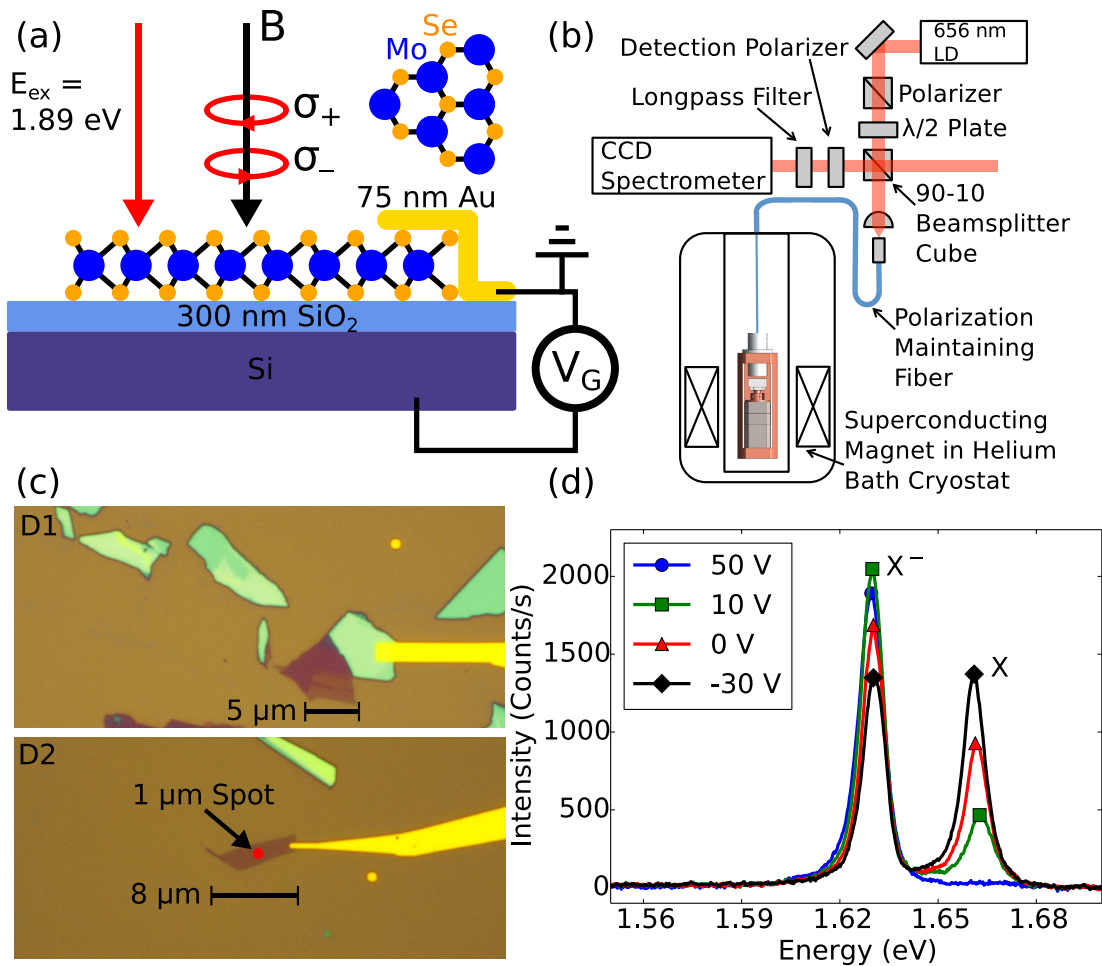


Figure 4.3: (a) Experimental geometry showing back-gated monolayer MoSe_2 devices in out-of-plane magnetic fields. Luminescence is excited with light from a 1.89 eV laser diode and collected separately for σ_+ and σ_- polarization in the Faraday geometry. (b) Schematic of the fiber-coupled optical cryostat used in the experiment. (c) Optical micrographs of devices D1 and D2. (d) Luminescence spectra of D2 taken at 0 T and 4.2 K with -30 V, 0 V, 10 V, and 50 V back-gate voltage.

To enable polarization-resolved spectroscopy, a zero-order quartz $\lambda/4$ plate is placed between the aspheric lenses, oriented at 45° to the fiber axes; this couples σ_+ and σ_- emission into orthogonal polarization modes of the fiber. The light exiting the fiber is directed through a rotatable polarizer, which selects one fiber mode for spectral analysis by a thermoelectrically cooled CCD spectrometer. We can also create circularly-polarized excitation by coupling linearly-polarized light into one of the two fiber polarization modes, or create equal intensity excitation in σ_+ and σ_- polarization by coupling in light polarized at 45° to the fiber axes. We excite photoluminescence with light from a 1.89 eV laser diode, which is 230 meV blueshifted from the A exciton transition, and as a result we see little dependence of the emission polarization on excitation polarization (see supplement section 1). The conclusions discussed below are independent of excitation polarization.

To fabricate our samples, we exfoliate bulk MoSe₂ crystals (grown by direct vapor transport) onto 300 nm silicon oxide on silicon, then use electron-beam lithography to define a single 0.5 nm Ti/75 nm Au contact, allowing use of the silicon substrate as a back gate. All data shown in the main text were taken from devices D1 and D2 pictured in Fig. 4.3c. Figure 4.3d shows the $B = 0$ luminescence spectra of D2 at -30 V, 0 V, 10 V, and 50 V. The peaks at 1.66 eV and 1.63 eV correspond to the neutral and charged A exciton respectively, with a charged exciton (trion) binding energy of 30 meV [26]. As the back-gate voltage is increased the exciton luminescence decreases and the trion luminescence increases, showing that our samples are intrinsically n -type and that the 1.63 eV peak corresponds to negatively charged trion luminescence.

Figure 4.4a compares polarization-resolved spectra taken for D1 in out-of-

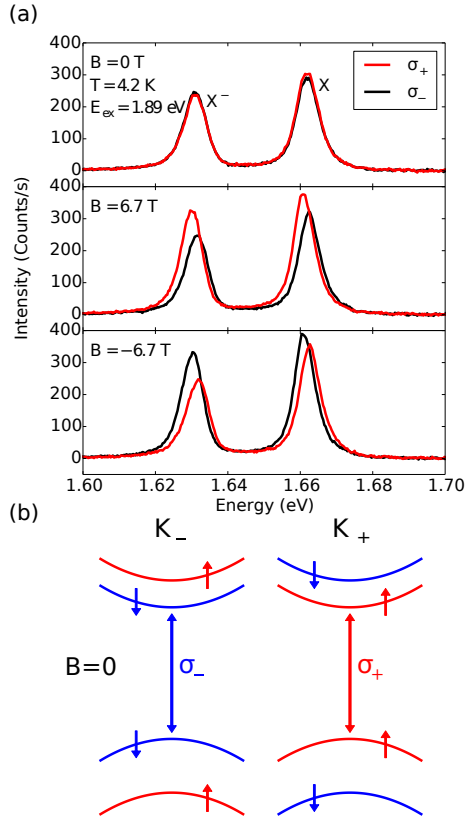


Figure 4.4: (a) Polarization-resolved luminescence spectra from monolayer MoSe₂ (D1) at 4.2 K for σ_+ and σ_- detection, as excited using unpolarized light at 1.89 eV. From top to bottom the panels show spectra taken with 0 T, 6.7 T and -6.7 T out-of-plane magnetic field. Both the polarization and splitting change sign upon reversing the field as shown in the lower panel. (b) Schematic band-structure of MoSe₂ near the K_+ and K_- points in zero magnetic field, showing the optical selection rules for the A exciton transition studied in this experiment. Within each valley, spin degeneracy is broken at $B = 0$ due to spin-orbit coupling, [27, 26, 32, 61, 62]. The arrows denote spin angular momentum up and down for the occupied states.

plane magnetic fields of 0 T, 6.7 T and -6.7 T and with the back gate grounded. For these data, we excite photoluminescence using equal intensity excitation in σ_+ and σ_- polarization. At zero field, we find no significant dependence of the peak energies or intensities on emission handedness. In comparison, the spectra taken at 6.7 T show splitting between the σ_+ and σ_- emission peaks of about -1.5 meV for both the exciton and trion. The luminescence is also σ_+ polarized: the trion peak has $P_{\text{trion}} = \frac{I_+ - I_-}{I_+ + I_-} = 14\%$, where I_{\pm} is the peak intensity of the trion in σ_{\pm} detection. For the exciton we measure $P_{\text{exciton}} = 9\%$. The luminescence polarization changes sign with reversal of the magnetic field but not with excitation polarization, showing that it arises from magnetically induced changes in the exciton and trion populations. Figure 4.4b depicts the schematic band structure of a MoSe₂ monolayer, illustrating the direct band gaps at the K_+ and K_- points, with arrows indicating the allowed A exciton transitions for σ_{\pm} light. Since the emission handedness is coupled to the exciton valley degree of freedom, the peak splitting and polarization we observe indicate valley degeneracy breaking.

Figure 4.5a shows the valley splitting of the exciton and trion peaks, defined as the difference between peak luminescence energy in σ_+ and σ_- detection, versus magnetic field. For each data point the peak positions were extracted via fits to a phenomenological asymmetric Voigt line shape (see supplement section 2). The errorbars come primarily from the CCD pixel size (about 0.15 nm per pixel). For both the exciton and trion peaks the valley splitting shows a linear magnetic-field dependence with a slope of $-0.22 \pm 0.01 \frac{\text{meV}}{\text{T}}$, and consistent results were found on three separate devices; data from other devices are given in supplement section 3.

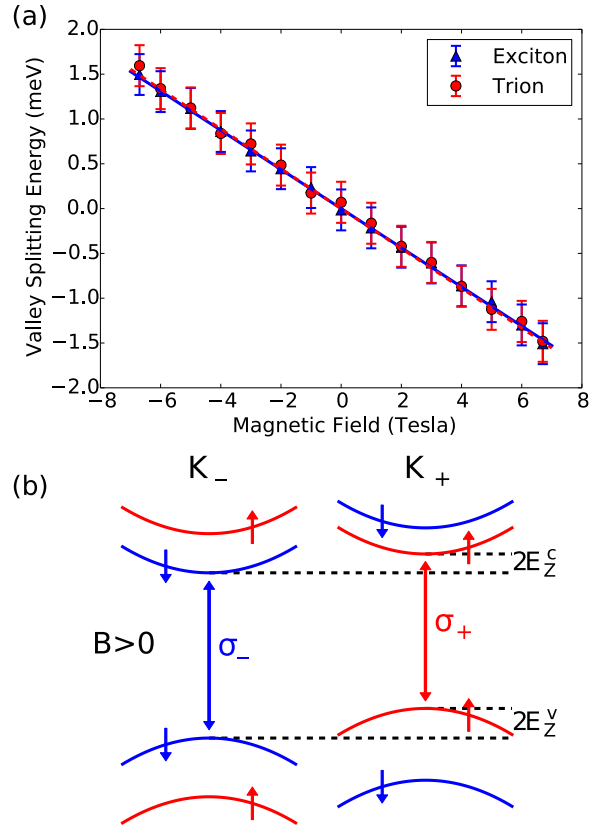


Figure 4.5: (a) Difference of peak energies found for σ_+ and σ_- detection plotted versus magnetic field for D1. Both the exciton (blue triangles) and trion (red circles) show splitting of $-0.22 \pm 0.01 \frac{\text{meV}}{\text{T}}$ found via a linear fit. The fits are plotted as blue solid and red dashed lines for the exciton and trion respectively. (b) The schematic bandstructure of MoSe₂ in magnetic field showing the Zeeman energy $E_Z^{c(v)}$ for the conduction (valence) band. The exciton Zeeman splitting is $2(E_Z^c - E_Z^v)$.

Valley splitting in magnetic field arises from the intrinsic chirality of Bloch electrons at the K_+ and K_- points. States at the two valley edges are Kramer's doublets related by time-reversal symmetry, so that their degeneracy can be broken by breaking time-reversal symmetry. Bloch electrons in a given band carry spin and orbital magnetic moments which change sign between valleys [31, 30, 63, 64]. Figure 4.5b schematically shows the energy shifts arising from Zeeman coupling between these moments and the magnetic field; there we define $2E_Z^{c(v)}$ as the magnetic-field-induced energy difference between the K_+ and K_- valley at the conduction (valence) band edge. Magnetoluminescence spectroscopy probes only the exciton Zeeman energy, which is the difference between conduction and valence band Zeeman energies. In this difference, the contributions from spin magnetic moments are expected to cancel, leaving only the contributions from orbital magnetic moments. The measured sign and magnitude of the valley splitting can be understood within a tight-binding picture [65, 66]. In the K_τ valley (letting $\tau = \pm 1$ be the valley quantum number), the valence band arises from hybridization of $d_{x^2-y^2} + \tau id_{xy}$ orbitals with angular momentum $l_z = 2\tau\hbar$ while the conduction band arises from hybridization of d_{z^2} orbitals with $l_z = 0$ [18, 23, 67, 62]. In the tight-binding limit, we therefore expect a contribution to the exciton Zeeman energy of $2(E_{Z,a}^c - E_{Z,a}^v) = -4\mu_B B$ from atomic-scale magnetic moments. The phase winding of Bloch states on the intercellular scale can also add to the orbital magnetic moment [65, 66, 30, 63, 68]. For example, in the two-band tight-binding model (the massive Dirac fermion model) the intercellular magnetic moment is equal for the conduction and valence bands with value $-\tau\mu_B \frac{m_e}{m_{\text{eff}}}$, where m_e is the free-electron mass, and m_{eff} is the electron-hole symmetric carrier effective mass [31, 30]. Including the bare spin magnetic moments this gives a total Zeeman splitting of $2E_Z^c = 2\mu_B + 2\mu_B \frac{m_e}{m_{\text{eff}}}$

for the conduction band and $2E_Z^v = 2\mu_B B + 4\mu_B B + 2\mu_B B \frac{m_e}{m_{\text{eff}}}$ for the valence band, and as a result $2(E_Z^c - E_Z^v) = -4\mu_B B$. In more general hopping models, the conduction and valence bands can have different intercellular moments giving a net contribution to the exciton magnetic moment [65, 66, 61, 35].

To compare our measurements with theory, we define the exciton valley g-factor $g_{\text{ex}}^{\text{vl}}$ as:

$$g_{\text{ex}}^{\text{vl}} = \frac{(E_+ - E_-)}{\mu_B B} = \frac{2(E_Z^c - E_Z^v)}{\mu_B B} \quad (4.1)$$

where E_{\pm} is the measured exciton peak energy in σ_{\pm} detection. Our exciton valley splitting measurements correspond to $g_{\text{ex}}^{\text{vl}} = -3.8 \pm 0.2$, consistent with the value of $g_{\text{ex}}^{\text{vl}} = -4$ expected from the d -orbital contribution to the exciton magnetic moment by itself. Any deviation of $g_{\text{ex}}^{\text{vl}}$ from -4 theoretically corresponds to the intercellular contribution to the g-factor. Our results are therefore consistent with the massive Dirac fermion model which predicts no intercellular contribution to $g_{\text{ex}}^{\text{vl}}$. We also expect the trion to have approximately the same splitting as the exciton, evinced by considering the trion as an exciton bound to an additional electron. While the additional electron contributes to the trion magnetic moment, it contributes equally to the final state moment after recombination leaving the transition energy unaffected (see supplement section 4). This is consistent with the experimental results of Fig. 4.5a for zero applied gate voltage.

We also attempted to calculate the valley g-factor using the multiband $\mathbf{k} \cdot \mathbf{p}$ theory of Refs. [64, 32], since their theory should include the intercellular and atomic contributions in a unified way [68]. The need to discuss these terms separately is an artifact of the lattice models discussed above. The calculation is detailed in section 5 of the supplement and gives a value for $g_{\text{ex}}^{\text{vl}}$ similar in mag-

nitude to our experimental results, but with the opposite sign (see supplement section 6 for our experimental determination of the sign). Therefore further theoretical work is required to understand the exciton valley splitting within the context of $\mathbf{k} \cdot \mathbf{p}$ theory calculations.

We find that the valley splitting and the resulting luminescence polarization both show a surprising dependence on an applied back-gate voltage. Polarization-resolved spectra taken with -20 V and 51 V applied to the substrate are shown in Fig. 4.6a for device D2. Our samples show significant hysteresis assumed to arise from photoionization of trap states [69], and the data in this panel are taken from a downward sweep. Figure 4.6b shows the trion splitting versus magnetic field for two different gate voltages on a downward sweep, finding $-0.29 \pm 0.02 \frac{\text{meV}}{\text{T}}$ at 40 V and $-0.23 \pm 0.02 \frac{\text{meV}}{\text{T}}$ at 0 V. This gate-voltage dependence of the valley splitting could arise from carrier-density dependence of the band Zeeman energies [35, 30], a hot luminescence effect as discussed in section 4 of the supplement, or other effects resulting from changes in the trion or final state wavefunctions upon increasing the Fermi level [70]. The gate dependence of trion valley splitting has implications for future magneto-optical studies of TMDs, as the intrinsic doping level may vary between samples causing a dispersion of measurement results.

The degree of trion polarization as a function of gate voltage is shown in Fig. 4.6c. In this dataset, we find a trion polarization that increases from 18% near zero back-gate voltage to over 50% near 40 V. The luminescence polarization is related to the valley population via $P_{\text{trion}} = \frac{n_+ - n_-}{n_+ + n_-}$, where n_{\pm} is the trion population in valley K_{\pm} . From this we infer that we are observing the generation of valley-polarized trion populations through applied magnetic field and

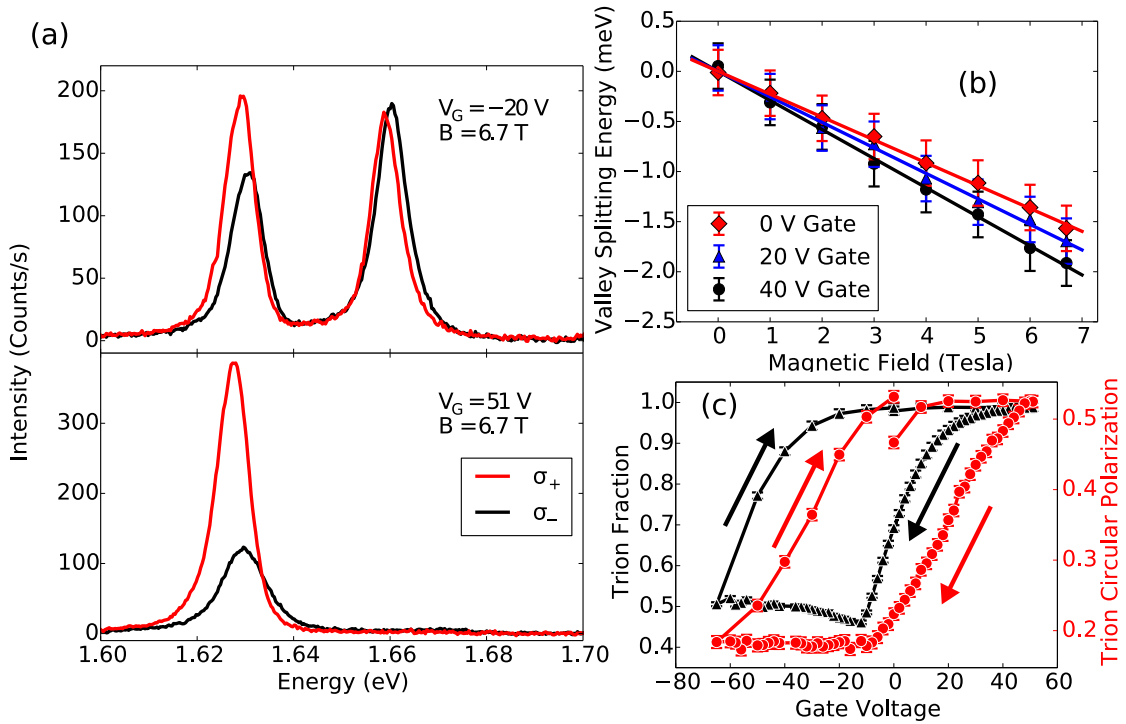


Figure 4.6: (a) Polarization-resolved luminescence spectra from D2 at 4.2K and 6.7 T for σ_+ and σ_- detection, excited with σ_- light at 1.89 eV. From top to bottom the panels show spectra taken with -20 V and 51 V gate voltage applied to the substrate. (b) Valley splitting versus magnetic field for selected gate voltages, showing an decrease in slope with gate voltage. (c) Circular polarization of the trion peak $\frac{I_+ - I_-}{I_+ + I_-}$ versus gate voltage at 6.7 T (red circles), showing an increase to over 50% as gate voltage is increased. For comparison, we also plot the trion fraction $\frac{I_{\text{trion}}}{I_{\text{trion}} + I_{\text{exciton}}}$ (black triangles).

gate voltage. The sign of P_{trion} in the n -type regime is independent of the excitation polarization but instead follows the sign of the magnetic field. We interpret the magnetic field dependence of the trion polarization as arising from partial relaxation of trions into their lowest energy spin-valley configuration (qualitatively consistent with the dependence of trion polarization on excitation power, see supplement section 7). This relaxation is expected to be incomplete as the intervalley scattering time is longer than the recombination time [70, 19]. In section 4 of the supplement, we calculate the trion polarization within a simple rate-equation model and show that the observed P_{trion} implies a ratio of the recombination time to the intervalley scattering time of ≈ 0.2 at low carrier density. This is about an order of magnitude larger than the value found in time-resolved measurements for WSe_2 at zero magnetic field [70]; however, the time-resolved measurements used resonant excitation which is expected to lead to reduced intervalley scattering compared to the off-resonant excitation we use. Trions can scatter between valleys via spin-flip intervalley scattering of their hole, and if this is the dominant scattering mechanism our results imply that the hole intervalley scattering rate increases monotonically with carrier density. This is consistent with the Bir-Aronov-Pikus mechanism for intervalley scattering of holes via their exchange interaction with the conduction electrons [19, 71]. The data in Fig. 4.6c was taken with σ_- excitation, but similar results were found using unpolarized excitation (see section 3 of the supplement).

In summary, we have presented measurements of polarization-resolved luminescence spectra for MoSe_2 at 4.2 K in magnetic fields up to 6.7 T, demonstrating valley degeneracy breaking. We measure a splitting of $-0.22 \pm 0.01 \frac{\text{meV}}{\text{T}}$ between exciton peaks in σ_+ and σ_- polarized emission spectra. This value is consistent with a simple tight-binding picture of the MoSe_2 bandstructure. We

also observe gate dependence of the valley splitting and polarization. Even with off-resonant, unpolarized excitation we were able to achieve a trion circular polarization of about 50% by gating the sample in 6.7 T magnetic field. Application of magnetic and electric fields can therefore provide an effective strategy for manipulating the valley degree of freedom in monolayer TMDs.

Similar work on WSe_2 has recently been posted by the Washington group [66] and the ETH Zurich group [65].

We thank Kathryn McGill and Joshua Kevek for growth of the bulk MoSe_2 crystal used for this work. We also thank Guido Burkard, Péter Rakyta, Alexander Högele and Ermin Malic for helpful discussions. This research was supported in part by the NSF (DMR- 1010768) and the Kavli Institute at Cornell for Nanoscale Science. We also made use of the Cornell Center for Materials Research Shared Facilities which are supported through the NSF MRSEC program (DMR-1120296). Device fabrication was performed at the Cornell NanoScale Facility, a member of the National Nanotechnology Infrastructure Network, which is supported by the National Science Foundation (Grant ECCS-0335765). D. M. acknowledges support from a NSERC PGS-D scholarship.

4.4 S1. Dependence of Luminescence Handedness on Excitation Handedness

Figures 4.7a and 4.7b show polarization-resolved luminescence spectra for D1 at $T = 4.2$ K and $B = 0$ T taken with σ_+ and σ_- polarized excitation respectively. We observe some preservation of the incident polarization even with our 1.89

eV excitation. We find $P_{\text{exciton}} = \frac{I_+ - I_-}{I_+ + I_-} = 6\%$ for σ_+ excitation and $P_{\text{exciton}} = -8\%$ for σ_- excitation indicating 7% average co-polarization of exciton luminescence with the excitation laser. On the other hand, we see counter polarization of 3% for the trion luminescence. We also studied the dependence of the field-induced polarization on excitation handedness: as shown in Fig. 4.7c switching the excitation polarization seemingly adds a constant offset. The small polarization preservation we observe is consistent with studies of polarization preservation in MoS₂ using off-resonant excitation [21, 19].

4.5 S2. Background Subtraction and Fitting

Raman scattering of the excitation laser in the fiber presents a significant background in our experiment, as has been reported elsewhere [7, 72]. A spectrum of fiber Raman excited with 705 nm light is plotted in Fig. 4.8a, showing fused silica Raman peaks [72]. Since we excite with 656 nm light we encounter only the tail of this signal during measurements of MoSe₂ luminescence. To account for this background, we take additional spectra with the excitation laser spot on silicon; the background spectrum is then subtracted from the signal after carrying out a dark-count subtraction on both spectra. This is shown in Figs. 4.8b and 4.8c. In practice, we rescale the background to match the signal spectrum away from the luminescence peaks, to account for laser-power fluctuations and to allow a single background spectrum to be used multiple times. In Figs. 4.8b and 4.8c we have used the data without rescaling to prove that fiber Raman entirely accounts for the background.

In the main text we report values for the peak polarization and energy as

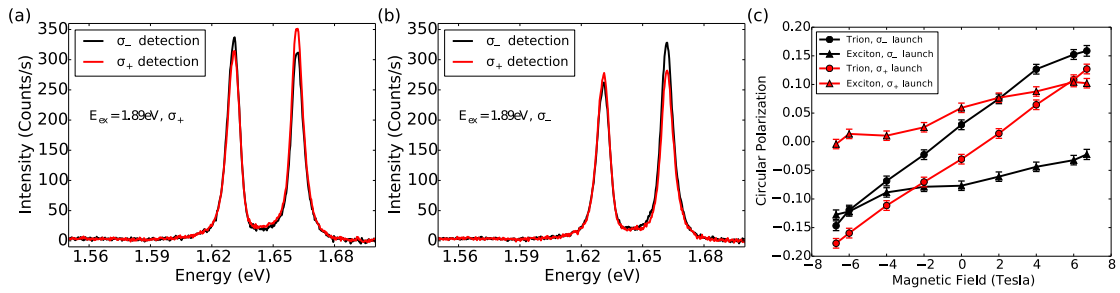


Figure 4.7: Luminescence Handedness Dependence on Excitation. (a) Polarization-resolved spectra from D1 taken at zero magnetic field and with σ_+ excitation, showing σ_+ polarization of exciton luminescence. (b) Polarization-resolved spectra from D1 taken at zero magnetic field and with σ_- excitation. (c) Luminescence polarization versus magnetic field with σ_+ (red) and σ_- (black) excitation for excitons (triangles) and trions (circles).

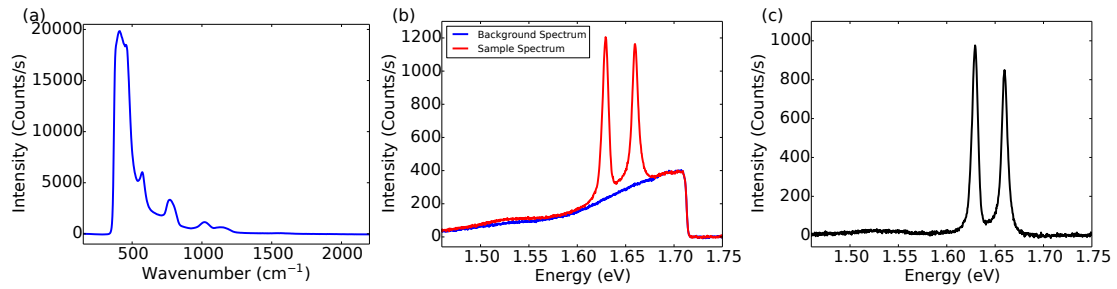


Figure 4.8: Fiber Background Spectra. (a) Fiber background spectrum excited with 705 nm laser diode, showing fused silica Raman peaks. (b) Comparison of spectra taken with 656 nm excitation laser on the sample (red) and on a nearby region of bare substrate (blue). (c) The result of subtracting the two curves in (b).

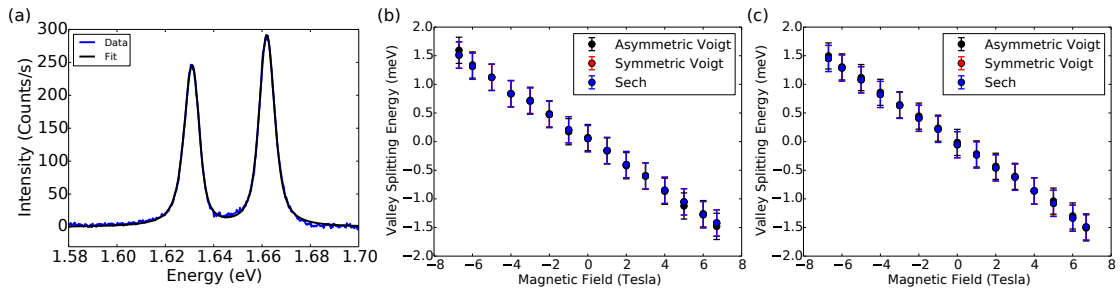


Figure 4.9: Peak Fitting Comparison. (a) Comparison of sample luminescence spectrum (blue) and fit used to locate peak energy (black). The spectrum is fit to the sum of two asymmetric Voigt profiles, with $\chi^2 \approx 3$ (b) Trion valley splitting as extracted with fits to asymmetric Voigt (black), symmetric Voigt (red), and hyperbolic secant (blue). (c) Exciton valley splitting as extracted with fits to asymmetric Voigt (black), symmetric Voigt (red), and hyperbolic secant (blue). Valley splittings from asymmetric Voigt fits are presented in Fig. 3 of the main text.

a function of magnetic field and gating. As described there, we use fits to an asymmetric Voigt profile to extract the peak properties. The Voigt function is defined as:

$$\frac{1}{\sigma\sqrt{2\pi}} \operatorname{Re} \left\{ \exp \left[- \left(\frac{\delta\omega + i\gamma}{\sqrt{2}\sigma} \right)^2 \right] \operatorname{erfc} \left[-i \left(\frac{\delta\omega + i\gamma}{\sqrt{2}\sigma} \right) \right] \right\}, \quad (4.2)$$

where $\delta\omega$ is the detuning and γ and σ are fit parameters characterizing the peak width. As written, the function describes the convolution of a Lorentzian with width γ and a Gaussian with width σ ; to make the line shape asymmetric we allow γ to take different values for positive and negative detuning. A typical spectrum with fit is plotted in Fig. 4.9a; in this case the χ^2 was about 3. We also tried fitting to other functions, such as a hyperbolic secant and a symmetric Voigt profile. There was no difference in the valley splitting within our error-bars. A comparison of splitting energies between symmetric Voigt, hyperbolic secant and asymmetric Voigt is shown in Figs. 4.9b and 4.9c.

4.6 S3. Comparison of Data from Multiple Devices

We measured the valley splitting versus magnetic field with the back-gate grounded for three different devices. All data were taken at 4.2 K and with 1.89 eV excitation. Valley splitting data not shown in the main text are given in Fig. 4.10; D1 and D2 are defined in the main text, and the additional device is called D3. For D3, we took data at two different positions on the flake. We have also provided Table 4.1 showing the slopes extracted from linear fits to this data. The standard deviation across samples of the trion splitting is $0.003 \frac{\text{meV}}{\text{T}}$ and the standard deviation of the exciton splitting is $0.01 \frac{\text{meV}}{\text{T}}$. These values are within the systematic error estimated from the CCD pixel size. For one of the locations on D3, there was a significant discrepancy between the exciton and

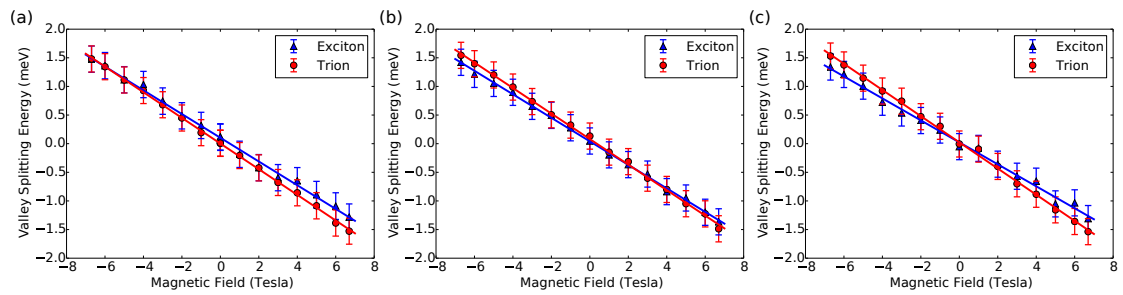


Figure 4.10: Comparison of Sample Valley Splitting. (a) Valley splitting data for D1, as defined in the main text. (b) Valley splitting data taken near the center of D3. (c) Valley splitting data taken near one edge of D3.

trion splitting.

Sample	Exciton Splitting ($\frac{\text{meV}}{\text{T}}$)	Trion Splitting ($\frac{\text{meV}}{\text{T}}$)
D1	-0.22	-0.22
D2	-0.21	-0.22
D3 location 1	-0.21	-0.22
D3 location 2	-0.19	-0.23

Table 4.1: Valley splitting for multiple devices in $\frac{\text{meV}}{\text{T}}$, defined as the difference of luminescence peak energies between σ_+ and σ_- polarized light. The error for all values is $\pm 0.01 \frac{\text{meV}}{\text{T}}$.

We also measured the gate dependence of valley splitting and polarization on two devices: D2 and another device not previously defined, D4. The gate dependence of luminescence from D4 is shown in Fig. 4.11. As shown in Fig. 4.11a, for D4 the trion polarization increases from about 10% to over 45% as the electron density is increased. For the data in Fig. 4.11 we used excitation light with equal intensity in σ_+ and σ_- polarization, and about 11 μW excitation power.

4.7 S4. Further Discussion of the Trion Luminescence and its Gate Voltage Dependence

Figure 4.12 shows the three possible trion spin-valley configurations which emit σ_+ polarization light on recombination (upper panels) and the corresponding final states after recombination (lower panels). These are the trion species defined as K_+ valley trions in the main text. There are also three more trion configurations not shown in Fig. 4.12 (the K_- valley trions) which are related to the configurations shown by time-reversal symmetry, and which emit σ_- light on

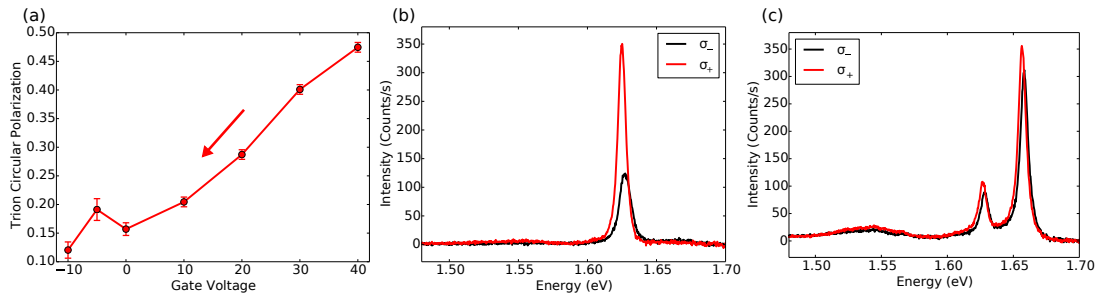


Figure 4.11: Gate Dependence of D. (a) Trion peak polarization versus gate voltage at $B = 6.7$ T for D4 taken on a downward sweep and using $11\mu\text{W}$ excitation with equal intensity in σ_+ and σ_- light (b) Polarization-resolved luminescence spectrum of D4 taken at 6.7 T magnetic field and 40 V back-gate voltage. (c) Polarization-resolved luminescence spectrum of D4 taken at 6.7 T magnetic field and -20 V back-gate voltage. The trion polarization is significantly reduced compared to the 40 V spectrum.

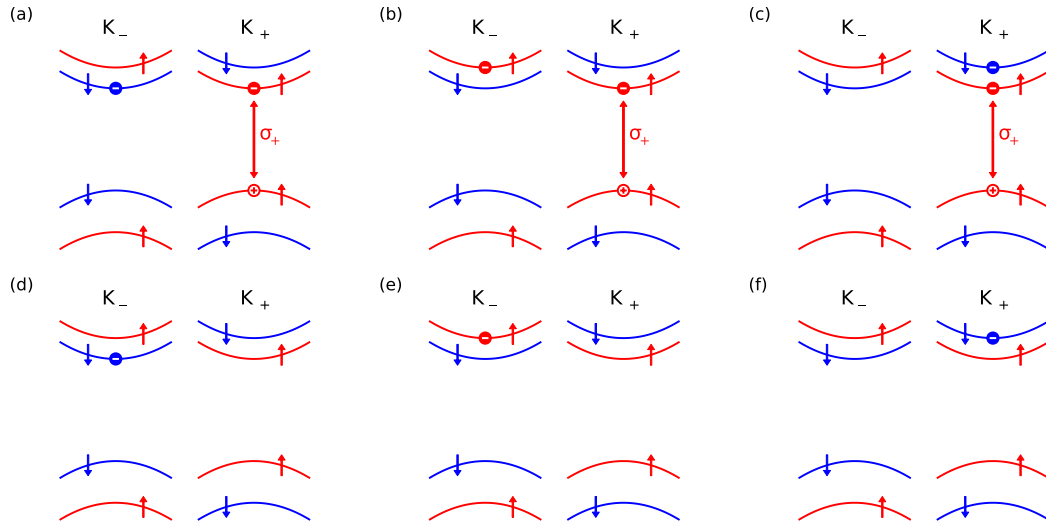


Figure 4.12: Band Diagrams for Gate Dependence of Trion Luminescence. Here we show the three possible trion spin-valley configurations which emit σ_+ polarized light on recombination (panels (a)-(c)) and the corresponding final states after recombination (panels (d)-(f)). In these schematic drawings, the full circles represent the two electrons in the trion, and the open circle represents the hole. We have arranged the panels so that the final state is below the initial state. The configurations shown here are the complete set of trion configurations emitting σ_+ light, but there are three more which emit σ_- light which are related to these via time-reversal symmetry. For the gate-voltage regime considered in our experiment, we expect that photoluminescence primarily arises from recombination of the trion species in panel (a) and its time-reversed partner.

recombination. In total there are then six trion configurations expected to have approximately the same binding energy, although the electron-hole exchange interaction is predicted to increase the energy of trions with parallel electron spins by about 6 meV [73]. Any trion configurations in which the two electrons have the same quantum numbers (spin and valley) have not been included in this accounting since they are not expected to be bound due to Pauli blocking. For MoSe₂ at low carrier density, only the lowest conduction bands will be occupied at 4.2 K since the conduction band spin-splitting is predicted to be about 20 meV [32, 61, 62]. As a result, the trion species in panel (a) is expected to be dominant at low carrier density. Based on Fig. 4d of the main text, we see that the conduction band edge for our samples is at approximately -12 V on a downsweep and therefore as an upper bound we gate into the conduction band by about $\frac{C\Delta V}{eA} / \frac{m_c}{\pi\hbar^2} \approx 20$ meV at our highest gate voltages (using $C \approx 1.2 \times 10^{-8}$ F/cm⁻¹ as the back-gate capacitance per unit area). The presence of trap states means this is probably an overestimate and we expect that the observed luminescence signal primarily arises from recombination of the panel (a) trion (and the time reversed version emitting σ_- light) at all gate voltages studied in this work.

In magnetic field, the total Zeeman energy of the trion can be approximated as the sum of the Zeeman energies of its constituent electrons and hole (the hole Zeeman energy being minus that of the relevant valence band). For example, the photon emitted when the trion in panel (a) recombines has energy: $E_{\text{initial}} - E_{\text{final}} = \epsilon_c + E_Z^c - \epsilon_v - E_Z^v + \epsilon_c - E_Z^c - E_B - (\epsilon_c - E_Z^c) = \epsilon_c - \epsilon_v - E_B + E_Z^c - E_Z^v = \hbar\omega + E_Z^c - E_Z^v$, where E_B is the sum of the exciton and trion binding energies (i.e. the total trion binding energy below the electronic band-gap), and $\hbar\omega$ is the trion emission energy for zero magnetic field. The trion valley splitting is then $2(E_Z^c - E_Z^v)$ and

equal to the exciton valley splitting. Similar calculations give the same results for the transitions shown in panels (b) and (c).

To estimate the gate dependence of the trion polarization we use a simple rate-equation model. In this model we assume that, for $B > 0$, the conversion rate of K_+ valley trions into K_- valley trions is suppressed by a Boltzmann factor of $e^{-2\beta E_Z^v}$ compared to the time-reversed process [74], where $\beta = \frac{1}{k_B T}$ with T the effective temperature of the trion population. The argument of the Boltzmann factor is determined by the energy barrier for switching from the trion species in panel a), with its hole in K_+ valley, to its time reversed partner with a hole in K_- valley: this energy is given by $E_{\text{initial}}(K_-) - E_{\text{initial}}(K_+) = 2E_Z^v$. We will also assume that, due to our off-resonant excitation, the formation rate Q of K_+ and K_- trions is roughly equal. The resulting rate equation is:

$$\begin{cases} \frac{dn_+}{dt} = Q - n_+/\tau_R + n_-/\tau_{\text{vl}} - n_+e^{-2\beta E_Z^v}/\tau_{\text{vl}} \\ \frac{dn_-}{dt} = Q - n_-/\tau_R - n_-/\tau_{\text{vl}} + n_-e^{-2\beta E_Z^v}/\tau_{\text{vl}} \end{cases} \quad (4.3)$$

where n_{\pm} is the trion population in the K_{\pm} valley, $1/\tau_R$ is the trion recombination rate, and $1/\tau_{\text{vl}}$ is the rate for K_- to K_+ intervalley scattering of the trion. In this simple model we have also ignored the possibility that the recombination rate may depend on the valley. The steady state solution is:

$$P_{\text{trion}} = \frac{n_+ - n_-}{n_+ + n_-} = \frac{\frac{\tau_R}{\tau_{\text{vl}}} (1 - e^{-2\beta E_Z^v})}{1 + \frac{\tau_R}{\tau_{\text{vl}}} (1 + e^{-2\beta E_Z^v})} \approx \frac{\frac{\tau_R}{\tau_{\text{vl}}}}{1 + \frac{\tau_R}{\tau_{\text{vl}}}} \quad (4.4)$$

where the second equality is obtained by ignoring the Boltzmann factor $e^{-2\beta E_Z^v} \approx 0.0004$ at 4.2 K and 6.7 T. At low gate voltages we find $P_{\text{trion}} \approx 0.18$ for the data in Fig. 4c of the main text or $\frac{\tau_R}{\tau_{\text{vl}}} \approx 0.2$. This is about an order of magnitude larger than the value of $\frac{\tau_R}{\tau_{\text{vl}}} \approx 0.03$ found by Ref. [75]; however, their value was obtained in significantly different experimental conditions since they studied

WSe₂ samples using resonant excitation and at zero magnetic field. In Fig. 4.13a, we plot the intervalley scattering rate normalized to the recombination rate $\frac{\tau_R}{\tau_{vl}} \approx |P_{\text{trion}}| / (1 - |P_{\text{trion}}|)$ versus gate voltage. The data shows a linear increase in intervalley scattering with carrier density, consistent with the Bir-Aronov-Pikus mechanism for intervalley hole scattering by the background conduction electrons [19, 71]. As discussed in section 7 of the supplement, we also observe a decrease in the trion polarization with increasing excitation power. This is qualitatively consistent with the rate-equation model assuming that the effective temperature of the trion population increases with excitation power.

In Figure 4.13b we show the peak intensity of trion luminescence in σ_+ and σ_- detection versus gate voltage. At small gate voltages, the trion luminescence intensity increases with increasing gate voltage for both σ_+ and σ_- detection, but the intensity of σ_- luminescence begins to decrease significantly above 15 V. As shown in Fig. 4.13c, the trion valley splitting changes only for gate voltages above about 15 V, suggesting that the increase in the valley splitting magnitude and decrease in the σ_- intensity could be related. Since the trion can recombine with a range of center of mass wavevectors [26], the change in valley splitting may result from a change in the k -space distribution of the K_- trion population rather than a change in the band Zeeman energies; the trion recombination energy redshifts as the final state center of mass momentum is increased. The redshift of K_+ trions compared to K_- trions would then correspond to a hot luminescence effect where the trion scattering rate from the K_- to K_+ valley is larger at larger wavevectors.

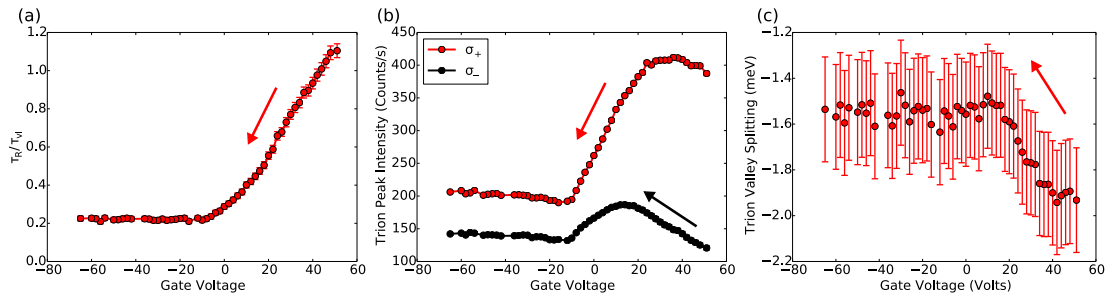


Figure 4.13: Trion Valley Scattering Rate. (a) Gate voltage dependence of $\frac{\tau_R}{\tau_{vl}}$ as defined in the text. This is the same dataset as used for Fig. 4.6c of the main text: it was taken for sample D2 at 4.2 K and 6.7 T magnetic field, using an excitation power of about $12.5 \mu\text{W}$ and σ_- excitation. The arrow represents the direction of the gate-voltage sweep. (b) Peak intensities of trion luminescence in σ_+ (red) and σ_- (black) detection versus gate voltage at 4.2 K and 6.7 T, taken for sample D2. (c) Trion valley splitting versus gate voltage at 4.2 K and 6.7 T, taken for sample D2.

4.8 S5. Calculations of the Exciton Valley Splitting within $\mathbf{k} \cdot \mathbf{p}$

Theory and Tight-binding Models

The magnetic moment of a band b can be calculated in $\mathbf{k} \cdot \mathbf{p}$ theory using the formula [68, 31, 76, 77, 78, 32]:

$$m_b = -\frac{\mu_B}{2m_e} \sum_{a \neq b} \frac{|P_+^{ba}|^2 - |P_-^{ba}|^2}{\epsilon_b - \epsilon_a} \quad (4.5)$$

where m_e is the free electron mass, μ_B is the Bohr magneton, ϵ_a is the energy of band a , and $P_{\pm}^{ba} = \langle b | p_x \pm ip_y | a \rangle$ is proportional to the optical matrix element for σ_{\pm} light between Bloch states $|a\rangle$ and $|b\rangle$. The formula above gives the z component of the magnetic moment, assuming $\{x, y, z\}$ form a right-handed coordinate system. As discussed in early papers on Bloch electrons in magnetic fields [68, 76], this formula includes both contributions from the phase winding of the Bloch state within a unit cell (the atomic contribution to the magnetic moment) and the phase winding on the scale of multiple unit cells (the intercellular contribution to the magnetic moment). The optical matrix elements are determined by the $\mathbf{k} \cdot \mathbf{p}$ Hamiltonian matrix elements, since $H_{\mathbf{k}\cdot\mathbf{p}} = \frac{\hbar}{2m_e} (k_+ p_- + k_- p_+)$, where $k_{\pm} = k_x \pm ik_y$, $p_{\pm} = p_x \pm ip_y$, and where \mathbf{k} and \mathbf{p} are the wavevector and momentum operator respectively.

In Table V of Ref. [32], Kormányos *et al.* give the non-zero $\mathbf{k} \cdot \mathbf{p}$ matrix elements within their theory. The resulting valley Zeeman energies (as defined in the main text) are:

$$E_Z^c / \mu_B = \frac{2m_e B |\gamma_3 / \hbar|^2}{\epsilon_c - \epsilon_v} - \frac{2m_e B |\gamma_5 / \hbar|^2}{\epsilon_c - \epsilon_{v-3}} - \frac{2m_e B |\gamma_6 / \hbar|^2}{\epsilon_c - \epsilon_{c+2}} \quad (4.6)$$

in the conduction band and

$$E_Z^v / \mu_B = -\frac{2m_e B |\gamma_3 / \hbar|^2}{\epsilon_v - \epsilon_c} + \frac{2m_e B |\gamma_2 / \hbar|^2}{\epsilon_v - \epsilon_{v-3}} + \frac{2m_e B |\gamma_4 / \hbar|^2}{\epsilon_v - \epsilon_{c+2}} \quad (4.7)$$

in the valence band, where ϵ_{c+2} is the energy of the second band above the conduction band and ϵ_{v-3} is the energy of the third band below the valence band. Here the parameters γ_i are related to the interband optical matrix elements, and the authors of Ref. [32] determine relevant combinations of these parameters via fits to the DFT band structure; details of the fitting procedure can be found in Refs. [64, 79]. In our case, the precise values of these parameters are not important, as we will focus on the relationship between the effective masses and valley splitting that can be derived using the $\mathbf{k} \cdot \mathbf{p}$ approach. The $\mathbf{k} \cdot \mathbf{p}$ theory effective masses can be written in terms of the γ_i similar to the Zeeman splitting (see Eq. B6 of Ref. [32]). Some simple algebra then allows us to obtain:

$$g_{\text{ex}}^{\text{vl}} = \frac{2(E_Z^c - E_Z^v)}{\mu_B} = 4 - 2 \left(\frac{m_e}{m_c} - \frac{m_e}{|m_v|} \right) \quad (4.8)$$

where $m_{c(v)}$ is the effective mass of the conduction (valence) band. As long as the effective masses for conduction and valence band are approximately equal, as expected from first principles calculations [80, 79], the valley splitting calculated this way will be close to $g_{\text{ex}}^{\text{vl}} = 4$ and have the opposite sign to our measurements. For example, taking $m_c = 0.49m_e$ and $|m_v| = 0.59m_e$ (these values are from [79]) gives $g_{\text{ex}}^{\text{vl}} = 3.3$.

The exciton valley splitting can also be calculated using a lattice model. For example, Ref. [18] originally proposed a model Hamiltonian for TMDs based on hybridization of d -orbitals at different Mo lattice sites. Such a lattice model neglects the atomic-scale structure of the wave function, and therefore the Zeeman coupling to the d -orbital magnetic moment must be introduced by hand [65, 66]. This gives a contribution to the band Zeeman energies of $E_{Z,a}^c = 0$ and $E_{Z,a}^v = 2\mu_B$, as discussed in the main text. Aside from this contribution, there is the magnetic moment due to phase winding of the Bloch states on the intercellular scale. This quantity can be calculated using the $\mathbf{k} \cdot \mathbf{p}$ theory formula Eq. 4.5

above, but this time within the reduced Hilbert space of the lattice model. For example, the Hamiltonian in the massive Dirac fermion model is:

$$H = \begin{pmatrix} \epsilon_c & \tau\gamma_3 q_{-\tau} \\ \tau\gamma_3^* q_{\tau} & \epsilon_v \end{pmatrix} \quad (4.9)$$

written in the basis of band-edge Bloch functions $\{|c\rangle, |v\rangle\}$. The resulting value for the intercellular Zeeman energy is $E_{Z,ic}^{c(v)} = \mu_B \frac{2m_e B |\gamma_3 / \hbar|^2}{\epsilon_c - \epsilon_v}$. Here we have used that $\langle c|p_+|v\rangle = 2m_e \gamma_3 / \hbar$. We note that $\frac{\hbar^2}{2m_c} = \frac{|\gamma_3|^2}{\epsilon_c - \epsilon_v}$ for this model so that the Zeeman energy is simply $\mu_B B \frac{m_e}{m_c}$. In a given valley this contribution shifts the energy levels in the conduction and valence bands in the same way, and therefore does not contribute to the exciton valley splitting. The total exciton valley splitting for this model is $2(E_Z^c - E_Z^v) = 2(E_{Z,a}^c - E_{Z,a}^v) + 2(E_{Z,ic}^c - E_{Z,ic}^v) = -4\mu_B$ as discussed in the main text. The same approach of separately treating the inter and intra cellular contributions can be used to calculate the exciton valley splitting in more general lattice models where the electron and hole masses are not equal, giving a value for the exciton valley splitting which differs from the bare d -orbital one [65, 66].

Finally, we discuss the effective Hamiltonian for excitons in magnetic field. The exciton Hamiltonian is found by subtracting the conduction and valence band dispersions and adding the electron-hole Coulomb interaction V :

$$H_{\text{ex}} = H_c(-i\hbar\nabla_e, \mathbf{r}_e) - H_v(i\hbar\nabla_h, \mathbf{r}_h) + V(|\mathbf{r}_e - \mathbf{r}_h|) \quad (4.10)$$

$$= \frac{\hbar^2}{2m_c} (-i\hbar\nabla_e + e\mathbf{A}(\mathbf{r}_e))^2 - \frac{\hbar^2}{2m_v} (-i\hbar\nabla_h - e\mathbf{A}(\mathbf{r}_h))^2 + V(|\mathbf{r}_e - \mathbf{r}_h|) + \frac{1}{2} g_{\text{ex}}^{\text{vl}} \mu_B B \tau. \quad (4.11)$$

Following Refs. [81, 82], we carry out a gauge transformation to find a one-body Hamiltonian for excitons with zero center of mass momentum:

$$H_{\text{ex}}^r = \frac{\hbar^2}{2\mu} \mathbf{k}^2 + \frac{\hbar e B}{2} \left(\frac{1}{m_c} - \frac{1}{|m_v|} \right) l_z + \frac{e^2 B^2}{8\mu} \mathbf{r}^2 + V(|\mathbf{r}|) + \frac{1}{2} g_{\text{ex}}^{\text{vl}} \mu_B B \tau \quad (4.12)$$

where $\mathbf{r} = \mathbf{r}_e - \mathbf{r}_h$ is the electron-hole separation, \mathbf{p} is the associated canonical momentum, $\mu = m_c|m_v|/(m_c + |m_v|)$, and $l_z = \hat{z} \cdot (\mathbf{r} \times \mathbf{p})$. For bright excitons we assume $l_z = 0$, i.e. that they are s -type [83, 70, 84]. Therefore the only term which can give rise to a linear magnetic field dependence of the exciton energy is the last term in Eq. 4.12, which describes a Zeeman-like coupling of the exciton valley degree of freedom to the magnetic field.

We also estimate the energy shift due to the quadratic term $\frac{e^2 B^2}{8\mu} \mathbf{r}^2$ in the exciton Hamiltonian. In the regime where the magnetic length ($l_B = \sqrt{\frac{\hbar}{eB}}$) is smaller than the exciton Bohr radius, this term leads to a quadratic shift of the exciton transition energy as demonstrated in experiments on quantum wells [82, 85, 86, 87]. Theoretically, this could manifest in our experiments as a quadratic term in the valley-averaged transition energy, but due to the small exciton Bohr radius for TMDs (1-3 nm [84, 70]) the correction should be small. We can estimate the diamagnetic shift using perturbation theory with the Wannier model above: the result is a quadratic increase of order $\frac{1}{8}\hbar(\omega_c + \omega_v)\left(\frac{a_B}{l_B}\right)^2 \approx 7 \mu\text{eV}$ at 6.7 T, where $\omega_{c(v)}$ is the electron (hole) cyclotron frequency, and a_B is the exciton Bohr radius. This energy shift is below our measurement sensitivity.

4.9 S6. Experimental Determination of the Sign of the Valley

Splitting

In the main text, we define the valley splitting as the difference of peak luminescence energies between σ_+ and σ_- polarized emission. Furthermore, σ_{\pm} polarization is defined as the circular polarization which carries $\pm\hbar$ angular momentum per photon along the field direction for $B > 0$. Equivalently, σ_+ (σ_-)

polarized light can be defined as the light with electric field vector rotating counter-clockwise (clockwise) in time around the positive B axis. The convention for $B > 0$ is defined in Fig. 1a of the main text. To determine the sign of the splitting, we used two methods.

First, we determined the rotational settings of the detection polarizer corresponding to different circular polarizations of emission. To do this, we launched circularly-polarized laser light into the cryostat objective lens from the sample space, and found the settings of the detection polarizer which maximized the resulting signal. The circularly-polarized light was generated by sending linearly polarized light through a $\lambda/4$ plate with the light polarized at 45° to the waveplate axes. Given knowledge of the waveplate axes and their orientation relative to the light polarization, the handedness of circularly-polarized light produced in this fashion can be determined. We also checked the assignment of the waveplate fast and slow axes by shining circularly-polarized light of a known handedness through the waveplate and analyzing the resulting linear polarization. For this test, the circularly-polarized light was generated using two N-BK7 prisms in a Fresnel rhomb geometry, so that the resulting handedness could be determined from the Fresnel equations. We determined the field direction using a calibrated Hall probe. The considerations above determine the rotational settings of the detection polarizer corresponding to detection of σ_+ and σ_- emission.

We also compared the valley splitting for MoSe_2 to magnetoluminescence measurements for a (110) cut, undoped, p -type CdTe substrate (from MTI Corporation). For p -type CdTe, the acceptor-bound exciton luminescence shows a four-fold splitting under magnetic field applied in the Faraday geometry. The

optical selection rules lead to circular polarization of these peaks, so that two are σ_+ polarized and two are σ_- polarized. With the detection polarization determined as discussed above, we find peak splitting and selection rules for CdTe in agreement with those found by Refs. [57, 58, 59]. In particular, given that the lowest energy acceptor-bound exciton luminescence peak for CdTe is σ_- polarized (for $B > 0$), we know that the lowest energy MoSe₂ peak indeed originates from σ_+ polarized luminescence (for $B > 0$) as indicated in the main text.

4.10 S7. Power Dependence of Trion Polarization

As shown in Fig. 4.14a, the trion luminescence polarization increases to about 65% circularly-polarized as the power is reduced for $B = 6.7$ T, $T = 4.2$ K, and in the regime of high electron density. On the other hand, we see no power dependence of the trion peak splitting (see Fig. 4.14b). Within our rate equation model, the power dependence of trion polarization arises from changes in the lattice temperature, or the effective temperature of the trion population which may not be equilibrium with the lattice. A thermometer mounted on the chip holder shows < 50 mK sample heating under more than $200 \mu\text{W}$ excitation, suggesting that the lattice heating is small. Figure 4.14c shows the gate dependence of trion polarization at 6.7 T and 4.2 K, with an excitation power of about $1.1 \mu\text{W}$; the fractional increase in the trion polarization with gate voltage is similar to data shown in the main text (taken with about $11 \mu\text{W}$ excitation).

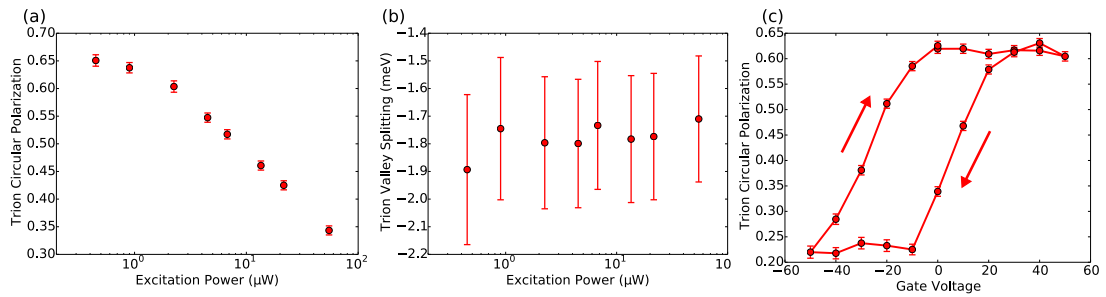


Figure 4.14: Power Dependence of Trion Polarization. (a) Trion peak circular polarization versus power in the n -type regime, for $B = 6.7$ T, and excited with σ_- polarized light. (b) Trion valley splitting versus power in the n -type regime and for $B = 6.7$ T. (c) Trion peak circular polarization versus gate voltage, taken at 6.7 T and using about $1.1 \mu\text{W}$ excitation power.

CHAPTER 5

FUTURE DIRECTIONS

Our combined microscopy, spectroscopy, and electrical measurement system has potential for a number of different materials systems. One particularly interesting system is the combination of complex oxide materials with effectively two-dimensional (2D) materials like graphene, boron nitride, and single or few layer transition-metal-dichalcogenides (TMDs) like AB_2 where A is Mo or W and B is S or Se. Combination of these 2D materials with each other is already a large field of study where local electrostatic environments, interface effects, and epitaxy lead to new or enhanced properties [88][89]. Combining the wide array of properties and symmetries found in complex oxides with the novel optical, mechanical, and transport properties found in these two-dimensional materials gives us potential access to new device functionalities. Among all the possibilities, we will focus on the combination of ferroelectric oxides with TMDs and graphene.

5.1 Introduction to Ferroelectrics as Gate Oxides for 2D Materials

The incorporation of ferroelectric oxides into semiconductor-based devices is a research direction motivated both by the large dielectric constants of ferroelectric oxides and the potential for using the hysteretic behavior of the polarization in the ferroelectric for memory applications. Effort has been made both to include ferroelectrics as the gate oxide for Si based field effect transis-

tors (FETs) and to incorporate ferroelectric capacitors into non-volatile one capacitor, one transistor based memory architectures [90][91][92] [93]. The large remnant polarizations of the ferroelectric gate or capacitor material can be used as two states of a memory system. Many issues related to materials compatibility, fatigue, non-volatility, and device read-out have been investigated with a predominant focus on incorporation of a wide variety of different ferroelectric chemistries with silicon fabrication techniques. FET geometry devices have been proposed and studied that use a variety of different ferroelectric oxides with insulating buffer layers between the ferroelectric and the Si channel in a metal-ferroelectric-insulator-semiconductor type structure. The inclusion of a dielectric between the ferroelectric and the semiconductor leads to a depolarization field that degrades the remnant polarization of the gate in time and can lead to volatility of the memory [90]. Commonly amorphous Hf-Al-O based buffer layers are used, as the high dielectric constant and high crystallization temperatures allow for better cycling behavior and long data retention times though the on-off ratio is still reduced by a factor of 10 on the time scale of ten days[93]. Molecular beam epitaxy (MBE) techniques have also been used to grow ferroelectric films directly onto Si with no buffer layer, though no FET type devices have been reported from these heterostructures [92].

Aside from integration with Si, oxide ferroelectrics have also been proposed and investigated as gate oxides and substrates for single layer graphene (SLG) and few layer graphene (FLG) based devices [94][95]. Commonly graphene devices are constructed with dielectric back or top gates for modulation of the Fermi level and carrier concentration of the graphene layer, which also serve as a mechanical support for the 2D material. The transport properties of the graphene are highly dependent on the electronic properties of these gate di-

electrics, with SiO₂ as a common choice. The morphology, chemistry, structural, and electronic properties of this gate material choice all can contribute extrinsic sources of scattering to a graphene based device limiting its performance. [94][96][97]. Hong et al demonstrated that swapping the gate oxide from SiO₂ for ferroelectric Pb(Zr_{0.2}Ti_{0.8})O₃ (PZT) increased the room temperature mobility of FLG to 70% of the theoretical limit from electron-phonon scattering, with low temperature mobilities as high as 1.4×10^5 cm²/V s [94]. These devices should also show a resistance hysteresis as the polarization of the gate is changed but that was not initially reported. This same group later reported measurements of the graphene resistance in similar devices (both FLG and SLG based) as the gate oxide polarization was changed, but this resistance showed an unexpected hysteretic behavior. The devices showed the direction of the hysteresis as opposite to that expected from carrier density change induced by the polarization reversal of PZT. They coined the term "antihysteresis" and attributed the behavior to interfacial defects between the graphene and the PZT, in particular to disassociated water molecules trapped at the interface to screen the native polarization of the PZT [98]. This behavior has been observed multiple times, and has been proposed as a mechanism to construct resistive non-volatile memory elements [99]. Other groups have reported similar antihysteresis behavior for graphene devices on SrTiO₃ (STO) thin films grown on Nb doped SrTiO₃ substrates with no measured ferroelectricity [100].

This issue of antihysteresis, which is attributed to substrate cleanliness and crystal quality, raises the question of how to eliminate the charged defects at the interface between the 2D material and the ferroelectric. The remnant polarization of the ferroelectric substrate means that charged adsorbates will be drawn to the surface to screen the polarization and cleaning efforts need to somehow

account for this. Surface crystalline defects may also contribute charged defects due to the polar nature of the chemistries involved in ferroelectrics. An obvious potential solution to cleaning the ferroelectric surfaces is to construct and clean the sample while the ferroelectric is above its Curie temperature (T_c) or while it is heated to reduce the remnant polarization at the surface. Recently, Yusef et al have demonstrated that they can construct graphene ferroelectric FETs using $\text{PbTiO}_3/\text{SrTiO}_3$ (PTO/STO) superlattices with a tunable T_c based on the volume fraction of PbTiO_3 in the superlattice [101]. They heated their substrates to 250°C in ambient conditions which both reduces the polarization by 75% and also had been shown previously to aid in the removal of physisorbates on ferroelectrics. They demonstrate that they can tune from a hysteretic to an antihysteretic device behavior by tuning the superlattice surface morphology, where reducing surface pits and using atomically flat electrodes transitions from antihysteretic to hysteretic behavior in the graphene. This demonstrates that clean interfaces between 2D materials and ferroelectrics are possible, and that a clean interface can lead to effective gating of the 2D material.

The methods used to improve the quality of graphene and ferroelectric interfaces should be applicable to the integration of exfoliated semiconducting TMD based devices as well. We propose the construction of single layer or few layer TMD devices on ferroelectric oxides as novel semiconductor-on-ferroelectric FET type devices with a mix of interesting optical and transport properties. Ferroelectric gates with clean interfaces can give us access to gating charge densities larger than the equivalent charge densities at the breakdown of SiO_2 gates with smaller applied voltages due to the spontaneous polarization of the ferroelectric [90]. This gate is also tunable at low temperatures, unlike ionic liquid gates which are another route to charge densities above $1 \times 10^{14} \text{ cm}^{-2}$. TMD FET

structures with ionic liquid gates have demonstrated novel devices such as light emitting transistors and stable p-n junctions [102] [103] or enhanced mobility for single layer and few layer TMD FETs [104]. Combined photocurrent, spectroscopy, imaging, and transport measurements at low temperature will allow us to investigate electroluminescence, dependence of magneto-luminescence at larger carrier densities, as well as the interplay between optical excitation and transport properties of the devices.

Integrating single and bi-layer TMDs with ferroelectrics may also tell us about the spatial arrangement of the underlying ferroelectric domains through the photoluminescence (PL) of the TMD. As discussed in the introduction, the enhancement of PL in monolayer devices comes from the breaking of inversion symmetry. The polarization from the underlying ferroelectric should break this symmetry for bilayer or few layer systems as well giving enhanced PL signal. For MoSe₂ shifts in the trion to exciton PL ratios should also reflect the underlying ferroelectric domain structure, giving a potential means to image the ferroelectric domain structure optically for out-of-plane polarizations.

5.2 Finding a Relevant Ferroelectric

From the graphene studies, we need to avoid the antihysteretic behavior to take full advantage of the intrinsic polarization from the ferroelectric gate. PTO/STO superlattices and hot TMD transfer clearly offer a route to explore, but TMDs are less stable to heating in air than graphene. Ideally we would like to find a material that undergoes a ferroelectric transition with out-of-plane polarization below room temperature since we intend to investigate these devices at cryo-

genic temperatures anyways. This would allow us to prepare and clean the ferroelectric surface without the electrostatic attraction of charged adsorbates to screen the surface, then to cool through a phase transition to induce the spontaneous polarization. Unfortunately, oxides with sub-300 K Curie temperatures and out-of-plane ferroelectric domains are not very common. We are investigating two potential systems, bulk single crystals of solid solutions of $(\text{Ba,Sr})\text{Ti}_3$ and compressively strained STO thin films. We obtained two pieces of bulk single crystal of $\text{Ba}_{0.1}\text{Sr}_{0.9}\text{TiO}_3$ from Rainer Held, which were polished normal to the crystal c axis. For this composition, we would expect a Curie temperature below 100 K [105]. We cut these crystals into 4 discrete samples and used Epotek H20E silver epoxy to attach each crystal to a common metal plate. We then wired up each crystal independently into a capacitive geometry to measure the capacitance of the crystal along the c -axis. We cooled the crystals to 5 K in a Helium bath cryostat, both in zero electric field and with a 50 V bias across the crystals on two separate cool down cycles. We measured the capacitance as we increased the temperature slowly to above 100 K. In both cases, we saw a common temperature dependence of the capacitance across all samples that suggested we were seeing capacitance of pure STO. In the case of cooling without an applied 50 V bias, we did see a small jump in capacitance at 70 K though this was not repeatable with a bias. This behavior would be consistent with small regions of different dielectric constant in a STO matrix, though it is unclear why a bias on cooling would eliminate this behavior. We saw no indication that we were seeing a ferroelectric phase transition that would allow us to use this as a substrate for TMDs.

We are also looking at 1.1% compressively strained STO grown by reactive MBE on (110) oriented NdGaO_3 (NGO (110)) substrates, which is predicted to

have out-of-plane ferroelectricity below room temperature though this has not been confirmed conclusively by experiment [106] [107] [108]. STO strained on NGO (110) has been demonstrated to have a remnant polarization greater than $6 \frac{\mu\text{C}}{\text{cm}^2}$ below 20 K [109]. NdGaO₃ is insulating, so we need to grow a thin conducting buffer layer between the STO and the NGO to act as a gate electrode for the STO without relaxing the strain between the substrate and the STO film. At a first attempt, we grew a 30 u.c. SrVO₃ (SVO) using 2.8×10^{-7} torr of oxygen back pressure with a substrate temperature of 790^o C measured with the pyrometer as our electrode which showed smooth growth by RHEED and achieved residual resistivity ratio (RRR) values for these films around 5-6 indicating moderate film quality. We then tried to cool these films for STO growth in 10% ozone, but saw the surfaces roughen by RHEED with time. To combat this, we grew 10 u.c. of STO at the same SVO growth conditions to cap the surface, then cooled the substrate, switched from O₂ to 10% ozone and grew another 30 u.c. of STO at a pyrometer temperature of 750^o C and an ion gauge pressure of 8.5×10^{-7} torr. Figure 5. shows that we have smooth thin films of STO, with an increase in the c-axis lattice constant (STO film peak shifted to lower 2θ angle) compared to unstrained STO. This peak shift is consistent with compressive strain in the films but could also indicate stoichiometry issues.

The next steps are to measure the temperature dependence of the film capacitance to look for signs of a ferroelectric transition and also to measure the film polarization. If strained STO on NGO (110) will not work as a sub-room temperature out of plane ferroelectric, BaTiO₃/SrTiO₃ and PbTiO₃/SrTiO₃ superlattices with large STO volume fractions also show promise [108]. An advantage of using reactive MBE grown thin films for our 2D material based devices is that we can mechanically exfoliate our 2D materials immediately after film growth to

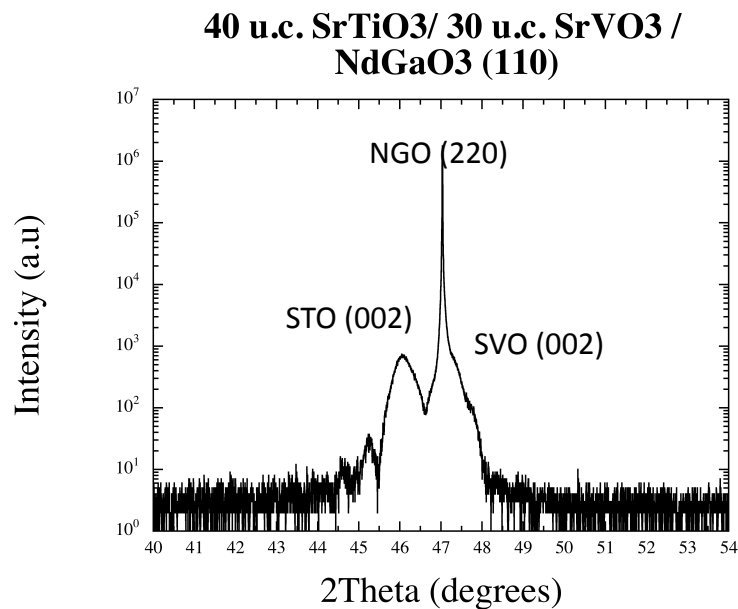
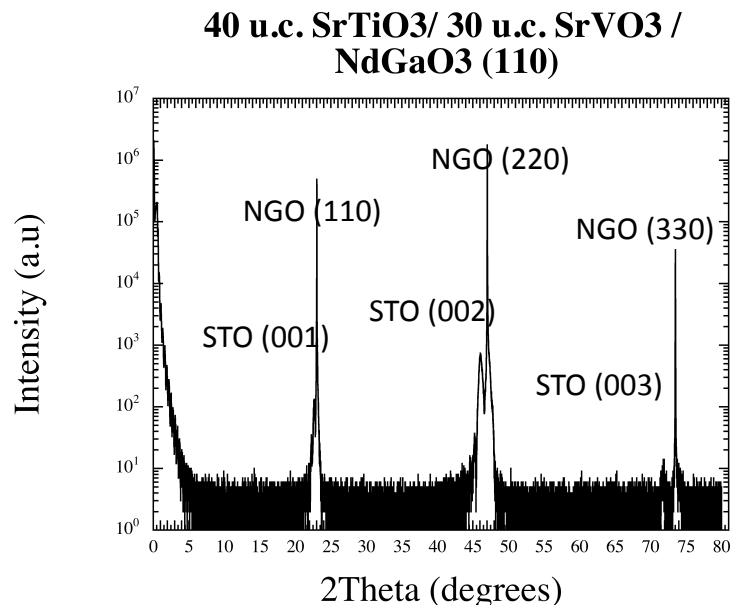


Figure 5.1: θ - 2θ Scans of SrTiO₃ Film on (110)NdGaO₃. Top scan shows 2θ range from 0° to 80° , with substrate and film peaks labeled. The SrVO₃ are hidden by the substrate peaks. Bottom scan shows 2θ range from 43° to 49° showing more clearly the (002) film peak and the side of (002) electrode peak. The STO film peak shows thickness fringes consistent with the number of unit cells grown.

reduce the chance of surface contamination.

5.3 Future Device Plans

If we are able to grow out-of-plane ferroelectric thin films and to make clean interfaces between these films and mechanically exfoliated TMDs, we can immediately investigate the TMD carrier mobility and optical properties with effective carrier densities up to an order of magnitude larger than is possible for SiO₂ gate dielectrics. Expanding to higher carrier densities should also allow us to investigate the mechanism of the gate dependence of the valley degeneracy breaking that we reported in chapter 4 and to potentially achieve both p and n doping regimes. We can envision making p-n junction type devices using a similar gating scheme to that used in ionic liquid gating studies, where we can write a ferroelectric domain wall underneath our TMD [103]. We also can achieve this with polarizations that are stable at zero bias after writing. We could effectively make non-volatile memory FETs or p-n junctions in a 2D semiconductor without chemical doping and large off currents. It is also possible that we will see mobility enhancements for TMDs on ferroelectrics similar to those observed on graphene. With a stable system for clean out-of-plane ferroelectric gating of TMDs, there are many more possibilities for devices that take advantage of the exciting physics of TMDs, the large polarizations at ferroelectric surfaces, and the non-volatility of ferroelectric domains.

APPENDIX A

**CURRENT STATE OF THE DILUTION REFRIGERATOR, AND UPDATED
SOPS**

Over the course of the last 6 years, weve made multiple changes to the electrical lines, the vacuum feedthroughs, the state of the mash, and the pumps and pumping lines for the dilution refrigerator. Both switch boxes have been modified significantly, the superconducting electrical lines for the nanopositioners have been added, the 1 K pot pump and the circulation pumps have both been replaced, the optical fiber feedthroughs have been added, and the temperature control and monitoring cable has been broken out. Here I will explain the changes made, how they related to the safe and proper operation of the refrigerator, and the issues related to the current mash ratio and volume. I will use the terminology from the Oxford Kevinox user manuals.

A.1 Electrical lines and switchboxes:

There are two switch boxes at the top of the dilution refrigerator that connect to two different vacuum electrical feedthroughs that run down into the inner vacuum chamber (IVC). Figure A.1 shows their relative positions. Both of these are 24 pin Fischer connectors. The switch box BNCs are labeled 1-24 and the numbers correspond to the labeled diagrams of the Fischer connectors from the Oxford manuals. Modifications have been to the lines down to the mixing chamber for each of these switch boxes. We've broken them down into a nanopositioning switchbox and a sample measurement switch box.

The switchbox A connector has been converted to a piezotube or nanopositioning

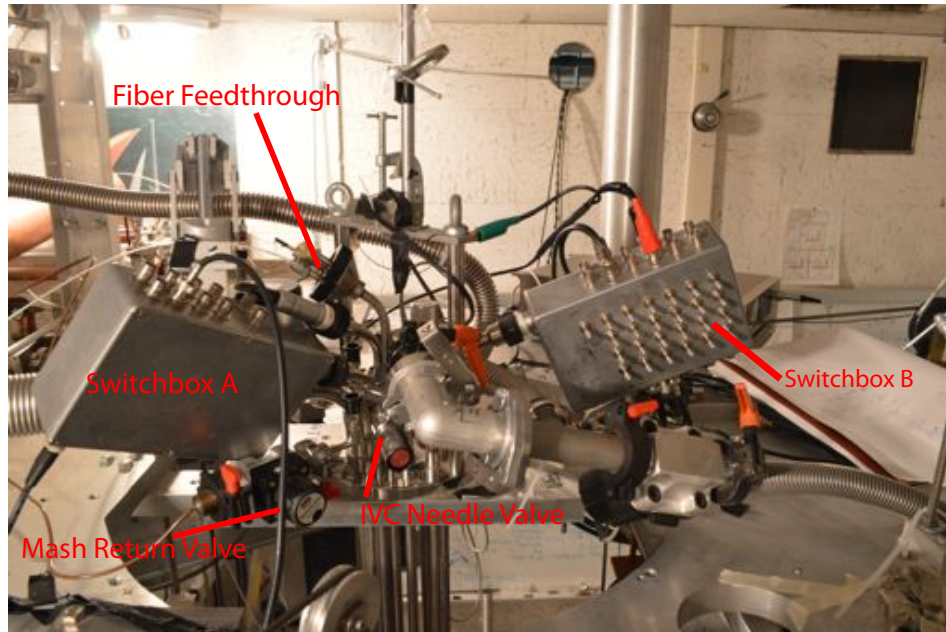


Figure A.1: Diagram of Kelvinox Switchboxes. Photo taken of the top of the dilution refrigerator showing the relationship between the switch boxes, the fiber optic feedthrough, the Inner Vacuum Chamber (IVC) needle valve, and the mash return line

sitioner controlling channel with 6 copper lines running into the fridge. These lines are thermalized at the 4 K plate, then soldered into a Samtec connector. The mate of that Samtec connector is soldered to BeCu clad NbTi wires which are then thermalized to the 1 K pot plate then the cold plate, and finally to the mixing chamber plate. The purpose of this multi stage wire assembly is to reduce the line resistance to reduce the RC constant of the piezo driving circuit for either the piezo tube or for the attocube nanopositioners. While the attocube manual states that there can be a 10 Ω resistance for the total loop between ground and the high voltage pin, weve found that this resistance must be under 5 Ω and should preferably be under 2 ohms total. The use of the normal metal-coated superconducting wires allows us to have high electrical conductivity at both room temperature and low temperature, while having a minimal thermal linkage between the various temperature stages while running the dilution refrigerator. Weve tried to use thin copper wires instead, but had large issues with driving the attocubes. We seem to see that the attocubes get mechanically jammed more often when the line resistance is over 5 ohms. The final key point for these nanopositioning lines is that since they are high voltage lines, seeing up to 300 V between pins from the piezotube controller, it is critically important to solder to the Samtec connectors delicately. Weve seen leakage between the pins and sparking if the plastic of the connectors sees too much heat during soldering. It is critically important to use a minimal amount of solder flux and to remove the flux carefully with isopropanol (IPA).

Switch box B has been modified extensively. The large, multi-pin rotary switch] that was used to tie all the BNCs to the same bus has been disconnected from the box due to a large amount of shorts between channels within the switch. Currently, each channel can be individually grounded using the

3 pole switches that correspond to each BNC, but they cannot be tied all to ground together with a single switch. There are also a few BNCs that are out of order with respect to the apparent geometric order. Pins 19, 20, 21, and 22 are swapped, where pins 21 and 22 are adjacent to pins 17 and 18 and then 19 and 20 follow. This is labeled in ink on the switch box next to the relevant BNCs. The measurement lines are all approximately $130\ \Omega$ from the switch box to the mixing chamber. There are some potential issues here with leakage between lines as measured at the switch box, but those issues have been hard to diagnose. I think its related to the position of the wires at the mixing chamber, as it seems that this can always be fixed by correctly strain relieving those wires, though sometimes things shift upon cooling. We also have some indication that this is an issue with the insulating coating on the old wires, since there sometimes seems to be a capacitive coupling between channels with an AC excitation. Careful measurement of the lines in their intended measurement state before cooling is essential.

A.2 Temperature Measurement

One of the complicating factors for the design of the microscope was how to deal with the inevitable temperature differential between the mixing chamber and the sample. While the temperature control cable has three channels of 4 point measurement and a heater channel for each stage, the AVS 47-b resistance bridge has the ability to control 9 separate channels. We have taken apart the connector that links the temperature control cable to the AVS bridges preamplifier and wired up the correct pins for channel 4 and channel 5 into the AVS. We use one of these channels to monitor the sample temperature.

Due to the complications from having a sample that can be moved with respect to the optical elements, significant temperature gradients between the sample and the mixing chamber are likely. It is essential to mount a temperature sensor on the sample mounting plate, whatever that geometry may eventually be. Figure 2.11 shows how we mount a temperature sensor to the standard low temperature chip holders that are around the lab. Note that we use lens tissue saturated with IPA thinned GE varnish both to thermalize the resistor to the sample holder and to attach the resistor to the sample holder with out electrical contact. For our bilayer strontium ruthenate experiments and for our optical calibration experiments, we used a single 5.6 K ohm resistor obtained from a batch calibrated by Eric Smith and John Reppy. The calibration table for this resistor is located on the shielded room door. It is important to note the zero field base temperature before sweeping field and to again note the temperature at field after it has stabilized from any eddy current heating. Since the resistor is sitting at the sample field, the magnetoresistance contributes. We see less than 5% change in the resistance at base temperature from 0 to 9 T.

A.3 1 K Pot Changes

Figure A.2 shows the state of the various pumps and things needed to run the dilution refrigerator. The 1 K pot for the dilution refrigerator functions using the refurbished Edwards E2M40 shown in that figure. This pump has a pumping rate of just under 30 CFM, and we had the electricians install a new circuit for this pump, which includes an on/off switch. There is no such switch on the pump. Over the years, the pump used to run the 1 K pot has changed, but it is essential to maintain this pumping rate going forward. When I started using



1. Circulation Pump
2. Oil Trap
3. 1 K Pot Pump
4. Return Line Pressure Gauge
5. Overpressure Shutoff Circuit for Circulation Pump
6. Switch for Circulation Pump

Figure A.2: Diagram of Pumps in Corridor. Photo taken of the mash circulation pump and the 1 K pot pump in the microKelvin access corridor. Relevant pumps, oil traps, pressure gauges, and control electronics are labeled.

the refrigerator, a single Edwards E2M8 pump with a pumping rate of 6 CFM was connected to the 1 K pot. Using a smaller pump leads to unacceptably long mash condensation times as well as a pot that is much more sensitive the setting of the needle valve. If the heat load to the 1 K pot gets too large compared to the cooling power, this can also give the appearance that the mash condensation lines are clogging during circulation. The 1 K pot exhaust line has a valve that switches between the He recovery system and a slight negative pressure house air return line. It is important to switch this to the house air line when starting the cool down process, and to switch it to the He recovery line when starting to pump on He. Due to the updates to the building, the two lines can be difficult to tell apart. The He recovery side is the one that runs through the fire protection foam into the space between the shielded room and the wall.

A.4 Mash Circulation Pump

One of the major changes made to the dilution refrigerator is the replacement of the Alcatel pump with a new magnetically coupled Pfeiffer sealed pump, shown in figure A.3. We have had a multitude of issues with the new pump, which all boil down to some sort of issue with the motor and the apparent back pressure of the pump convolved with the temperature of the pump oil and possibly the pump oil level. In practice, this means that a cold pump will not spin up to its maximum speed and draw the correct amount of current from the power supply when it is turned on with a back pressure over -20 Hg. The pump will start spinning, and you will see the fan on the motor, shown in figure A.3 start to spin slowly and with a start and stop pattern. At the same time, the top of the motor will start to get very warm and eventually this will trigger the



- | | |
|-----------------|-----------------------------|
| 1. Top of Motor | 3. Heating Belt and Foil |
| 2. Motor Fan | 4. Watch Glass for Pump Oil |

Figure A.3: Diagram of Circulation Pimp. Photo taken of the mash circulation pump with the motor and other parts important for use labeled

thermocouples in the motor and kill the motor to protect it. You will also hear a slow cyclic pulsing sound that will correspond with the motion that you can see on the motor fan. If this happens, turn off the pump so as to not damage the motor. This is frustrating, and it is out of spec for the pump. The pump should operate just fine up to atmospheric pressure at the back pressure, and a large amount of time was spent with the Pfeiffer rep to try to figure out what was going on. We think it might have something to do with the tolerances on the fit between the pump blades and the cast aluminum pump housing, or some sort of clog between the pump and the oil trap shown in figure A.2. If anyone is ever forced to open the mash return line, two things should be changed in an attempt to fix this more permanently. First, a pressure gauge should be added immediately at the outlet from the pump and the narrow spiral bellows should be swapped for a larger diameter vacuum line. Second, the oil level in the pump should be lowered to half way down the watch glass.

There are two ways to start up a cold pump, either by changing its temperature or changing the pressure in the return line. If the fridge has been running and if the mash has already been cleaned through the nitrogen traps and condensed, you can rely on cryopumping the mash into the fridge to lower the return pressure below -20 Hg on the return gauge, shown in figure A.2. If there is any chance that the mash could have been contaminated due to a leak, you should not try to condense it into fridge. There is a second volume that you can use to cryopump the mash and lower the return pressure. I have installed a cryopump stick into the gas handling system (shown in figure A.4) that fits into the He trap dewar. This stick currently contains clean He4 and may contain a very small amount of He3. Before discarding the gas in this stick, you can confirm that there is an unusable amount of He3 with the leak detector. When this

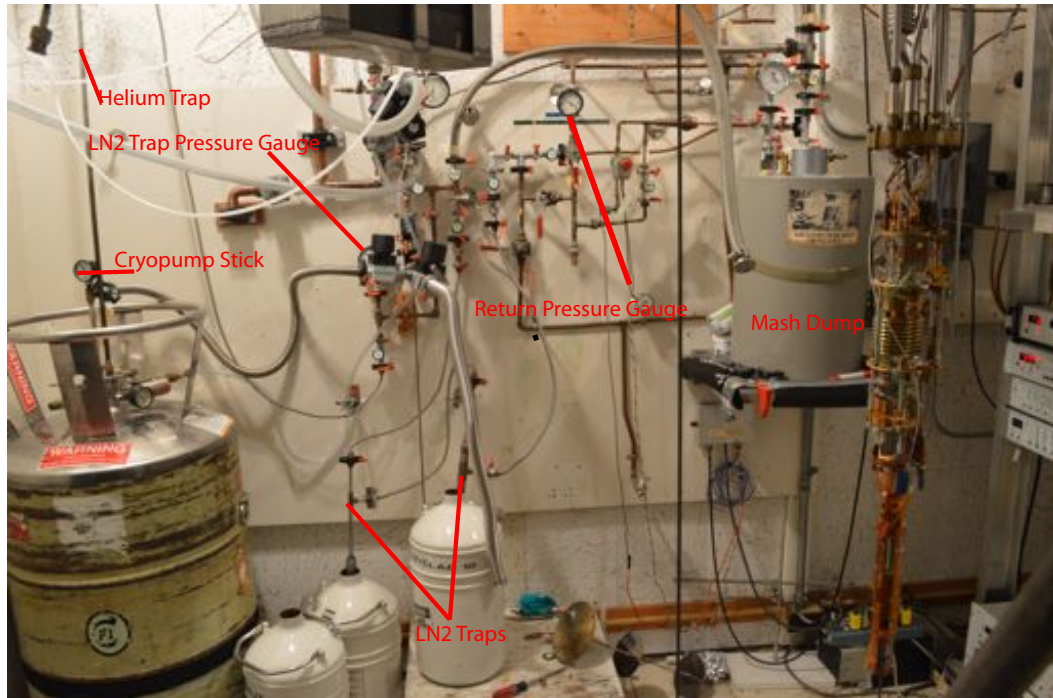


Figure A.4: Gas Handling System Diagram. Photo taken of the gas handling system for the Kelvinox dilution refrigerator.

stick is cold in the He trap dewar, shown in figure A.4, you can use it to store the mash in the return line safely while you work on the mash, the circulation pump, or some other aspect of the dilution refrigerator that requires you to vent those lines. This also allows you to cryopump the mash in the return lines to lower the pressure and get the pump started. I do not recommend this course of action, unless it is absolutely necessary or you have to vent the pump anyways.

Fortunately, there is an easy way to start the pump. I have borrowed a heating belt from the Shen group, which they do not need anymore. As is shown in figure A.3, the cast aluminum pump body is wrapped with aluminum foil, and this heating belt is then taped to the pump with Kapton tape. I turn on the heat belt to >80% power as shown on its controller and I wait until the pump body heats up until it is warm to the touch. While the pump is heating up, I try to turn it on every 20 min both to mix up the pump oil for more even heating and to check if the pump is ready. After 90 to 120 minutes, the pump will spin up to full speed and you can turn off the heating belt. It is important to keep an eye on the pump, and to make sure that the aluminum pump body continues to heat up from operation while the motor casing stays cool enough to be comfortably touched with bare hands. If the pump turns off during circulation, you can usually restart it immediately as it will stay hot during operation.

A.5 Optical Fiber Feedthroughs and Maintenance

There are three vacuum feedthroughs that can be used to run optical fibers down into the dilution refrigerator. Depending on the cladding of the fiber, different vacuum sealing methods can be used. One part of the seal is a Teflon

ferule modeled after the metal ferule in a swagelock connector. This clamps down on the fiber cladding and makes a seal between the cladding and the metal part of the feedthrough. For the standard Thorlabs fiber, there is a hard plastic casing inside the outer soft plastic and nylon fiber outer coating. This plastic casing does not make a vacuum tight seal with the fiber, and is difficult to remove safely without breaking the fiber. In order to make a vacuum tight seal, you need to remove some of the hard plastic and flow epoxy into the void between the fiber and casing.

The best way to do this is to make a Teflon ferrule that fits the hard casing, feed the fiber into the IVC through the ferrule with a nut, splice on the fiber termination, mount the fiber into the microscope insert, and then slightly tighten the Swagelock nut around the ferrule. You then need to get everything all set up like you are going to cool down a sample, including getting a sample or mirror into the focal plane of the microscope so you can monitor the light coming back out of the fridge. Seal up the IVC so you can pump on it with the leak detector or turbo pump. Now you need to cut a section out of the hard casing near the vacuum feedthrough and flow some stycast 1266 epoxy into the opening. While the epoxy is still fluid, you need to pull a slight vacuum on the IVC and let the pressure differential pull more epoxy into the void. Apply more epoxy every 30 minutes for 2 to 3 hours, then equalize the pressure and wait for the epoxy to cure for 24 hours. Tighten the Swagelock nut and make up a new batch of epoxy. Roughen the surfaces of the hard casing near your cut and the Swagelok connector with sand paper then clean all the surfaces with IPA. Pull vacuum on the IVC and flow fresh epoxy all over the Swagelok connector and your previous epoxy. Apply a new coating of epoxy every 30 minutes for 2 hours, then equalize the pressure and let the epoxy cure for 24 hours. After 24 hours, leak

check your new joint carefully. If it leaks, you can repeat the process of cleaning, flowing fresh epoxy, and pulling vacuum. During this entire process, you can monitor the reflected power to ensure that you are not breaking the fiber or changing its transmission. You will see some focus changes as you pump the IVC out, but you should not see changes in the reflection as you cure the epoxy.

I mentioned earlier that you need to splice on the fiber termination. In our design, we are using the standard FC/APC or FC/PC fiber terminations, but these connectors do not fit through the vacuum feedthrough. You need to cleave the fiber, and then re-splice on a new termination. This is not something that we have the equipment to do, but fortunately the Wise group has a fiber-splicing machine that can splice either polarization maintaining (PM) single mode or non-PM single mode fiber. They have been kind enough to help us whenever we need assistance in changing the fiber. If you think the fiber or the fiber termination is damaged, then you need to contact the Wise group to find out who is currently trained on the fiber splicer and who can help you. Be sure to always blank the beam and clean the fiber tip with the fiber cleaning cloth whenever you connecting the fiber to the optics in the microscope.

BIBLIOGRAPHY

- [1] A. Kapitulnik, J. Xia, E. Schemm, and A. Palevski, "Polar Kerr effect as probe for time-reversal symmetry breaking in unconventional superconductors," *New Journal of Physics*, vol. 11, no. 5, p. 055060, 2009.
- [2] T. Vuletić, B. Korin-Hamzić, S. Tomić, B. Gorshunov, P. Haas, T. Room, M. Dressel, J. Akimitsu, T. Sasaki, and T. Nagata, "Suppression of the Charge-Density-Wave State in $\text{Sr}_{14}\text{Cu}_{24}\text{O}_{41}$ by Calcium Doping," *Physical review letters*, vol. 90, no. 25, p. 257002, 2003.
- [3] M. Stern, P. Plochocka, V. Umansky, D. Maude, M. Potemski, and I. Bar-Joseph, "Optical probing of the spin polarization of the $\nu=5/2$ quantum Hall state," *Physical review letters*, vol. 105, no. 9, p. 096801, 2010.
- [4] A. García-Flores, D. A. Tenne, Y. Choi, W. Ren, X. Xi, and S. Cheong, "Temperature-dependent Raman scattering of multiferroic $\text{Pb}(\text{Fe}_{0.5}\text{Nb}_{0.5})\text{O}_3$," *Journal of Physics: Condensed Matter*, vol. 23, no. 1, p. 015401, 2011.
- [5] J.-P. Tetienne, T. Hingant, L. Rondin, A. Cavailles, L. Mayer, G. Dantelle, T. Gacoïn, J. Wrachtrup, J.-F. Roch, and V. Jacques, "Spin relaxometry of single nitrogen-vacancy defects in diamond nanocrystals for magnetic noise sensing," *Physical Review B*, vol. 87, no. 23, p. 235436, 2013.
- [6] M. Sladkov, M. Bakker, A. Chaubal, D. Reuter, A. Wieck, and C. van der Wal, "Polarization-preserving confocal microscope for optical experiments in a dilution refrigerator with high magnetic field," *Rev. Sci. Instrum.*, vol. 82, no. 4, p. 043105, 2011.
- [7] A. Högele, S. Seidl, M. Kroner, K. Karrai, C. Schulhauser, O. Sqalli, J. Scrimgeour, and R. J. Warburton, "Fiber-based confocal microscope for cryogenic spectroscopy," *Review of scientific instruments*, vol. 79, no. 2, p. 023709, 2008.
- [8] A. Fried, M. Fejer, and A. Kapitulnik, "A Scanning, All-Fiber Sagnac Interferometer for High Resolution Magneto-Optic Measurements at 820 nm," *arXiv preprint arXiv:1403.4227*, 2014.
- [9] J. Xia, P. T. Beyersdorf, M. M. Fejer, and A. Kapitulnik, "Modified Sagnac interferometer for high-sensitivity magneto-optic measurements at cryogenic temperatures," *Applied physics letters*, vol. 89, no. 6, p. 062508, 2006.

- [10] J.-F. Mercure, "The de Haas van Alphen effect near a quantum critical end point in $\text{Sr}_3\text{Ru}_2\text{O}_7$," *arXiv preprint arXiv:1001.3980*, 2010.
- [11] S. Grigera, P. Gegenwart, R. Borzi, F. Weickert, A. Schofield, R. Perry, T. Tayama, T. Sakakibara, Y. Maeno, A. Green *et al.*, "Disorder-sensitive phase formation linked to metamagnetic quantum criticality," *Science*, vol. 306, no. 5699, pp. 1154–1157, 2004.
- [12] R. Perry, L. Galvin, S. Grigera, L. Capogna, A. Schofield, A. Mackenzie, M. Chiao, S. Julian, S. Ikeda, S. Nakatsuji *et al.*, "Metamagnetism and critical fluctuations in high quality single crystals of the bilayer ruthenate $\text{Sr}_3\text{Ru}_2\text{O}_7$," *Physical review letters*, vol. 86, no. 12, p. 2661, 2001.
- [13] R. Borzi, S. Grigera, J. Farrell, R. Perry, S. Lister, S. Lee, D. Tennant, Y. Maeno, and A. Mackenzie, "Formation of a nematic fluid at high fields in $\text{Sr}_3\text{Ru}_2\text{O}_7$," *Science*, vol. 315, no. 5809, pp. 214–217, 2007.
- [14] R. Perry and Y. Maeno, "Systematic approach to the growth of high-quality single crystals of $\text{Sr}_3\text{Ru}_2\text{O}_7$," *Journal of crystal growth*, vol. 271, no. 1, pp. 134–141, 2004.
- [15] C. Stingl, R. Perry, Y. Maeno, and P. Gegenwart, "Symmetry-breaking lattice distortion in $\text{Sr}_3\text{Ru}_2\text{O}_7$," *Physical review letters*, vol. 107, no. 2, p. 026404, 2011.
- [16] J.-F. Mercure, S. Goh, E. O'Farrell, R. Perry, M. Sutherland, A. Rost, S. Grigera, R. Borzi, P. Gegenwart, and A. Mackenzie, "Quantum oscillations in the anomalous phase in $\text{Sr}_3\text{Ru}_2\text{O}_7$," *Physical review letters*, vol. 103, no. 17, p. 176401, 2009.
- [17] C. Lester, S. Ramos, R. Perry, T. Croft, R. Bewley, T. Guidi, P. Manuel, D. Khalyavin, E. Forgan, and S. Hayden, "Field-tunable spin-density-wave phases in $\text{Sr}_3\text{Ru}_2\text{O}_7$," *Nature materials*, 2015.
- [18] D. Xiao, G.-B. Liu, W. Feng, X. Xu, and W. Yao, "Coupled Spin and Valley Physics in Monolayers of MoS_2 and Other Group-VI Dichalcogenides," *Phys. Rev. Lett.*, vol. 108, p. 196802, May 2012. [Online]. Available: <http://link.aps.org/doi/10.1103/PhysRevLett.108.196802>
- [19] K. F. Mak, K. He, J. Shan, and T. F. Heinz, "Control of valley polarization in monolayer MoS_2 by optical helicity," *Nat. Nanotechnol.*, vol. 7, no. 8, p. 494, 2012.

- [20] A. M. Jones, H. Yu, N. J. Ghimire, S. Wu, G. Aivazian, J. S. Ross, B. Zhao, J. Yan, D. G. Mandrus, D. Xiao, W. Yao, and X. Xu, "Optical generation of excitonic valley coherence in monolayer WSe_2 ," *Nat. Nanotechnol.*, vol. 8, no. 9, p. 634, 2013.
- [21] G. Kioseoglou, A. T. Hanbicki, M. Currie, A. L. Friedman, D. Gunlycke, and B. T. Jonker, "Valley polarization and intervalley scattering in monolayer MoS_2 ," *Appl. Phys. Lett.*, vol. 101, no. 22, p. 221907, 2012.
- [22] H. Zeng, J. Dai, W. Yao, D. Xiao, and X. Cui, "Valley polarization in MoS_2 monolayers by optical pumping," *Nat. Nanotechnology*, vol. 7, no. 8, p. 490, 2012.
- [23] T. Cao, G. Wang, W. Han, H. Ye, C. Zhu, J. Shi, Q. Niu, P. Tan, E. Wang, B. Liu, and J. Feng, "Valley-selective circular dichroism of monolayer molybdenum disulphide," *Nat. Commun.*, vol. 3, p. 887, 2012.
- [24] G. Sallen, L. Bouet, X. Marie, G. Wang, C. R. Zhu, W. P. Han, Y. Lu, P. H. Tan, T. Amand, B. L. Liu, and B. Urbaszek, "Robust optical emission polarization in MoS_2 monolayers through selective valley excitation," *Phys. Rev. B*, vol. 86, p. 081301, Aug 2012. [Online]. Available: <http://link.aps.org/doi/10.1103/PhysRevB.86.081301>
- [25] K. F. Mak, K. L. McGill, J. Park, and P. L. McEuen, "The Valley Hall Effect in MoS_2 Transistors," *Science*, vol. 344, pp. 1489–1492, Jun 2014.
- [26] J. S. Ross, S. Wu, H. Yu, N. J. Ghimire, A. M. Jones, G. Aivazian, J. Yan, D. G. Mandrus, D. Xiao, W. Yao, and X. Xu, "Electrical control of neutral and charged excitons in a monolayer semiconductor," *Nat. Commun.*, vol. 4, p. 1474, 2013.
- [27] Y. Zhang, T.-R. Chang, B. Zhou, Y.-T. Cui, H. Yan, Z. Liu, F. Schmitt, J. Lee, R. Moore, Y. Chen, H. Lin, H.-T. Jeng, S.-K. Mo, Z. Hussain, A. Bansil, and Z.-X. Shen, "Direct observation of the transition from indirect to direct bandgap in atomically thin epitaxial $MoSe_2$," *Nat. Nanotechnol.*, vol. 9, p. 111, 2013.
- [28] M. Chhowalla, H. S. Shin, G. Eda, L.-J. Li, K. P. Loh, and H. Zhang, "The chemistry of two-dimensional layered transition metal dichalcogenide nanosheets," *Nature chemistry*, vol. 5, no. 4, pp. 263–275, 2013.
- [29] K. F. Mak, C. Lee, J. Hone, J. Shan, and T. F. Heinz, "Atomically Thin MoS_2 : A New Direct-Gap Semiconductor," *Phys.*

- Rev. Lett.*, vol. 105, p. 136805, Sep 2010. [Online]. Available: <http://link.aps.org/doi/10.1103/PhysRevLett.105.136805>
- [30] D. Xiao, W. Yao, and Q. Niu, "Valley-Contrasting Physics in Graphene: Magnetic Moment and Topological Transport," *Phys. Rev. Lett.*, vol. 99, p. 236809, Dec 2007. [Online]. Available: <http://link.aps.org/doi/10.1103/PhysRevLett.99.236809>
- [31] W. Yao, D. Xiao, and Q. Niu, "Valley-dependent optoelectronics from inversion symmetry breaking," *Phys. Rev. B*, vol. 77, p. 235406, Jun 2008. [Online]. Available: <http://link.aps.org/doi/10.1103/PhysRevB.77.235406>
- [32] A. Kormányos, V. Zólyomi, N. D. Drummond, and G. Burkard, "Spin-Orbit Coupling, Quantum Dots, and Qubits in Monolayer Transition Metal Dichalcogenides," *Phys. Rev. X*, vol. 4, p. 011034, Mar 2014. [Online]. Available: <http://link.aps.org/doi/10.1103/PhysRevX.4.011034>
- [33] X. Li, F. Zhang, and Q. Niu, "Unconventional Quantum Hall Effect and Tunable Spin Hall Effect in Dirac Materials: Application to an Isolated MoS₂ Trilayer," *Phys. Rev. Lett.*, vol. 110, p. 066803, Feb 2013. [Online]. Available: <http://link.aps.org/doi/10.1103/PhysRevLett.110.066803>
- [34] R.-L. Chu, X. Li, S. Wu, Q. Niu, W. Yao, X. Xu, and C. Zhang, "Valley-splitting and valley-dependent inter-Landau-level optical transitions in monolayer MoS₂ quantum Hall systems," *Phys. Rev. B*, vol. 90, p. 045427, Jul 2014. [Online]. Available: <http://link.aps.org/doi/10.1103/PhysRevB.90.045427>
- [35] H. Rostami, A. G. Moghaddam, and R. Asgari, "Effective lattice Hamiltonian for monolayer MoS₂: Tailoring electronic structure with perpendicular electric and magnetic fields," *Phys. Rev. B*, vol. 88, p. 085440, Aug 2013. [Online]. Available: <http://link.aps.org/doi/10.1103/PhysRevB.88.085440>
- [36] Y.-H. Ho, Y.-H. Wang, and H.-Y. Chen, "Magnetoelectronic and optical properties of a MoS₂ monolayer," *Phys. Rev. B*, vol. 89, p. 155316, Apr 2014. [Online]. Available: <http://link.aps.org/doi/10.1103/PhysRevB.89.155316>
- [37] T. Cai, S. A. Yang, X. Li, F. Zhang, J. Shi, W. Yao, and Q. Niu, "Magnetic control of the valley degree of freedom of massive

Dirac fermions with application to transition metal dichalcogenides," *Phys. Rev. B*, vol. 88, p. 115140, Sep 2013. [Online]. Available: <http://link.aps.org/doi/10.1103/PhysRevB.88.115140>

- [38] NewportOptics. (2015, January) Fiber optic coupling. [Online]. Available: <http://www.newport.com/Fiber-Optic-Coupling/144877/1033/content.aspx>
- [39] C. A. Randall, N. Kim, J.-P. Kucera, W. Cao, and T. R. Shrout, "Intrinsic and extrinsic size effects in fine-grained morphotropic-phase-boundary lead zirconate titanate ceramics," *Journal of the American Ceramic Society*, vol. 81, no. 3, pp. 677–688, 1998.
- [40] S. Kimura and T. Wilson, "Confocal scanning optical microscope using single-mode fiber for signal detection," *Applied optics*, vol. 30, no. 16, pp. 2143–2150, 1991.
- [41] E. Hecht, "Optics 2nd edition," *Optics 2nd edition by Eugene Hecht Reading, MA: Addison-Wesley Publishing Company, 1987*, vol. 1, 1987.
- [42] M. Debessai, J. Hamlin, and J. Schilling, "Comparison of the pressure dependences of T_c in the trivalent d-electron superconductors Sc, Y, La, and Lu up to megabar pressures," *Physical Review B*, vol. 78, no. 6, p. 064519, 2008.
- [43] D. Penninckx and N. Beck, "Definition, meaning, and measurement of the polarization extinction ratio of fiber-based devices," *Applied optics*, vol. 44, no. 36, pp. 7773–7779, 2005.
- [44] C. Mirri, L. Baldassarre, S. Lupi, M. Ortolani, R. Fittipaldi, A. Vecchione, and P. Calvani, "Anisotropic optical conductivity of $\text{Sr}_3\text{Ru}_2\text{O}_7$," *Physical Review B*, vol. 78, no. 15, p. 155132, 2008.
- [45] L. Klein, J. Dodge, T. Geballe, A. Kapitulnik, A. Marshall, L. Antognazza, and K. Char, "Perpendicular magnetic anisotropy and strong magneto-optic properties of SrRuO_3 epitaxial films," *Applied physics letters*, vol. 66, no. 18, pp. 2427–2429, 1995.
- [46] W. Zou, Z. He, and K. Hotate, "Complete discrimination of strain and temperature using brillouin frequency shift and birefringence in a polarization-maintaining fiber," *Optics express*, vol. 17, no. 3, pp. 1248–1255, 2009.

- [47] G. Westenberger, H. J. Hoffmann, W. W. Jochs, and G. Przybilla, "Verdet constant and its dispersion in optical glasses," in *San Diego, '91, San Diego, CA*. International Society for Optics and Photonics, 1991, pp. 113–120.
- [48] J. Noda, K. Okamoto, and Y. Sasaki, "Polarization-maintaining fibers and their applications," *Lightwave Technology, Journal of*, vol. 4, no. 8, pp. 1071–1089, 1986.
- [49] N. Caponio and C. Svelto, "A simple angular alignment technique for a polarization-maintaining-fiber," *Photonics Technology Letters, IEEE*, vol. 6, no. 6, pp. 728–729, 1994.
- [50] Y. Ida, K. Hayashi, M. Jinno, T. Horii, and K. Arai, "New method for polarisation alignment of birefringent fibre with laser diode," *Electronics letters*, vol. 21, no. 1, pp. 18–20, 1985.
- [51] M. Tsubokawa, T. Higashi, and Y. Negishi, "Mode couplings due to external forces distributed along a polarization-maintaining fiber: an evaluation," *Applied optics*, vol. 27, no. 1, pp. 166–173, 1988.
- [52] N. F. Borrelli, "Faraday rotation in glasses," *The Journal of Chemical Physics*, vol. 41, no. 11, pp. 3289–3293, 1964.
- [53] A. Rost, R. Perry, J.-F. Mercure, A. Mackenzie, and S. Grigera, "Entropy landscape of phase formation associated with quantum criticality in $\text{Sr}_3\text{Ru}_2\text{O}_7$," *Science*, vol. 325, no. 5946, pp. 1360–1363, 2009.
- [54] A. Daire, W. Goeke, and M. Tupta, "White Paper: New instruments can lock out lock-ins," Technical Report, Keithley Instruments, Inc., Cleveland, OH, Tech. Rep., 2005.
- [55] A. Kapitulnik, "Notes on constraints for the observation of Polar Kerr Effect in complex materials," *Physica B: Condensed Matter*, 2014.
- [56] M. Hayne and B. Bansal, "High-field magneto-photoluminescence of semiconductor nanostructures," *Luminescence*, vol. 27, no. 3, pp. 179–196, 2012.
- [57] A. V. Malyavkin, "Bound multiple exciton complex in CdTe," *Solid State Commun.*, vol. 39, no. 12, pp. 1315–1317, 1981.
- [58] E. Molva and L. S. Dang, "Magneto-optical studies of excitons bound to

- Ag and Cu acceptors in p-type CdTe," *Phys. Rev. B*, vol. 27, no. 10, p. 6222, 1983.
- [59] —, "Magneto-optical study of Li and Na acceptor bound excitons in CdTe: Fine structure and cubic crystal-field effect," *Phys. Rev. B*, vol. 32, no. 2, p. 1156, 1985.
- [60] T. Kazimierczuk, T. Smoleński, M. Goryca, P. Wojnar, K. Fronc, A. Golnik, M. Nawrocki, J. Gaj, P. Kossacki *et al.*, "Magnetophotoluminescence study of intershell exchange interaction in CdTe/ZnTe quantum dots," *Physical Review B*, vol. 84, no. 16, p. 165319, 2011.
- [61] G.-B. Liu, W.-Y. Shan, Y. Yao, W. Yao, and D. Xiao, "Three-band tight-binding model for monolayers of group-VIB transition metal dichalcogenides," *Phys. Rev. B*, vol. 88, p. 085433, Aug 2013. [Online]. Available: <http://link.aps.org/doi/10.1103/PhysRevB.88.085433>
- [62] K. Kośmider, J. W. González, and J. Fernández-Rossier, "Large spin splitting in the conduction band of transition metal dichalcogenide monolayers," *Phys. Rev. B*, vol. 88, p. 245436, Dec 2013. [Online]. Available: <http://link.aps.org/doi/10.1103/PhysRevB.88.245436>
- [63] M.-C. Chang and Q. Niu, "Berry curvature, orbital moment, and effective quantum theory of electrons in electromagnetic fields," *J. Phys.: Condens. Matter*, vol. 20, no. 19, p. 193202, 2008. [Online]. Available: <http://stacks.iop.org/0953-8984/20/i=19/a=193202>
- [64] A. Kormányos, V. Zólyomi, N. D. Drummond, P. Rakyta, G. Burkard, and V. I. Fal'ko, "Monolayer MoS₂: Trigonal warping, the Γ valley, and spin-orbit coupling effects," *Phys. Rev. B*, vol. 88, p. 045416, Jul 2013. [Online]. Available: <http://link.aps.org/doi/10.1103/PhysRevB.88.045416>
- [65] A. Srivastava, M. Sidler, A. V. Allain, D. S. Lembke, A. Kis, and A. Imamoglu, "Valley Zeeman Effect in Elementary Optical Excitations of a Monolayer WSe₂," *arXiv:1407.2624*, 2014.
- [66] G. Aivazian, Z. Gong, A. M. Jones, R.-L. Chu, J. Yan, D. G. Mandrus, C. Zhang, D. Cobden, W. Yao, and X. Xu, "Magnetic Control of Valley Pseudospin in Monolayer WSe₂," *arXiv:1407.2645*, 2014.
- [67] Z. Y. Zhu, Y. C. Cheng, and U. Schwingenschlögl, "Giant spin-orbit-induced spin splitting in two-dimensional transition-metal dichalcogenide semiconductors," *Phys. Rev. B*, vol. 84, no. 15, p. 153402, 2011.

- [68] Y. Yafet, "g Factors and Spin-Lattice Relaxation of Conduction Electrons," *Solid State Phys*, vol. 14, p. 1, 1963.
- [69] A. A. Mitioglu, P. Plochocka, J. N. Jadczak, W. Escoffier, G. L. J. A. Rikken, L. Kulyuk, and D. K. Maude, "Optical manipulation of the exciton charge state in single-layer tungsten disulfide," *Phys. Rev. B*, vol. 88, p. 245403, Dec 2013. [Online]. Available: <http://link.aps.org/doi/10.1103/PhysRevB.88.245403>
- [70] C. Zhang, H. Wang, W. Chan, C. Manolatou, and F. Rana, "Absorption of light by excitons and trions in monolayers of metal dichalcogenide MoS₂: Experiments and theory," *Phys. Rev. B*, vol. 89, p. 205436, May 2014. [Online]. Available: <http://link.aps.org/doi/10.1103/PhysRevB.89.205436>
- [71] G. L. Bir, A. G. Aronov, and G. E. Pikus, "Spin relaxation of electrons due to scattering by holes," *Zh. Eksp. Teor. Fiz.*, vol. 69, no. 4, p. 1382, 1975.
- [72] J. Ma and Y.-S. Li, "Fiber Raman background study and its application in setting up optical fiber Raman probes," *Appl. Opt.*, vol. 35, no. 15, pp. 2527–2533, 1996.
- [73] H. Yu, G.-B. Liu, P. Gong, X. Xu, and W. Yao, "Dirac cones and Dirac saddle points of bright excitons in monolayer transition metal dichalcogenides," *Nat. Commun.*, vol. 5, p. 3876, 2014.
- [74] C. R. L. P. N. Jeukens, P. C. M. Christianen, J. C. Maan, D. R. Yakovlev, W. Ossau, V. P. Kochereshko, T. Wojtowicz, G. Karczewski, and J. Kossut, "Dynamical equilibrium between excitons and trions in CdTe quantum wells in high magnetic fields," *Phys. Rev. B*, vol. 66, p. 235318, Dec 2002. [Online]. Available: <http://link.aps.org/doi/10.1103/PhysRevB.66.235318>
- [75] G. Wang, L. Bouet, D. Lagarde, M. Vidal, A. Balocchi, T. Amand, X. Marie, and B. Urbaszek, "Valley dynamics probed through charged and neutral exciton emission in monolayer WSe₂," *Phys. Rev. B*, vol. 90, p. 075413, Aug 2014. [Online]. Available: <http://link.aps.org/doi/10.1103/PhysRevB.90.075413>
- [76] J. M. Luttinger, "Quantum Theory of Cyclotron Resonance in Semiconductors: General Theory," *Phys. Rev.*, vol. 102, pp. 1030–1041, May 1956. [Online]. Available: <http://link.aps.org/doi/10.1103/PhysRev.102.1030>

- [77] L. M. Roth, "g Factor and Donor Spin-Lattice Relaxation for Electrons in Germanium and Silicon," *Phys. Rev.*, vol. 118, pp. 1534–1540, Jun 1960. [Online]. Available: <http://link.aps.org/doi/10.1103/PhysRev.118.1534>
- [78] S. Wu, J. S. Ross, G.-B. Liu, G. Aivazian, A. Jones, Z. Fei, W. Zhu, D. Xiao, W. Yao, D. Cobden, and X. Xu, "Electrical tuning of valley magnetic moment through symmetry control in bilayer MoS₂," *Nat. Phys.*, vol. 9, no. 3, pp. 149–153, 2013.
- [79] A. Kormányos, V. Zólyomi, M. Gmitra, N. D. Drummond, J. Fabian, V. Fal'ko, and G. Burkard, "Model Hamiltonians and material parameters for monolayer transition metal dichalcogenides," *arXiv:1410.6666*, 2014.
- [80] A. Ramasubramaniam, "Large excitonic effects in monolayers of molybdenum and tungsten dichalcogenides," *Phys. Rev. B*, vol. 86, p. 115409, Sep 2012. [Online]. Available: <http://link.aps.org/doi/10.1103/PhysRevB.86.115409>
- [81] R. S. Knox, *Theory of Excitons*. Academic Press, New York, 1963.
- [82] N. A. Gippius, A. L. Yablonskii, A. B. Dzyubenko, S. G. Tikhodeev, L. V. Kulik, V. D. Kulakovskii, and A. Forchel, "Excitons in near-surface quantum wells in magnetic fields: Experiment and theory," *J. Appl. Phys.*, vol. 83, no. 10, p. 5410, 1998.
- [83] G. Berghäuser and E. Malic, "Analytical approach to excitonic properties of MoS₂," *Phys. Rev. B*, vol. 89, p. 125309, Mar 2014. [Online]. Available: <http://link.aps.org/doi/10.1103/PhysRevB.89.125309>
- [84] T. C. Berkelbach, M. S. Hybertsen, and D. R. Reichman, "Theory of neutral and charged excitons in monolayer transition metal dichalcogenides," *Phys. Rev. B*, vol. 88, p. 045318, Jul 2013. [Online]. Available: <http://link.aps.org/doi/10.1103/PhysRevB.88.045318>
- [85] M. Sugawara, N. Okazaki, T. Fujii, and S. Yamazaki, "Diamagnetic shift and oscillator strength of two-dimensional excitons under a magnetic field in In_{0.53}Ga_{0.47}As/InP quantum wells," *Phys. Rev. B*, vol. 48, pp. 8848–8856, Sep 1993. [Online]. Available: <http://link.aps.org/doi/10.1103/PhysRevB.48.8848>
- [86] H. Q. Hou, W. Staguhn, S. Takeyama, N. Miura, Y. Segawa, Y. Aoyagi, and S. Namba, "Diamagnetic shift in In_xGa_{1-x}As/GaAs strained quantum

- wells," *Phys. Rev. B*, vol. 43, pp. 4152–4157, Feb 1991. [Online]. Available: <http://link.aps.org/doi/10.1103/PhysRevB.43.4152>
- [87] D. C. Rogers, J. Singleton, R. J. Nicholas, C. T. Foxon, and K. Woodbridge, "Magneto-optics in GaAs-Ga_{1-x}Al_xAs quantum wells," *Phys. Rev. B*, vol. 34, pp. 4002–4009, Sep 1986. [Online]. Available: <http://link.aps.org/doi/10.1103/PhysRevB.34.4002>
- [88] B. Hunt, J. Sanchez-Yamagishi, A. Young, M. Yankowitz, B. J. LeRoy, K. Watanabe, T. Taniguchi, P. Moon, M. Koshino, P. Jarillo-Herrero *et al.*, "Massive Dirac fermions and Hofstadter butterfly in a van der Waals heterostructure," *Science*, vol. 340, no. 6139, pp. 1427–1430, 2013.
- [89] C. Dean, A. Young, I. Meric, C. Lee, L. Wang, S. Sorgenfrei, K. Watanabe, T. Taniguchi, P. Kim, K. Shepard *et al.*, "Boron nitride substrates for high-quality graphene electronics," *Nature nanotechnology*, vol. 5, no. 10, pp. 722–726, 2010.
- [90] S. Tiwari, "Nanoscale device physics, Chapter 4, Phase transitions and their devices," provided as class notes.
- [91] W. Zhang, M. Takahashi, and S. Sakai, "Electrical properties of Ca_xSr_{1-x}Bi₂Ta₂O₉ ferroelectric-gate field-effect transistors," *Semiconductor Science and Technology*, vol. 28, no. 8, p. 085003, 2013.
- [92] M. P. Warusawithana, C. Cen, C. R. Sleasman, J. C. Woicik, Y. Li, L. F. Kourkoutis, J. A. Klug, H. Li, P. Ryan, L.-P. Wang *et al.*, "A ferroelectric oxide made directly on silicon," *Science*, vol. 324, no. 5925, pp. 367–370, 2009.
- [93] S. Sakai and R. Ilangovan, "Metal-ferroelectric-insulator-semiconductor memory FET with long retention and high endurance," *Electron Device Letters, IEEE*, vol. 25, no. 6, pp. 369–371, 2004.
- [94] X. Hong, A. Posadas, K. Zou, C. H. Ahn, and J. Zhu, "High-mobility few-layer graphene field effect transistors fabricated on epitaxial ferroelectric gate oxides," *Phys. Rev. Lett.*, vol. 102, p. 136808, Apr 2009. [Online]. Available: <http://link.aps.org/doi/10.1103/PhysRevLett.102.136808>
- [95] Y. Zheng, G.-X. Ni, C.-T. Toh, C.-Y. Tan, K. Yao, and B. Özyilmaz, "Graphene field-effect transistors with ferroelectric gating," *Physical review letters*, vol. 105, no. 16, p. 166602, 2010.

- [96] Y.-W. Tan, Y. Zhang, K. Bolotin, Y. Zhao, S. Adam, E. Hwang, S. D. Sarma, H. Stormer, and P. Kim, "Measurement of scattering rate and minimum conductivity in graphene," *Physical Review Letters*, vol. 99, no. 24, p. 246803, 2007.
- [97] E. Hwang, S. Adam, and S. D. Sarma, "Carrier transport in two-dimensional graphene layers," *Physical Review Letters*, vol. 98, no. 18, p. 186806, 2007.
- [98] X. Hong, J. Hoffman, A. Posadas, K. Zou, C. Ahn, and J. Zhu, "Unusual resistance hysteresis in n-layer graphene field effect transistors fabricated on ferroelectric $\text{Pb}(\text{Zr}_{0.2}\text{Ti}_{0.8})\text{O}_3$," *Applied Physics Letters*, vol. 97, no. 3, p. 033114, 2010.
- [99] E. B. Song, B. Lian, S. M. Kim, S. Lee, T.-K. Chung, M. Wang, C. Zeng, G. Xu, K. Wong, Y. Zhou *et al.*, "Robust bi-stable memory operation in single-layer graphene ferroelectric memory," *Applied Physics Letters*, vol. 99, no. 4, p. 042109, 2011.
- [100] S. Saha, O. Kahya, M. Jaiswal, A. Srivastava, A. Annadi, J. Balakrishnan, A. Pachoud, C.-T. Toh, B.-H. Hong, J.-H. Ahn *et al.*, "Unconventional Transport through Graphene on SrTiO_3 : A Plausible Effect of SrTiO_3 Phase-Transitions," *Scientific reports*, vol. 4, 2014.
- [101] M. H. Yusuf, B. Nielsen, M. Dawber, and X. Du, "Extrinsic and intrinsic charge trapping at the graphene/ferroelectric interface," *Nano letters*, vol. 14, no. 9, pp. 5437–5444, 2014.
- [102] S. Jo, N. Ubrig, H. Berger, A. B. Kuzmenko, and A. F. Morpurgo, "Mono- and Bilayer WS_2 Light-Emitting Transistors," *Nano letters*, vol. 14, no. 4, pp. 2019–2025, 2014.
- [103] Y. Zhang, T. Oka, R. Suzuki, J. Ye, and Y. Iwasa, "Electrically switchable chiral light-emitting transistor," *Science*, vol. 344, no. 6185, pp. 725–728, 2014.
- [104] L. Chu, H. Schmidt, J. Pu, S. Wang, B. Özyilmaz, T. Takenobu, and G. Eda, "Charge transport in ion-gated mono-, bi-, and trilayer MoS_2 field effect transistors," *Scientific reports*, vol. 4, 2014.
- [105] K. Bethe and F. Welz, "Preparation and properties of (Ba, Sr) TiO_3 single crystals," *Materials Research Bulletin*, vol. 6, no. 4, pp. 209–217, 1971.

- [106] D. Nuzhnyy, J. Petzelt, S. Kamba, X. Martí, T. Čechal, C. Brooks, and D. Schlom, "Infrared phonon spectroscopy of a compressively strained (001) SrTiO₃ film grown on a (110) NdGaO₃ substrate," *Journal of Physics: Condensed Matter*, vol. 23, no. 4, p. 045901, 2011.
- [107] T. Yamada, J. Petzelt, A. Tagantsev, S. Denisov, D. Noujni, P. Petrov, A. Mackova, K. Fujito, T. Kiguchi, K. Shinozaki *et al.*, "In-Plane and Out-of-Plane Ferroelectric Instabilities in Epitaxial SrTiO₃ Films," *Physical review letters*, vol. 96, no. 15, p. 157602, 2006.
- [108] D. G. Schlom, L.-Q. Chen, C.-B. Eom, K. M. Rabe, S. K. Streiffer, and J.-M. Triscone, "Strain tuning of ferroelectric thin films*," *Annu. Rev. Mater. Res.*, vol. 37, pp. 589–626, 2007.
- [109] H. Jang, A. Kumar, S. Denev, M. Biegalski, P. Maksymovych, C. Bark, C. Nelson, C. Folkman, S. Baek, N. Balke *et al.*, "Ferroelectricity in strain-free SrTiO₃ thin films," *Physical review letters*, vol. 104, no. 19, p. 197601, 2010.